ulm university universität
uulm

Design and Mechanical Performance of Fully Dense Nanocrystalline Noble Metals on the Basis of Pd, Pd-Ag and Pd-Au

DISSERTATION

zur Erlangung des akademischen Grades eines

DOKTOR-INGENIEURS

(DR.-ING.)

der Fakultät für Ingenieurwissenschaften
und Informatik der Universität Ulm

von

Lilia Kurmanaeva

aus Salavat, Russia

Gutachter:	Prof. Dr. Hans-Jörg Fecht Prof. Dr. Ruslan Valiev
Amtierender Dekan:	Prof. Dr.-Ing. Klaus Dietmayer

Ulm, 07.07.2011

Table of Contents

1 INTRODUCTION AND OBJECTIVES 1

1.1 Introduction 1

1.2 Objectives of present study 3

2 THE STATE OF THE ART 5

2.1 Synthesis of bulk nanocrystalline materials 5
2.1.1 Physical methods: Inert Gas Condensation (IGC) 6
2.1.2 Chemical methods: Electrodeposition (ED) 7
2.1.3 Solid state processing by severe plastic deformation (SPD) 8

2.2 Plastic deformation mechanisms in ultrafine grained and nanocrystalline fcc metals: results from experiments and molecular dynamic simulations 12
2.2.1 Slip of full dislocations 12
2.2.2 Slip of partial dislocations and twinning 13
2.2.3 Grain boundary mediated mechanisms 14

2.3 Balance of high strength and good ductility in nanocrystalline materials 17
2.3.1 Strengthening mechanisms 17
2.3.1.1 The grain size strengthening 18
2.3.1.2 Strengthening by storage of dislocations inside of grains 19
2.3.2 Ductility 20

3 MATERIALS SYNTHESIS AND ANALYTICAL METHODS 25

3.1 Materials for investigation 25

3.2 Processing methods 28
3.2.1 Nanocrystalline specimens 28
3.2.2 Ultrafine grained specimens 28

3.3 Microstructure characterization 30
3.3.1 X-ray diffraction (XRD) 30
3.3.2 Transmission electron microscopy (TEM) 33

3.4 Mechanical property tests 35
3.4.1 Hardness measurements 35
3.4.2 Tensile and compression measurements 35
3.4.2.1 Background on mechanical tests 35
3.4.2.2 Experimental procedures 37
3.4.4 Compression-torsion tests 39

4 EXPERIMENTAL RESULTS 41

4.1 Micro- and nanostructure formation resulting from severe shear deformation and related deformation mechanisms in nc and ufg Pd and Pd-Ag alloys 41
4.1.1 Microstructure of Pd-Ag alloys resulting from High Pressure Torsion 41
4.1.2 Microstructural evolution by TEM analysis 47
4.1.2.1 XRD analysis of nc Pd resulting from compression-torsion tests 47
4.1.2.2 Microstructure evolution (TEM) 49

4.2 Mechanical performance of nc and ufg Pd and Pd alloys 54
4.2.1 Results of tensile tests of Pd-Ag alloys 54
4.2.2 Mechanical properties of nanocrystalline Pd and Pd-10 at.% Au 55
4.2.3 Mechanical properties of Pd with bimodal microstructure 59

5 DISCUSSION 61

5.1 Fundamental plastic deformation mechanisms in nc and ufg Pd and Pd alloys ... 61
5.1.1 Deformation mechanisms in ultra-fine grained Pd-Ag alloys 62
5.1.2 Deformation mechanisms in nc Pd 63
5.1.3 Deformation map for Pd 66

5.2 Mechanical behaviour of nc and ufg Pd and Pd alloys 67
5.2.1 Strengthening mechanisms 67
5.2.1.1 Ultra-fine grained Pd-Ag alloys 67
5.2.1.2 Nanocrystalline Pd and Pd-10at.% Au 68
5.2.2 Analysis and tailoring of ductility in nanocrystalline metals 70
5.2.2.1 Improving ductility by alloying in Pd-Ag alloys 70
5.2.2.2 Improved ductility in Pd with bimodal microstructure 72
5.2.2.3 Inherent plastic instability of nanocrystalline Pd and Pd-10at.% Au 72

6 SUMMARY AND OUTLOOK 75

APPENDIX 79

A. Kinetic analysis of nanocrystalline materials 79

B. List of abbreviations and symbols 81

REFERENCES 83

CURRICULUM VITAE 92

PUBLICATIONS 93

CONFERENCE CONTRIBUTIONS 94

ACKNOWLEDGEMENTS 95

Chapter 1

Introduction and objectives

1.1 Introduction

Nanotechnology as a key technology has gained a wide interest in science and engineering due to the possibility of designing and producing entirely new materials with unique properties. In this regard, advanced nanocrystalline materials exhibiting a pronounced nanostructure are a key issue in improving the performance and functionality of advanced compounds and devices. This is not only important for fundamental studies in solid state physics and chemistry but also for engineering applications, for example in the field of microelectronics, electronic packaging and micro-electro-mechanical (MEMS) devices and systems.

As such, the recent past has seen an increasing interest in studies of the relationship between microstructure and mechanical properties of nanocrystalline (nc) materials. It is well established in material science that grain boundaries are effective obstacles for dislocation motion in metals, as generally described by the increase of the yield stress of polycrystals with decreasing grain size, expressed in general in Hall-Petch type equations [1,2]. For example, it has been established in the 1950's that the yield strength of mild steels can be increased by a factor 3 when the grain size is reduced to the range of micrometers. Thus, it can be expected that reducing the grain size of the metal to very small values in the range of a few nanometers dislocation activity will become less important in favor of alternative mechanisms which involve new mechanisms at grain boundaries [3,4]. Moreover, since nc materials are characterized by a large volume fraction of grain boundaries and atoms located therein with structural components differing significantly from the crystalline core part, other physical and chemical properties and functionalities will be altered as well.

Nanocrystalline materials are defined as polycrystalline materials that have at least one dimension in "nanoscale" (typically from 100 down to 1 nm). Depending on the dimensions in which the length is "nanoscale", they can be differently classified into nanoparticles and clusters, thin films and layered structures, as well as bulk nanostructured materials [5]. Classification can also be made based on the grain size [6]: ultrafine-grain (ufg) materials, where grain sizes are less than ~ 1 μm, nanocrystalline materials where the average grain size is typically less than 10-20 nm. However, in practice, materials also

exhibit other structural elements having sizes of less than 100 nm including second phase particles or precipitates, dislocation substructures, pores, etc. These nanometer-sized features also have a considerable influence on the properties of the materials. Materials containing these nanostructural elements are designated nanostructured (ns) materials. Besides, for materials which are qualified as bulk nanostructured materials the sample size is large extending over several mm and thus containing typically 10^{15} - 10^{16} grains [7].

In the mid-1980s, Gleiter [8] made the visionary argument that metals and alloys, if produced in a nanocrystalline state, would have a number of appealing mechanical characteristics of potential significance for structural applications. Compared with conventional coarse-grained (cg) materials, the benefits that may be derived from nanostructuring include ultrahigh yield and fracture strengths, superior wear resistance, and possibly superplastic formability at low temperatures and/or high strain rates.

NC materials can be prepared through either a "bottom-up" approach, when the nanocrystalline structure is built atom by atom, or a "top-down" approach, when the nanostructure is synthesized by breaking down the bulk microstructure into the nanoscale. There are several commonly used chemical and physical methods, such as for examples inert gas condensation, which is a "bottom-up" approach, and severe plastic deformation (SPD) – as a "top-down approach". In the recent years, considerably progress has developed in SPD techniques worldwide [9,10]. As such, it has become realistic to produce ufg materials in commercially reasonable amounts. Thanks to their outstanding mechanical properties, ufg materials obtained by means of SPD offer a wide range of applications as structural building units and components. The potential for technical innovations based on SPD materials has been demonstrated for many areas [11,12,13], e.g. in the production of Ti-based medical implants, superplastic forming of light metals, nanosteels and Cu-alloys with combined mechanical strength and electrical conductivity, and others.

1.2 Objectives of present study

The understanding of deformation mechanisms operating in nanocrystalline materials is very important in order to understand and improve their mechanical properties, and it is necessary for the scientifically motivated design of new materials. Several review papers [14,15] on mechanical properties and deformation mechanisms were published in the last 10 years mostly focussing on metals with grain size more than 100 nm. The present thesis investigates the fundamentals of plastic deformation of fully dense bulk nanocrystalline f.c.c metals, such as Pd and Pd alloys with a grain size as small as 15 nm. It has already been demonstrated [16] that using a method of inert gas condensation (IGC) one can successfully obtain bulk nanocrystalline Pd samples. The present work demonstrates that the application of subsequent high pressure torsion allows to make IGC samples fully dense. Furthermore, alloying was used for the stabilization of the nanostructure and designing new properties of materials. The alloying elements have been chosen to (i) improve the stability of the nc microstructure against room temperature and deformation induced grain growth considerably, and (ii) change the stacking fault energy (Au) of palladium in a controlled manner.

Earlier, J. Markmann et al. [17] already studied the deformation of nc Pd using cold rolling techniques and creep experiments of thin foils which are different by strain rate and geometry. In the present work the same material was investigated in bulk geometry allowing standard tensile and compression tests to be applied. Furthermore, nanocrystalline samples were investigated using unusual methods of torsion testing under high pressure. This method allows deformation of samples to a high strain without causing fracture. The combination of standard and new methods allowed to obtain new information about the deformation mechanisms acting in nanocrystalline metals.

In contrast to the brittleness of nc materials, ufg materials show high strength and good ductility. It is known that ufg materials exhibit superior hardness, strength and fatigue properties as compared to their coarse grained counterparts. However, often they possess a lack of ductility or are affected by rapid strain localization. Usually, stress-strain curves of these materials show failure immediately after onset of yielding [18]. Such behavior is related to the low strain hardening capacity of ufg materials due to limited dislocation storage in small grains. It is expected that any improvement of strain hardening will be beneficial for the ductility, i.e., by enhancing the uniform elongation, in ufg materials [14]. Several routes to improve the ductility of ufg materials were suggested, such as generating

bimodal grain size distributions, nano-twins, dispersion of nano-particles, etc. [19]. The present work confirmed that materials with bimodal grain size distribution showed improved ductility. Furthermore, a quite current method is to increase the ductility by alloying with specific materials with the purpose of decreasing the stacking fault energy (SFE) as shown in Refs. [20,21]. One of the key objectives of the present thesis is therefore to investigate the deformation behaviour and the microstructure in ufg Pd-Ag alloys processed by high pressure torsion. Addition of Ag dramatically decreases γ_{SF} in Pd-Ag alloys leading to improvement of both strength and ductility.

The thesis is organized as follows. Chapter 1 represents an introduction to the topic and objectives of the study, while chapter 2 describes the state of the art of nanocrystalline materials. For instance, section 2.1 briefly highlights several of the most important and commonly used methods for the synthesis of bulk nc materials. Section 2.2 reviews deformation mechanisms of nanostructured materials that have been predicted by molecular-dynamic (MD) simulation and experimentally observed to operate in face-centred cubic (f.c.c) metals. Section 2.3 summarizes experimental observations on strength and ductility of nc materials. Chapter 3 gives a general description on materials and the primary experimental techniques used for the preparation and the characterization of the samples applied in this study. Chapter 4 presents results on the microstructure formation resulted from SPD and mechanical properties of the materials investigated. Chapter 5 discusses the results on deformation mechanisms, strengthening mechanisms that operate in nanostructured Pd and Pd alloys, and principles for obtaining a good combination of strength and ductility. A summary and outlook follows in Chapter 6.

Chapter 2

The state of the art

2.1 Synthesis of bulk nanocrystalline materials

Two complementary approaches have been developed to synthesize nanostructured materials.

The first one is a "**bottom-up approach**", in which bulk nanostructured materials are assembled from individual atoms or nanoscale building blocks such as nanoparticles. Gleiter's pioneering work [22] represents a typical example of "bottom-up" approach. In his method a specially produced nanopowder was used as a basis for bulk nanocrystalline materials. Further various chemical and physical methods have been developed to synthesize nanopowder for small-scale laboratory investigations as well as for large-scale commercial use. These methods include inert gas condensation (IGC) [16,22], ball milling/alloying [23,24], electrodeposition [25], physical vapor deposition [26], chemical vapor deposition [27], etc. The "bottom-up" approach has a number of applications such as films, coatings, electronic devices, drug delivery systems, cosmetics, paints, lubricants, rocket fuel, catalysts, and reinforcement for nanocomposites.

The majority of "bottom-up" methods produce nanopowder or thin layers. For structural applications, the nanopowder needs to be consolidated into a bulk nanocrystalline material. However, a consolidation of nanopowder has been a challenge. Gleiter [16,22] and Nieman et al. [28] suggested a cold compaction of IGC nanopowders *in-situ* in ultrahigh vacuum to obtain nanostructured discs with a diameter of about 10 mm. However, this method still suffers from both the limited final size of samples and a common problem of all two-step methods in that a compaction step may not provide completely dense material. Series of other conventional and new techniques (such as hot pressing, rapid hot forging, spark sinter plasma synthesis etc.) have been used to consolidate nanopowder. The majority of these techniques involves application of heat and pressure. In general, grain growth usually occurs during consolidation, although nanopowders' oxidation and contaminations may help to impede the grain growth.

Electrodeposition (ED) can be classified as the "bottom-up" method of preparation of nanocrystalline materials and also as the "one-step" method since no consolidation step is needed. Thick electrodeposits may be considered as a bulk material. Electrodeposits with

special properties were already prepared in the middle of the 19th century, and at the turn of the 20th century electrolysis was employed to produce special coatings with an enhanced hardness. By using special processing methods a large number of metals, alloys composites and ceramics have been electrodeposited with nanocrystalline structure. ED occurs by nucleation of crystallites on the substrate surface and their subsequent growth along with nucleation of new crystals. However, due to the complex chemical composition of the electrolytes in use remaining chemicals and impurities are generally retained in the metallic coatings.

The second approach for producing nanostructured materials is the "**top-down approach"**, when the initial coarse-grained polycrystalline structure is refined down to nanoscales. Severe plastic deformation (SPD) is the most successful "top-down" method. A possibility of producing very fine grain structure by SPD was proposed by using plastic deformation up to very high strains. Among the most developed SPD techniques are equal-channel angular pressing and high-pressure torsion. Recently, new SPD techniques have been developed, such as accumulated roll bonding, twist extrusion, repetitive corrugation and straightening. SPD-produced materials typically have an average grain size of barely above 100 nm, the upper bound often used to define the nanocrystalline materials. However, subgrains with low misorientation angles, dislocation cell structure, and the coherent crystalline domains as measured by X-ray analysis are usually smaller than 100 nm. Therefore, these materials produced by SPD can be classified as nanostructured materials.

One of the goals of the present work is the investigation of mechanical properties of nanocrystalline materials. The number of preparation methods of nc materials with dimensions suitable for mechanical testing is limited, the most successful techniques are IGC, ED and SPD. Further in sections 2.1.1-2.1.3 a short description of these specific methods including operating principle, advantages and disadvantages is presented and summarized in the Table 2.1.

2.1.1 Physical methods: Inert Gas Condensation (IGC)

In this technique a metal evaporates inside a chamber containing partial pressure (typically few hundred Pascal) of an inert gas, e.g. He, Ar. The evaporated atoms collide with gas atoms, lose their energy, and condense in the form of small discrete crystals of

loose powder. The condensed fine powder is collected on a liquid-nitrogen-cooled finger and is stripped off by a Teflon ring into a compacting device (Fig.2.1).

The IGC method allows producing bulk nanocrystalline samples having uniform equiaxed microstructure with the mean grain size of 5-15 nm, that are texture-free and of very high purity. But the method has several disadvantages including limited specimen volume, relatively high costs of the preparation equipment and residual porosity. There are also difficulties associated with retaining the fine grain size after consolidation [29]. However, this is not the limitation of the method, but an inherent feature of the nc state, that is by definition not a stable structure.

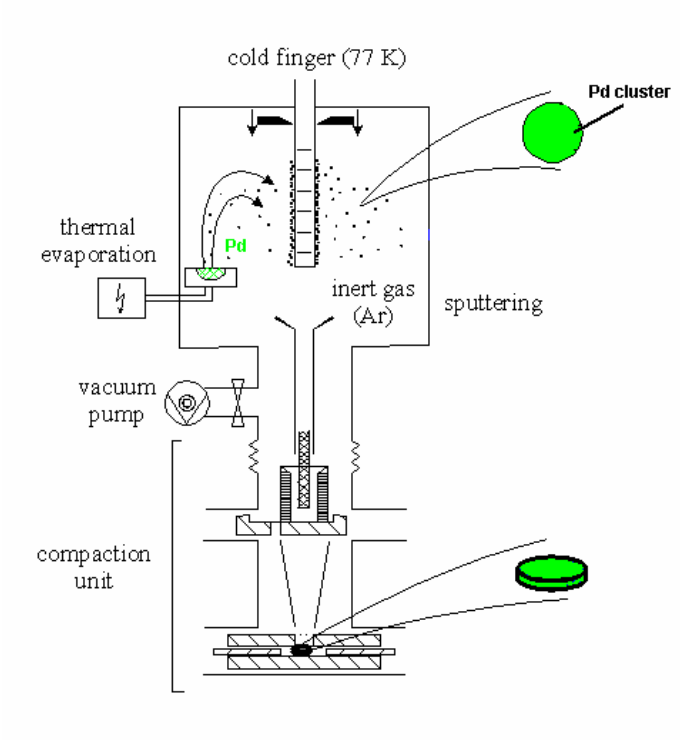


Figure 2.1 A schematic illustration of an IGC process.

2.1.2 Chemical methods: Electrodeposition (ED)

As many other "bottom-up" approaches ED occurs by nucleation of crystallites on the substrate surface and their subsequent growth along with the nucleation of new crystals. Since the late 1980s ED has been widely studied as a method to produce nc materials. Much of the work was pioneered by Erb and coworkers [25,30]. They suggested that in order to obtain nanocrystalline grain size, nucleation events should be favored over growth ones. Variables in ED include bath composition, bath pH, temperature, overpotential, bath

additives, and direct current vs. pulse electrodeposition. The two most important mechanisms that are rate-determining steps for formation of nanoscale grains in ED are a charge transfer at the electrode surface and a surface diffusion of adions on the crystal surface. One method to inhibit the growth of nucleated crystallites is reducing the surface diffusion of adions by adsorption (which may be referred to as "grain refiners" or "additives") on the growing surface. Most of additives are organic materials and may become trapped at grain boundaries and are presumably responsible for the brittle mechanical behavior in nanocrystalline materials processed by ED with additives. Since high overpotential favors extensive nucleation, the second method is pulse platting, where the grain size reduction can be achieved with a short duration of the pulse combined with high peak current densities. In the co-deposition of the alloys, the solute atoms can act as organic additives but without any deleterious embrittlement effect.

2.1.3 Solid state processing by severe plastic deformation (SPD)

For successfully applying the methods of SPD, a number of requirements [9] are to be fulfilled:

1. Methods should provide structures with prevailing high angle GBs. This will lead to qualitative changes in the material's properties.
2. Microstructure should be uniform within the whole volume of the sample. This will provide stable properties of the materials
3. Methods should not exhibit any mechanical damages or cracks.

SPD refers to various experimental procedures of metal forming that may be used to impose very high strains on materials leading to exceptional grain refinement. The unique feature of SPD processing is that the high strain is imposed at relatively low temperatures (usually less then 0.2 of the melting temperature, T_m) without any significant change in the overall dimensions of the workpiece. Another feature is that the shape of sample is retained due to the use of special tool geometries that prevent a free flow of materials and thereby produce a significant hydrostatic pressure. SPD-produced nanomaterials are fully dense and their large geometric dimensions make them attractive for efficient practical applications.

The two most developed SPD techniques are: equal channel angular pressing (ECAP) and high pressure torsion (HPT). Although general principles of processing methods were

proposed more than 60 years ago, the main development of SPD techniques as methods for efficient microstructure refinement occurred during the last 10-15 years.

Equal channel angular pressing (ECAP). The method of ECAP realizing deformation of massive billets via pure shear was developed by Segal and co-workers in the beginning of 1980's [31]. Theirs goal was to introduce an intense plastic strain into materials without changing the cross section area of billets. Due to that, the repeat deformation is possible. However, main reports and overviews of using ECAP as successful method to produce ufg metals with unique properties appeared in 1990s [32]. As illustrated in Fig. 2.2a, during ECAP a rod-shaped billet is pressed through a die constrained within a channel that is bent at an abrupt angle. A shear strain is introduced when the billet passes through the point of intersection of two parts of the channel. Since the cross-section dimensions of the billet remain unchanged, the pressing may be repeated to attain an exceptional high strain. During the repeated pressing, the shear strain is accumulated in the billet, leading ultimately to the formation of an ultra-fine grained structure [33].

High pressure torsion (HPT). The scientific origin of HPT processing was described by Bridgman in 1943 [34]. However, Bridgman studied the mechanical behavior of metals under high hydrostatic pressure. Furthermore, the applied pressure was significantly lower than the ones used in recent HPT. And only by the end of the 1980's it was reported about application of HPT for obtaining homogeneous nanostructures with high-angle grain boundaries [35,36]. HPT refers to a processing in which the sample, generally with the shape of a thin disk, is subjected to torsional straining under a high hydrostatic pressure: the principle of HPT is illustrated schematically in Fig. 2.2b. The disk is located within a cavity, a high pressure is applied, and torsional straining is achieved by the rotation of one of the anvils. Thanks to the special geometric shape, the sample is strained in conditions of quasi-hydrostatic compression under the applied pressure. As a result, in spite of large strain values, the deformed sample is not destroyed.

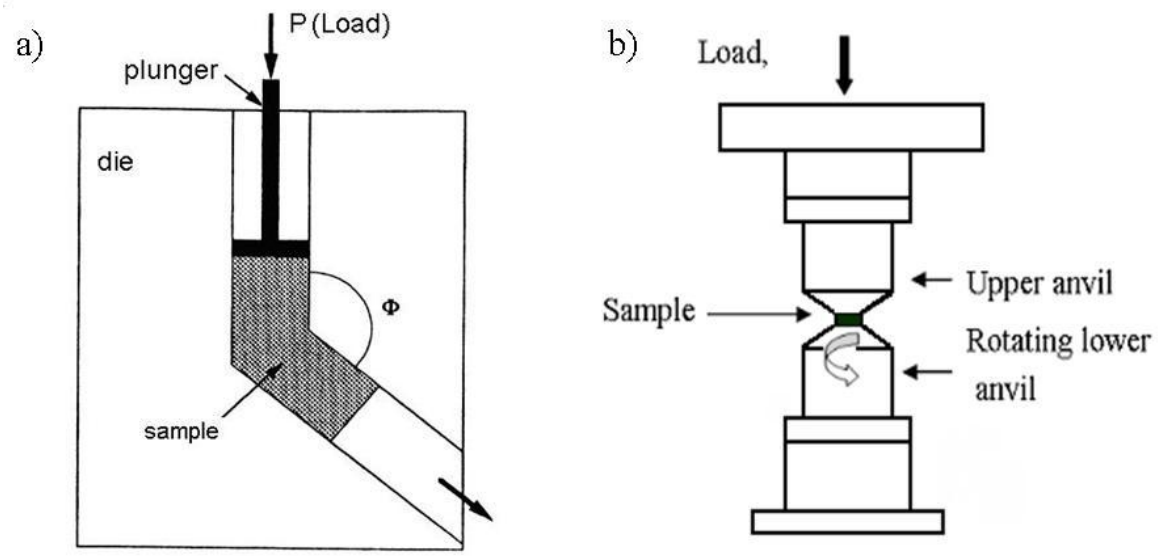


Figure 2.2 A schematic representation of SPD equipment: **(a)** equal channel angular pressing, **(b)** high pressure torsion.

Table 2.1 List of processing methods described in section 2.1 including operating principle, advantages and disadvantages

Method	First announcement	Operating principle	Advantages	Disadvantages
A bottom-up approach				
IGC	Gleiter H, 1981 [22]	An evaporation of the metal in inert gas, condensation on cold finger, collection and consolidation of nanocrystalline powder	High purity, bulk, grain size 5-10 nm	Porosity, high costs of the preparation equipment
ED	Erb, 1995 [25]	A nucleation of crystallites on the substrate surface and their subsequent growth along with the nucleation of new crystals.	grain size ~ 30 nm	Small dimension of samples, impurities
A top-down approach				
HPT	Smirnova et al., 1986 [35] Valiev et al., 1988 [36]	An ingot is placed between two anvils and strained in torsion under the applied pressure of several GPa.	High values of strain, grain size cheap	Relatively small dimensions of sample
ECAP	Segal, 1981 [31] Valiev, et al. [32]	A sample is pressed through equiaxed channels bended for a certain angle.	Large dimensions, big amounts, application	Min GS refinement 100 nm

2.2 Plastic deformation mechanisms in ultrafine grained and nanocrystalline fcc metals: results from experiments and molecular dynamic simulations

It is well known that the mechanical behavior of materials is determined by their deformation mechanisms while deformation mechanisms are controlled by the microstructure and defect structure of materials. Unique mechanical properties of nanostructured materials are attributing to their unique deformation mechanisms which in many cases are different from those in their cg counterparts. In conventional cg materials, the plastic deformation occurs mainly through dislocation slip and twinning. When a dislocation passes through a grain, it will deform the grain with the amount of the deformation equal to the Burgers vector of the dislocation. Dislocation sources required for sustained dislocation slip in cg materials include Frank-Read sources [37]. Twinning in coarse grained materials occurs through the pole mechanism [38], in which one partial dislocation forms a whole twin via climbing a screw dislocation pole to adjacent slip plane. However, when the grain sizes are reduced to a few tens nanometers, the pole mechanism for twinning and traditional sources for dislocation multiplication (the Frank-Read sources) no longer work. Besides, with the decreasing of grain size the grain boundary area increases that activates grain boundary mediated processes.

2.2.1 Slip of full dislocations

For cg materials with medium and high stacking fault energy (e.g. Cu, Ni, Al), slip of full dislocations is the primary deformation mechanism at room temperature and quasistatic strain rate.

With decreasing grain sizes and subgrain sizes below a few tens nanometers the traditional Frank-Read sources within the grain may no longer work, and grain boundaries become the sources and the sinks for slipping dislocations [3,4]. In other words dislocations are emitted from grain boundary (GB) segment and disappear into another GB segment without accumulation inside the grain interior.

It should be noted that it is possible for full dislocations to be trapped inside very small grains via dislocation interlocking and other mechanisms. The activation of full dislocations depends on the applied stresses. For nanocrystalline fcc metals and alloys with

grain size below 100 nm the slip of full dislocation may become less significant and other deformation mechanisms as partial dislocation slip and deformation twinning become more significant.

2.2.2 Slip of partial dislocations and twinning

Partial dislocation slip and deformation twinning are two different but related deformation processes. The early understanding of the partial dislocations and deformation twins was largely from the results of MD simulation because of experimental difficulties.

MD simulation predicted that partial dislocation emission from grain boundaries [39,40] is a dominant deformation mechanism in grains with a diameter in the range of several tens of nanometers. The activation of partial dislocations provides a critical precondition for the formation of deformation twins. Deformation twins have been predicted by MD simulations in nc Al [39], Ni [40], Cu [41], i.e. in materials with high–to-medium stacking fault energy (SFE), where deformation twinning had never been observed in conventional straining conditions. Three twinning mechanisms were suggested [39]: (1) homogeneous twinning inside nanosized grains by coincidental overlapping of wide stacking-faults ribbons. The stacking fault ribbons were formed by dissociation of lattice dislocation, and become very wide due to the effect of grain size as well as external stresses [42]. (2) Heterogeneous twinning from the grain boundaries. (3) Twinning by grain boundary splitting and migration. These mechanisms of deformation twinning have recently been experimentally verified in nc Al [42,43], Cu [42], Ni [44] and Pd [45]. Al in its cg state has never been observed to deform by twinning, except the crack tips, because of very high SFE. CG Cu does not deform by twinning except at very high strain rates and/or low temperatures. These results indicate that nc materials indeed deform via mechanisms not accessible to their cg counterparts, and grain size plays a critical role in the formation of deformation twins.

However, MD simulation does not tell what is the critical stress needed for the deformation twins to nucleate and to grow or what grain size is optimum for a deformation twin nucleation. Moreover, MD simulations naturally use extremely high strain rates in the order of 10^6 to 10^8 s^{-1} which correspond to “explosive deformation” in the real experiments. It is well known that the strain rate significantly affects the deformation

mechanisms of materials [42]. This adds complexity to the interpretation of the MD results.

Therefore, an analytical model based on the classical dislocation theory has been proposed to explain the nucleation and the growth of deformation twins in nc fcc metals [46]. The model suggests that the stress for twin growth is much smaller than that for the nucleation. The model also suggests that there exists an optimum grain size range in which deformation twins nucleate most readily. The critical twinning stress is found to be determined primarily by SFE, while the optimum grain size is largely determined by ratio of shear modulus to SFE.

2.2.3 Grain boundary mediated mechanisms

When the grain size is very small, grain boundary mediated mechanisms have been predicted as prevalent deformation mechanism [47,48]. With decreasing of the grain size it is easier for grains to align for geometric accommodation during grain boundary sliding (GBS). The mechanism of GBS was studied in detail in the 1980's due to interest in superplasticity. It was suggested as the dominant deformation mechanism of superplasticity.

Grain boundary sliding. One of the first model of GBS in nc materials were suggested by Hahn et al. [47]. The interface sliding model proposes that grain-boundary sliding controls the deformation mechanism, and that, in order to overcome grain-boundary obstacles that are triple junctions (TJ), several grain boundaries must cooperate to form a plane interface, what then by further interconnection with other plane interfaces, will lead to long-range sliding (Fig. 2.3). Such a migration involves a change in TJ geometry and more generally TJ migration. The developed structure might be associated with shear planes, where high plastic deformation is localized, resulting in a larger macroscopic deformation of nc metals.

A later result of MD simulation supports the picture presented by the interface sliding model. For example, Van Swygenhoven and co-workers [48,49] show that GBS is the primary deformation mechanism in nanocrystalline metals, such as Cu, and that such a sliding mechanism results in a build-up of stress across neighbouring grains. This stress is relieved by grain boundary and triple junction migration. The degree to which this occurs depends on the grain size since for small grain sizes more planar interfaces provide

reduced steric hindrance to concurrent grain boundary sliding. Furthermore, authors suggest that it is not only the grain boundary sliding takes place in nc materials, but also granular rotation and deformation via intergranular slip, which contribute to collective grain activity (Fig. 2.4).

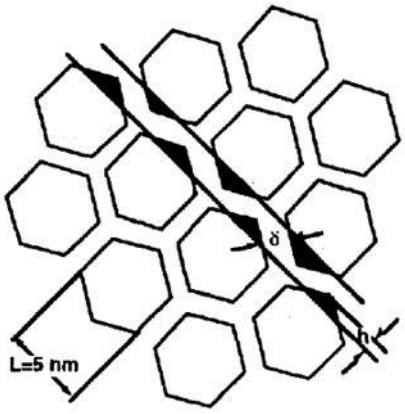


Figure 2.3 from ref [47] A schematic of a grain arrangement in a nc material. A mesoscopic planar interface can be formed by grain boundary migration. Atoms located in the darker regions have to be rearranged.

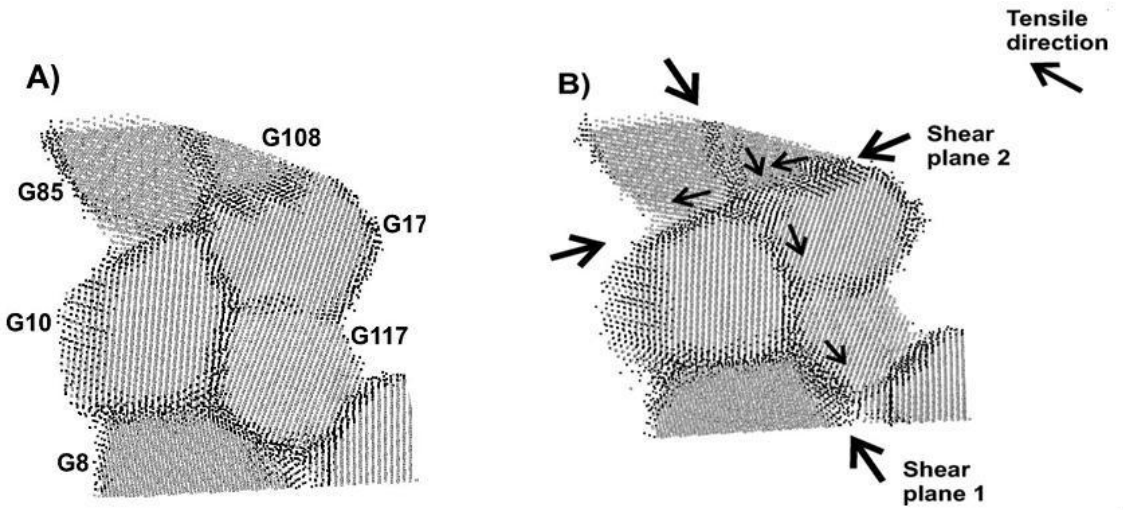


Figure 2.4 Cooperative shear planes formation in nc Ni after Ref. [49]: **(a)** is the atomic configuration before loading, and **(b)** after 3.6% plastic deformation.

Grain rotation. Recently, Ma and coworkers [50] observed that nanosized grains rotate during plastic deformation and can coalesce along directions of shear, creating larger paths for dislocation movement. They called it shear band. Fig. 2.5 shows this in schematic fashion. The orientations of the slip systems with highest Schmid factors are represented by a short line in each grain (Fig. 2.5a). As plastic deformation takes place, two neighboring grains might rotate in a way that brings their orientation closer together

(Fig. 2.5b). This leads to the elimination of the barrier presented by the boundary between them, providing a path for more extended dislocation motion (Fig. 2.5c). This mechanism can actually lead to softening and localization, and is consistent with the limited ductility often exhibited by nanocrystalline metals.

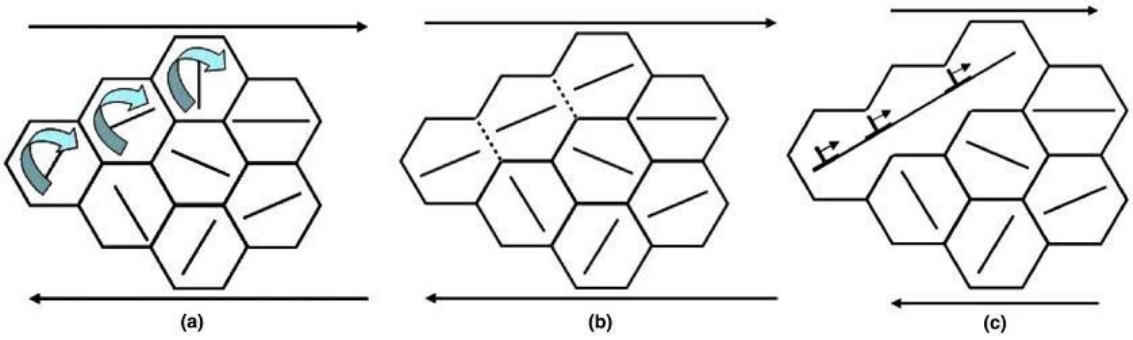


Figure 2.5 from Ref. [15] Rotation of neighboring nanograins during plastic deformation and creation of elongated grains by annihilation of grain boundary.

Deformation-induced grain growth. Nanocrystalline materials can undergo significant grain growth at ambient conditions [29,51]. Plastic deformation further accelerates the growth [52,53,54]. Accelerated grain boundary migration has been directly observed by transmission electron microscopy (TEM) during *in-situ* tensile tests of nc Al thin film samples [52]. The stress assisted mechanism for which several explanations have been proposed including interaction of the external stress with grain boundary dislocations [55,56] and the shear-coupled motion of grain boundaries [57]. In conditions when the microstructure is not stable during deformation because of the stress-induced grain growth, it should be possible to observe the change of the primary deformation mechanism. Such change has been recently revealed during an *in-situ* tensile test in Al nc film, when activity of full dislocations was registered in grains which diameter had increased up to a certain size. Stress-induced room temperature grain growth in nc materials was reported for the first time in nc Pd in cold rolling experiments [17]. Subsequently it was observed in HPT-processed electrodeposited Ni [53], under microindentations of nc-Cu [54] compressively deformed nc-Ni [58], tensile strained Ni–Fe and Co–Pd alloys [59,60], and by direct observations *in-situ* in TEM in nc Al films [41].

2.3 Balance of high strength and good ductility in nanocrystalline materials

Since their discovery more than 20 years ago, nc materials attract attention due to their superior hardness, strength and fatigue properties as compared to their coarse grained counterparts. Furthermore, it has been long predicted by Gleiter and co-workers [8] that nc materials could show increased ductility due to activation of grain boundary and diffusional deformation mechanisms. However, these expectations were not realised and mostly nc materials show limited ductility in tension. As reasons of low ductility many researches point out either drawbacks from synthesis or that grain boundary mechanisms are not as effective as deformation mechanisms associated with generation and movement of dislocations

This section shortly discusses main concepts to achieve high strength and good ductility. Only f.c.c. metals will be covered here, because they are the class of metals for which systematic data sets are available.

2.3.1 Strengthening mechanisms

As it was shown in section 2.2, dislocations are most effective carriers for plasticity in crystalline solids. An interaction of mobile dislocations with obstacles leads to an increase of the level of flow stresses, hence to the strengthening of a material. Several strengthening mechanisms take place in metals: lattice resistance, grain size strengthening, solute hardening, precipitation hardening and dislocation hardening.

In pure closed packed f.c.c. and h.p.c. metals, the lattice resistance in the best slip systems is normally very small, making it necessary to introduce other extrinsic mechanisms to raise the plastic resistance. This can be accomplished by alloying with the second constituent, which, either in the form of solid solution or as precipitate particles in the host metal, effectively elevates resistance to dislocation motion due to effects of elasticity.

The most effective strengthening mechanisms in nanocrystalline metal however is grain size strengthening. Furthermore, storage of dislocations and nano-twins inside ultra-fine grains leads for further strengthening.

2.3.1.1 The grain size strengthening

The yield strength of polycrystalline metals is generally observed to increase as the grain size decreases according to the empirical Hall–Petch (H–P) relationship [1,2]:

$$\sigma = \sigma_0 + K_d d^{-1/2}, \qquad (2.1)$$

where d is the grain diameter, σ is the yield strength, and σ_0 and K_d are material dependent constants. A physical basis for this behavior is associated with the difficulty of dislocation movement across grain boundaries and stress concentration due to dislocation pile-up. Based on Eq. 2.1, metals with nanoscale grains should be much stronger than their coarse grained counterparts. But stress plateaus or even stress drops were observed in materials when grain size decreased into the range of 10-20 nm (Fig. 2.6). The exact grain size range when a flow stress drops depends on the material and remains uncertain.

Explanations offered for reduced or even negative H-P slope in the nanocrystalline grain size range include activation of the room-temperature creep [8], onset of grain boundary sliding [61], approach to amorphous state (the amorphous phase is supposed to be weaker than the crystalline phase) [62], and nucleation of cracks/voids in triple junctions [63]. In recent experiments several authors [64,65,66] measured an activation volume in ED nc Ni in tensile testing, and found a value of about $10b^3$, where b is a Burgers vector. This value is one magnitude higher than it would be expected for the Coble creep ($\sim 1b^3$), suggesting a minor role of the Coble creep hypothesized by earlier authors. The grain-boundary sliding (see section 2.2.3) was proposed by MD simulation [61,67] and later observed during *in-situ* transmission electron microscopy experiments in nc Ni with an average grain size of 10 nm [68,69]. The GBS hypothesis provides a possible explanation to the abnormal H-P slope observed so far from experiments. The question remains, however, as to what grain size the transition occurs and how it depends upon different materials systems. It is difficult to experimentally pinpoint such transition grain size. There are several factors that complicate this issue. The majority of samples contain porosity and/or contaminations; the average grain size used in H-P relation is usually obtained from X-ray measurements, which alone does not represent the internal structure of nc materials with grain size distribution. Other factors, such as twin boundaries and impurities, could also impact the measured hardness/strength.

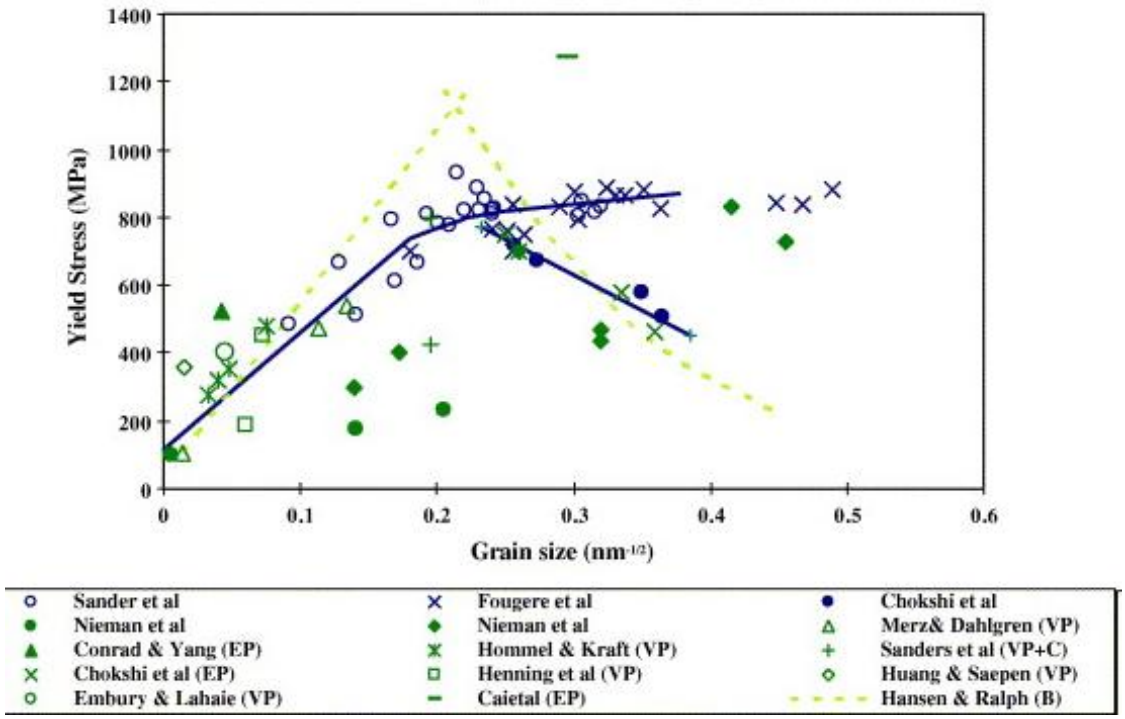


Figure 2.6 after Ref. [15]: The combined Hall-Petch relation for Cu

Nano-twins. A twin boundary is a special kind of grain boundary that can effectively impede the motion of dislocations and increase the strength of the materials. By introducing a high density of nanoscale growth twins, Lu and coauthors [70,71] demonstrated a significant size-dependence of mechanical properties on the twin lamellar spacing, much like the grain size dependence of the strength in nc metals. With increasing of twin density, or decreasing twin lamellar spacing, the strength of nano-twined Cu samples increased gradually. It was suggested by Lu and collaborators, that the strengthening effect of twin boundaries is analogous to that of conventional grain boundaries in Cu.

2.3.1.2 Strengthening by storage of dislocations inside of grains

Strain hardening, alternatively referred as work hardening, first tackled by Taylor [72], results from the interaction of strain fields of dislocations as more and more introduced during plastic flow. In Taylor's formula yield stress can be written:

$$\sigma = \alpha G b \sqrt{\rho} \qquad (2.2)$$

where b is the Burgers vector, ρ is the dislocation density and α is the geometrical constant that lies typically in the range $0.1<\alpha<0.5$. In general terms this expression (Eq.

2.2) relates the yield stress to the inter-obstacle spacing, which for the ensemble of dislocation with density ρ is approximately equal to $1/\sqrt{\rho}$.

The strain hardening of nc materials has been documented recently. In some cases (in most of them metals were produced by electrodeposition), (1) nanocrystalline metals are found to exhibit strong strain hardening up to failure [71,73,74]; whereas in others, (2) little strain hardening was observed [18]. The mechanism responsible for the strong strain hardening (1) in nc metals produced by ED is not clear yet. The stress increase could arise from an "exhaustion" phenomenon, possibly due to gradual exhaustion of grain boundary dislocation sources, and/or increase of the internal stress as a result of grain boundary sliding [61,67]. Another possibility is the gradual involvement of grains with different grain sizes in a deformation process due to presence of grain size distribution [75].

In case of materials of the second type (2), a short region of strain hardening (1-3%) is followed by a long region of negligible work hardening or even softening; this behaviour is different from that of single crystals or polycrystalline materials, which typically show strong strain hardening to very large strains. Such nanostructured metals were mostly prepared by SPD and their deformation behaviour is easy to understand. This is because the refinement of originally large grains into nano-/ultrafine-grained structure is achieved though accumulation and rearrangement of dislocations. These materials usually contain a high density of dislocations and other defect structures, similarly to the late work hardening stage of heavily deformed conventional metals. The strain hardening rate in these metals is very low because the density of dislocations reaches a saturation level in the presence of dynamic recovery. Described low strain hardening behaviour has been observed in samples processed by ECAP [76,77].

2.3.2 Ductility

The *ductility* of material is usually defined as the ability to plastically deform without failure under external stress.

In conventional coarse-grained (1-100 μm) engineering materials, the tensile ductility sometimes increases with decreasing grain size, due to effects of small grain sizes on nucleation and propagation of cracks. In contrast, the tensile elongation to failure of nanostructured materials (Fig. 2.7) decreases monotonically with increased strength (with several exceptions) [75]. A similar trend has been observed in other ns materials. However,

despite such a decrease of tensile elongation, nanocrystalline materials are intrinsically ductile, judging from the often-seen ductile dimples in fracture surface. These dimples have a size significantly larger than the grain sizes. It has been proposed, that the dimples are formed thought collective shearing of a group of nanograins during deformation [78].

Koch et. al. [79] pointed towards three major sources for the low tensile ductility observed on nanostructured materials. They are (1) processing porosities and imperfections; (2) tensile instability; (3) crack nucleation or propagation instability, where the imposed stress at an existing flow exceeds the critical toughness of the material. The first source is processing related and somewhat material-system dependent. With improvement of processing routes, porosity- and contamination-free nanostructured samples have become available to avoid such problems.

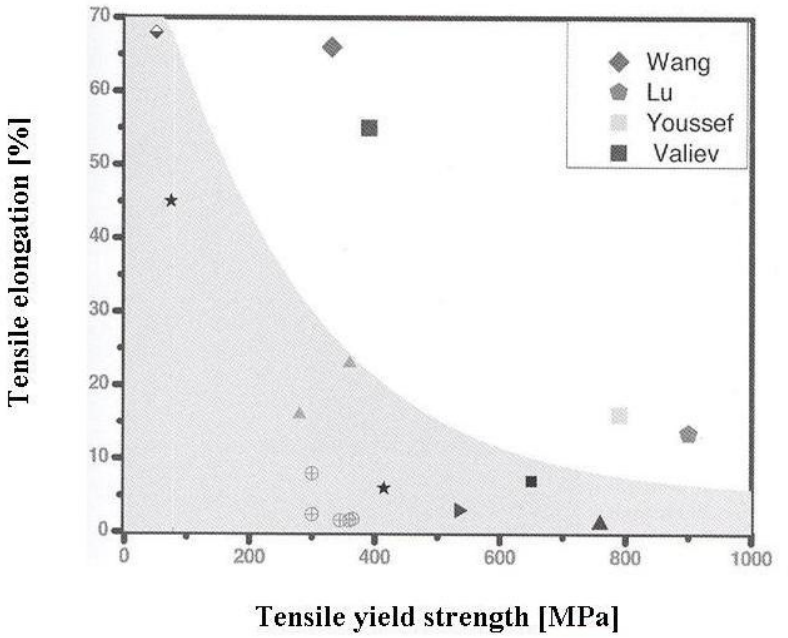


Figure 2.7 After Ref. [75] Summary of tensile yield strength vs tensile elongation to failure in various nanostructured copper from open literature. In general, the tensile ductility decrease with increasing strength. The few promising data pointing the good combination of strength and ductility are from Wang [80] (bimodal structure), Lu [71] (nano-twins), Yossef [81] (*in-situ* consolidated high purity Cu), Valiev [82] (increased m).

The tensile instability is closely tied to strain hardening rate and strain rate sensitivity, both of which are indicative of intrinsic resistance of nanostructured materials to strain localization. According to Hart's criterion for strain-rate sensitive materials [83],

$$\frac{1}{\sigma}\left(\frac{d\sigma}{d\varepsilon}\right)_{\dot{\varepsilon}} + m - 1 \leq 0 \qquad (2.3),$$

where the first term is a normalized strain hardening rate, and the second term is the strain rate sensitivity. The tensile instability sets in when the condition in Eq. 2.3 is reached. According to this criterion, high stain hardening rate and/or strain rate sensitivity help to prevent early necking and prolong the tensile elongation to failure.

A majority of nanostructured materials exhibit low strain-hardening rate. The strain hardening behavior of ns materials are affected by a number of structural parameters such as grain size distribution, dislocation density, internal stresses, presence of twin boundaries and low/high angel boundaries, stacking fault energy, and so forth. Usually, stress-strain curves of these materials show failure immediately after onset of yielding [18]. Such behavior is related to limited dislocation storage in small grains (section 2.3.1.2). On the other hand, nanostructured materials prepared using SPD contain high dislocations density and dynamic recovery occurs as a deformation progresses, which also leads to limited strain hardening rates. It is expected that any improvement of strain hardening will be beneficial for the ductility, i.e. enhancing the uniform elongation, in ufg materials [14].

Of equal importance, the strain rate sensitivity of ns materials also has a direct impact on the tensile ductility. The enhanced strain rate sensitivity slows down early necking and prevents catastrophic failure. For example, for *m* a value of 0.14 was reported at room temperature in an ECAP Cu after 16 passes by Valiev and co-authors [82]. Tensile results revealed a very large tensile elongation to failure of over 50 % (one of the exceptions in Fig. 2.3.2)

The decrease of the grain size down to the nanometer regime, on the other hand is potentially conductive to reduce the flaw size (which is of the same order as the grain size) that subsequently helps to suppress the crack nucleation and propagation. It is known from conventional materials that both yield stress and fracture stress increase as a grain size decreases, with fracture strength increasing faster. Given the strong increase of flow stress with decreasing grain size at the nanoscale, the competition between plastic flow and fracture becomes difficult to predict.

As a tensile ductility is of crucial importance to structural application, in recent years several approaches were developed to improve this critical mechanical property, such as generating bimodal grain size distributions, nano-twins, dispersion of nano-particles, etc.[19]. A quite current method is to increase the ductility by alloying with specific

materials with the purpose of decreasing the stacking fault energy (γ_{SF}) as shown in Refs. [20,21].

Approaches to improve ductility:

(a) *Bimodal Microstructure*. A useful strategy is to develop a bimodal or even multimodal grain structure with micrometer-sized large grains embedded in nano- or ultrafine-grained matrix (one of the exceptions shown in Fig. 2.7). As such, the nanograins impart high strength, whereas the micrometer-sized grains provide strain hardening mechanisms and potentially high tensile ductility. By adjusting the volume fraction, size, shape, and the distribution of coarse grains, one has ample room and opportunities to tailor the mechanical properties of nanostructured materials, to optimize strength, ductility, or a combination of both. Note that a porosity-free highly uniform nanocrystalline structure is not only extremely difficult to process but also not necessary or beneficial for properties and structural application. In fact, for most nanocrystalline metals that showed ductility, the microstructure usually contains a certain fraction of larger grains. In a more generic case, the larger grains can also be ductile second-phase particles, or dendrite structure, which will act as a roadblock for shear localization or crack propagation [84].

(b) *Nano-twins.* As it was described afore, a twin boundary can effectively impede the motion of dislocations and increase the strength of the materials. At the same time twin boundary also allows nonglissile partial dislocations to deposit on its twin plane and accommodate plastic deformation. In addition the twin lamellar structure may be viewed as inherently bimodal, because the long scale parallel to twin boundaries is significantly larger then nanoscale twin lamellar width. Twins can accumulate and form tangles, cutting the twin ribbons into cells. High density twins (Fig. 2.8) can be produced using electrodeposition by increasing the current density and lowering the temperature during deposition [70].

(c) *Dispersion of nano-particles*. The high strength and the high ductility have also been achieved in certain nanostructured alloys (Al alloys, steels) through precipitation/aging [85]. In ns grains, the hard precipitates also initiate, drag, and pin dislocations thus reducing the dynamic recovery. The result is a significant dislocation storage required for compatible plastic strains, allowing a high strain-hardening rate that leads to larger uniform strains while elevating strength. To promote the precipitation of a

large population of nanoparticles, SPD is often involved in the processing to pump in extra defects to increase nucleation sites.

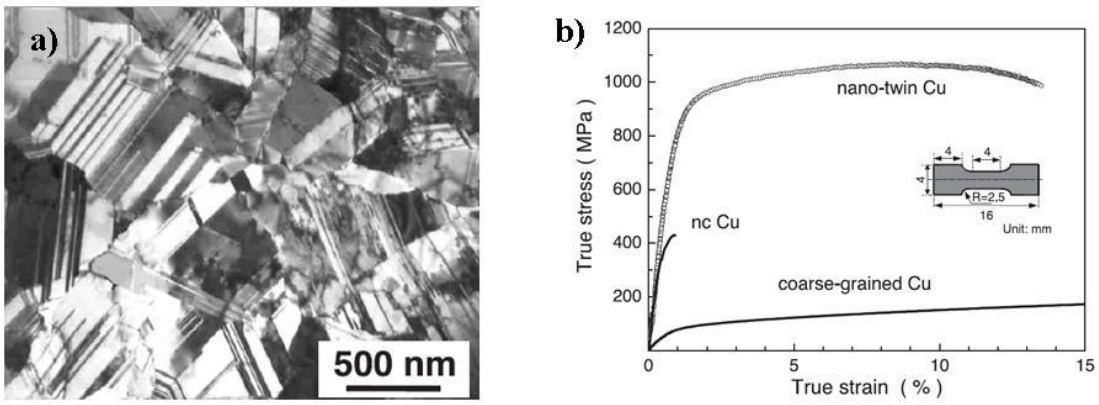


Figure 2.8 (a) A bright-field TEM image of the typical microstructure in an as-deposited Cu sample. **(b)** A typical tensile stress-strain curve for the as-deposited Cu sample with nano-twins in comparison with that for a coarse-grained polycrystalline Cu sample (with an average grain size larger than 100 μm) and nc Cu sample (mean grain size ~ 30 nm) [70].

(d) *Annealing*. Some ns materials prepared by SPD bear similarity with heavily worked samples; it is conceivable that annihilation and recovery of stored dislocations through proper heat treatment could help to regain strain hardening in these metals and thus to achieve a higher value of tensile elongation. Thermal treatment could also help to optimize the non-equilibrium grain boundary structure and improve the mechanical properties. Note that high-temperature annealing is not an option in this situation, as excessive grain growth will occur. A concurrent increase of strength and ductility after low-temperature annealing has been indeed seen in several ECAP metals [86].

Chapter 3

Materials synthesis and analytical methods

3.1 Materials for investigation

As a material we used Pd, Pd-10 at.% Au, and Pd-*x* at.% Ag (x=5,10,20,40).

Pd and Pd-*x* at.% Ag (x=10, 20, 40) samples were alloyed by heating and melting in an arc-melting oven under Ar atmosphere at the Universität des Saarlandes, FR7.3 Technische Physik. According to the phase diagram the Pd-Ag system is completely soluble (Fig 3.1a) [87]. The physical properties (melting temperature [87], elastic shear modulus [88], stacking fault energy [89]) and the initial microhardness of the investigated materials are presented in Table 3.1. The stacking fault energy of Ag (22 mJ/m^2) is significantly lower than that of Pd (169 mJ/m^2). Therefore addition of Ag dramatically decreases the stacking fault energy (γ_{SF}) in Pd-Ag alloys (Table 3.1).

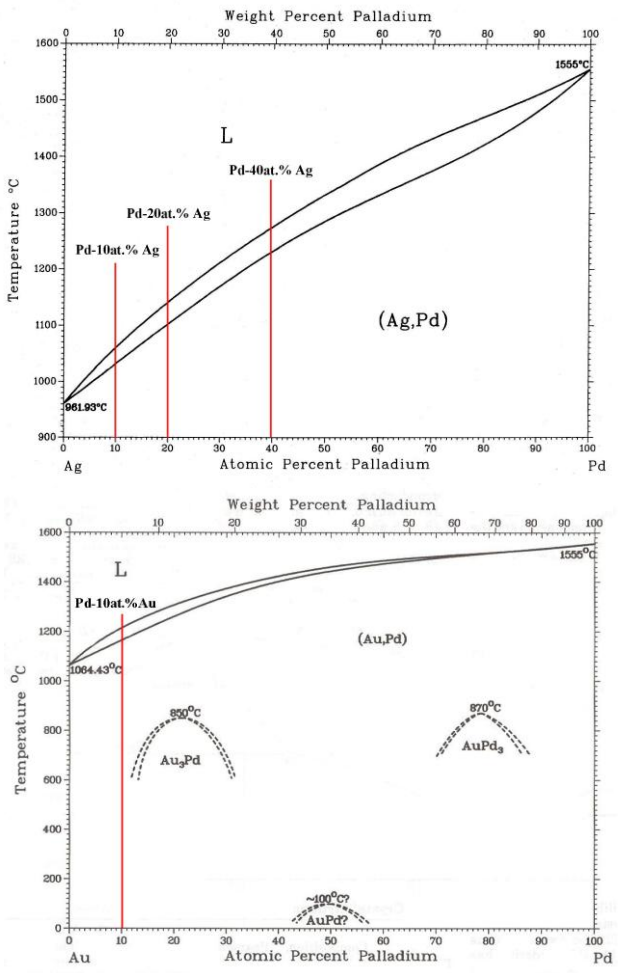


Figure 3.1 After Ref [87]: Phase diagrams of **(a)** Pd-Ag system and **(b)** Pd-Au system. Red lines show composition which we used in the recent work.

Pd-Au systems are also characterized by solute solubility (Fig 3.1b). Materials were prepared by inert gas condensation at the Universität des Saarlandes, FR7.3 Technische Physik. Initial microstructures of as-IGC Pd and as-IGC Pd-10at.% Au were uniform (Fig. 3.2a,c) with a mean grain size of 14(1) nm and 13(1) nm for Pd and Pd-10 at.% Au, respectively. Careful inspection revealed very few twins in as-IGC microstructure. Dislocations can be observed only in a small fraction of grains. Triple points exhibit angles near 120°, as in an equilibrated grain microstructure.

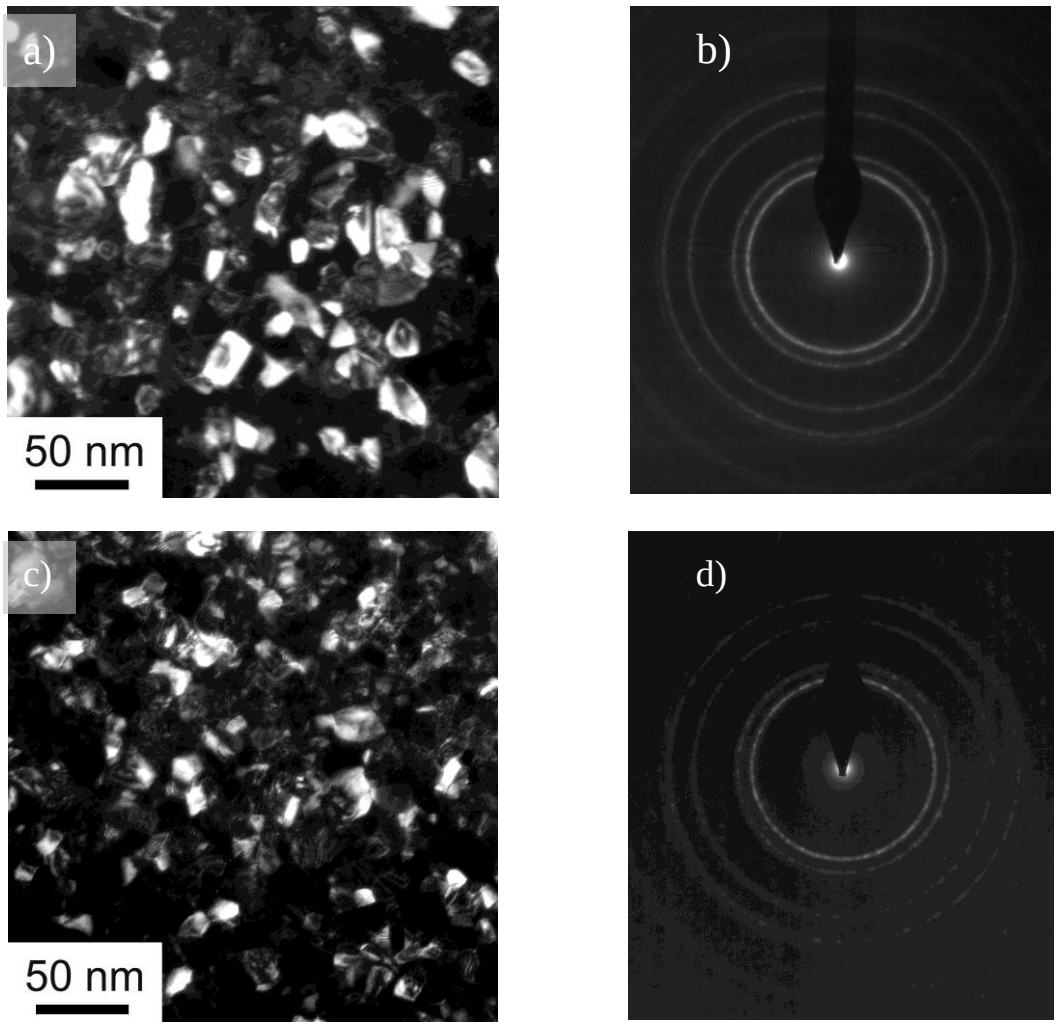


Figure 3.2 Microstructure of nanocrystalline Pd **(a,b)** and Pd-10 at.% Au **(c,d)** in as-IGC state: dark-field images using 111 reflections **(a,c)** and selected area diffraction patterns as insert **(b,d).**

Table 3.1 List of physical properties: melting temperature (T_m) [87], elastic shear modulus (G) [88], stacking fault energy (γ_{SF}) [89] and initial hardness of studied alloys.

	T_m [°C]	G, [GPa]	γ_{SF} [mJ/m^2]	Initial microhardness [HV]
Pd	1555	46.2	179	42(5)
Au	1064	78	32	-
Pd-10Au	1200	49.4*	150**	-
Ag	962	29.4	22	31(1)
Pd-10Ag	1510	44.5*	165.3	45(4)
Pd-20Ag	1470	42.8*	125	66(10)
Pd-40Ag	1385	39.5*	118.7	62(8)

*Shear module of Pd-Ag and Pd-Au alloys were estimated from Young's modulus of pure Pd, Ag, and Au using the rule of mixture.

**Stacking fault energy is estimated using EAM potential, courtesy of Dr. Karsten Albe (TU Darmstadt)

3.2 Processing methods

Samples were processed by the inert gas condensation and high pressure torsion, as well as combination of both techniques.

3.2.1 Nanocrystalline specimens

Nanocrystalline samples have been produced by IGC technique (see section 2.1.1), using a 10^{-7} mbar base pressure vacuum system and thermal evaporation of pure metal in a 1 mbar helium atmosphere. The powder was consolidated *in-situ* at a pressure of 2 GPa in order to obtain disc-shaped specimens with a diameter of 8 mm and thickness of typically 200-1000 μm (Fig. 3.3, right sample). A relative density of as-IGC pellets was 91 %. Because of the rapid grain growth at room temperature [29], the specimens were stored in liquid nitrogen when not under investigation.

3.2.2 Ultrafine grained specimens

Because of some residual porosity of as-IGC materials some pellets were additionally consolidated using HPT (for description of method see section 2.1.3.2) under a pressure of 4-6 GPa with different number of revolutions (n = 0.5, 2, 5). After this treatment the density of nanocrystalline samples was about 98-100 % of the density of bulk material. Archimedes density measurements were performed with air and diethylphtalate as independent media. The HPT consolidation of as-IGC Pd was done initially using special HPT facilities at Ufa State Aviation Technical University (in collaboration with Prof. Dr. Ruslan Valiev). Furthermore, we used a Schenck™ compression-torsion testing machine in IMF-II, KIT CN (Karlsruhe, Germany) with an axial load capacity of 400 kN with limited angular range of rotation.

Coarse grained ingots of Pd and Pd-x at.% Ag (x = 10, 20, 40) samples were processed by HPT under quasi-hydrostatic pressure of 6 GPa for five revolution in Ufa State Aviation Technical University (Ufa, Russia). The final dimensions of the HPT-disks were about 10 mm in diameter and 0.3 mm in thickness (Fig. 3.3, left sample).



Figure 3.3 View of the samples prepared by IGC (on the right) and IGC+HPT (on the left).

3.3 Microstructure characterization

The microstructure characterization we performed using transmission electron microscopy (TEM) and X-ray diffraction (XRD).

3.3.1 X-ray diffraction (XRD)

The X-ray line-broadening analysis of diffraction patterns is a simple and reliable method for the characterization of the microstructure and, most prominently, the grain size. Quantitative XRD measurements of the samples were performed using a Philips X'Pert diffractometer (INT, KIT CN).

Crystallite size and microstrains (elastic lattice strains) were estimated from the XRD peak broadening (Fig. 3.4a) using the modified Williamson-Hall method [90,91]. For an estimation using Williamson-Hall method, we need information of the peak parameters (peak position and intensity, full width at half maximum (FWHM) and integral breadth) from X-ray diffractions. The peak parameters were defined by fitting a Pearson VII function to the measured peak in the software Phillips Profil Fit 1.0. All reflections with Miller indices up to (4 2 0) were used for grain size and microstrains estimates. Furthermore, it is necessary to correct measured data for instrumental broadening. A LaB_6 standard by NIST was used to determine this correction.

The reflection width can be described as:

$$\delta k = \frac{2\pi K}{\lambda}\cos\theta\delta(2\theta) \qquad (3.1),$$

where λ is the wavelength, θ is the half of scattering angle, $\delta(\theta)$ is the FWHM.

The Scherrer formula [92] describes the contribution of size broadening to δk,

$$\delta k_{\text{size}} = \frac{2\pi K}{L} \qquad (3.2),$$

where L is the length of the diffraction column of unit cells and $K = 0.83$ denotes the Scherrer constant. For isotropic microstructure, value of L scales with crystalline size D according $L = 3D/4$ [93], a relation which we adopt here.

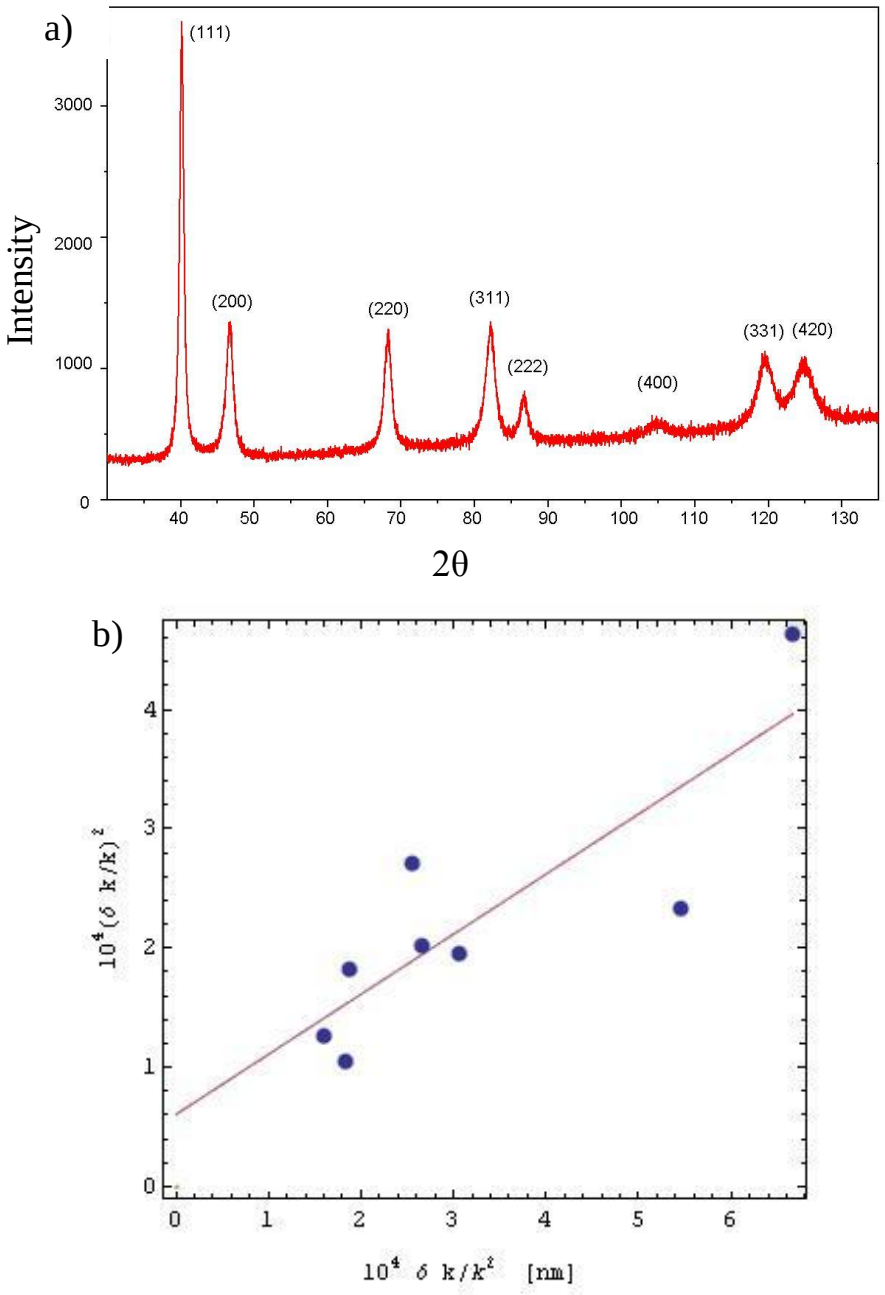


Figure 3.4 (a) Typical X-ray diffraction of nc Pd (λ_{Cu}=154.183 pm). Numbers in brackets are reflections with Miller indices. **(b)** Willamson-Hall plot of nc Pd XRD shown in (a).

The microstrain broadening arises from local variation of lattice parameter about its mean. Its effect on the peak broadening is usually expressed as

$$\delta k_{\text{strain}} = 2\varepsilon k \qquad (3.3),$$

where ε is the microstrain.

The deconvolution of the size- and strain-contributions to the peak broadening is typically based on assumptions on the functional form of the contributions. It is typically assumed that the size-broadening is Lorentzian and the strain broadening is Gaussian [90]. By analysis of the convolution of the two functions, one obtains the following expression for the net broadening, δk, due to the combined strain- and size-effects:

$$\frac{\delta k_{\text{size}}}{\delta k} = 1 - \left(\frac{\delta k_{\text{strain}}}{k} \right)^2 \tag{3.4}$$

In terms of Eqs. 3.2 and 3.3, one then obtains the modified Williamson-Hall relation:

$$\frac{(\delta k)^2}{k^2} = \frac{2\pi K}{3D} \frac{\delta k}{k^2} + 4e \tag{3.5},$$

Eq. 3.5 has a line form $y=bx+a$ where $x=\delta k / k^2$ and $y=\delta k^2 / k^2$ Thus, in the plot (Fig. 3.4b) of $\delta k^2 / k^2$ vs $\delta k / k^2$ the slope measures the inverse crystalline size and the ordinate intercept measures the magnitude of microstrain.

Besides conventional XRD measurements in the present work we used data of synchrotron XRD measurements with a correction for residual stresses. These measurements were performed using the synchrotron ANKA at KIT CN by Dr. Stephen Doyle. We used similar procedure as described afore for calculation of grain size and microstrain. Furthermore, we were interested in an evaluation of the lattice parameters (a) and stacking fault probabilities (α_{SF}) [94] that needs a special route of correction for residual stresses. This procedure was necessary because severe deformation is characterized by very high residual stresses in the processed specimens.

Residual stresses cause shifts of XRD peaks, and consequently, may affect the results of the estimation of the lattice parameter or stacking fault probability out of peak positions and peak shifts. It was shown, that by tilting of the sample with respect to the XRD diffraction plane at a certain angle (angle Ψ in a standard Eulerian coordinate system), the influence of the residual stresses on the position of a certain XRD peak can be eliminated [95]. For Pd these tilt angles are quite similar for all crystallographic directions at about 48° (see [95] for details). Therefore the synchrotron XRD measurements used for the determination of the lattice parameter and the stacking fault density were performed at this angle using an Eulerian cradle. As residual stress does not influence the estimate of the volume averaged crystallite size and the average amount of microstrain, these values were estimated using the X-ray diffractograms measured at Ψ=0°.

The Warren stacking fault (α_{SF}) probability parameter were determined using the Nelson-Riley method, that measures the number of density of stacking faults, by analysis of reflection position. The estimation was done using the software *Mathematica* and Notebook written by Jürgen Markmann and described in Ref. [96].

3.3.2 Transmission electron microscopy (TEM)

Samples for transmission electron microscopy (TEM) were prepared using several techniques:

1. electropolishing using Tenupol 5 electropolishing apparatus (Struers A/S, Denmark);
2. mechanical grinding and following thinning to thickness of electron transparency using Gatan Precision ion polishing system (PIPS, Gatan, USA);
3. using focus ion beam (FIB) FEI 400.

Foils of Pd were electropolished with a BK-2 electrolyte [97] at -20°C and at a voltage of 60V using a Tenupol 5 electropolishing apparatus (Struers A/S, Denmark).

3 mm discs of Pd-10 at. %Au with 100 μm thickness were mechanically grinded and dimpled, then further thinned to a thickness of electron transparency using a Gatan PIPS with an Ar^+ ions accelerated at 2,0-3,5 kV.

For the preparation of thin foils from Pd-Ag alloys a two-step procedure was applied. Initially foils were mechanically grinded and dimpled, then they were thinned to a thickness of electron transparency using a Gatan Precision Ion Polishing System (PIPS, Gatan, USA) with an Ar^+ ions accelerated at 2,5-3,5 kV. In order to remove the ion damaged layer from the thin foil surfaces, further electropolishing with an electrolyte BK-2 at a temperature of -20^o C and at voltage of 60 V was applied.

Preparation of TEM lamellas from deformed parts of samples after tensile or compression tests was done by means of focus ion beam (FIB) by Torsten Scherer (INT, KIT CN, Karlsruhe). Location of the foil was defined inside of the FIB.

For conventional bright- and dark-field imaging a Phillips CM 30 operated at 300 kV was used, and high-resolution microscopy was conducted using an FEI Tecnai F20 G^{2e} operated at 200 kV.

TEM foils from HPT samples were taken from a location corresponding to the gauge section of tensile specimen and approximately situated at a distance of 3 mm from the sample centre (Fig. 3.5).

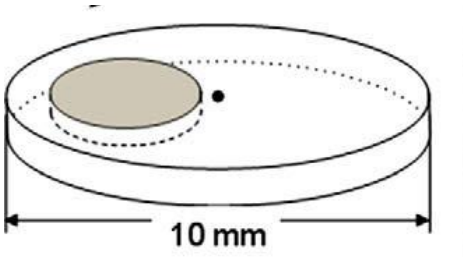


Figure 3.5 Schematic diagram of sample cutting from an as HPT disc for TEM investigation. The grey circle indicates the position of the TEM thin foil and situates at a distance of 3 mm from the sample centre.

The mean grain size was estimated using a line interception method [98] in representative dark-field TEM images. The line interceptions were measured in two directions: in the direction of shear deformation during HPT, and perpendicular to it. The final grain size was calculated as the average between length and width. For a statistical distribution of the grain sizes a total of 150-300 grains were measured for each analysis.

3.4 Mechanical property tests

Mechanical properties of investigated materials were studied using hardness measurements, tensile, compression and compression-torsion tests.

3.4.1 Hardness measurements

Vickers hardness was measured using the microhardness testing machine Buehler™ Micrometer 5104 with operation box. The investigated specimen is indented by applying the test force using a regular quadrangular pyramid diamond indenter whose face-to-face angle is 136 degrees. The indentation has a diamond-shape. The Vickers hardness of specimens is found by dividing test force "*F*" by the surface area "*S*" of an indentation, which is estimated from the average diagonal length of the indentation. All indentations were done with testing force 300 g. during 15 s. At least 10 measurement points were done for each sample.

3.4.2 Tensile and compression measurements

3.4.2.1 Background on mechanical tests

The stress-strain behaviour of materials is generally defined from a monotonic tensile test on a smooth specimen (Fig 3.6a). For such a specimen:

$$\sigma_{eng} = \frac{P}{A_0} \quad (3.6),$$

$$\varepsilon_{eng} = \frac{L - L_0}{L_0} = \frac{l}{L_0} \quad (3.7),$$

where P is the applied load, A_0 is the initial cross-sectional area of the specimen, L_0 is the initial length, L is the instantaneous length, and l is the displacement. Since the cross-sectional area changes during deformation, the true stress, which is greater that the engineering stress in tension (conversely, less in compression), is defined as:

$$\sigma_{true} = \frac{P}{A} \quad (3.8)$$

where A is the instantaneous area. Likewise, the true strain is less than the engineering strain in tension up to necking and can be calculated as:

$$\varepsilon_{true} = \int_{L_0}^{1} \frac{dL}{L} = \ln \frac{L}{L_0} \qquad (3.10).$$

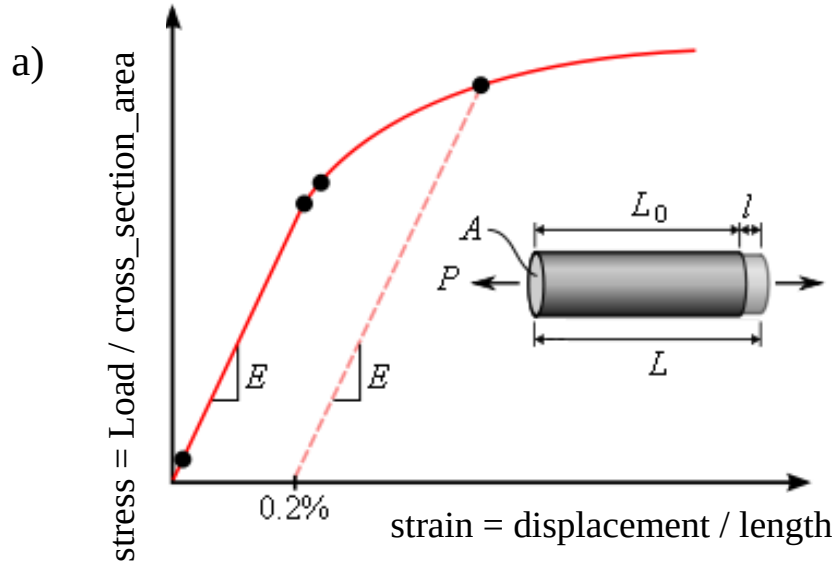


Figure 3.6 As schematic representations of: **(a)** stress-strain curve; **(b)** strain rate (jump) test curve.

The relation between the engineering stress and strain and true stress and strain comes from:

$$L = L_0 + l \qquad (3.11).$$

Combining Eq. 3.7, Eq. 3.10 and Eq. 3.11, one can obtain:

$$\varepsilon_{true} = \ln\left(\frac{L_0 + l}{L_0}\right) = \ln\left(1 + \frac{l}{L_0}\right) = \ln(1 + \varepsilon_{eng}) \qquad (3.12)$$

Plastic deformation is a constant-volume process, therefore:

$$A_0 \times L_0 = A \times L = const \tag{3.13}$$

$$\frac{A_0}{A} = \frac{L}{L_0} \tag{3.14}$$

To relate the true stress to the engineering stress, from Eq. 3.6, Eq. 3.14, and Eq. 2.2:

$$\sigma_{true} = \frac{P}{A_0} \times \frac{L}{L_0} = \sigma_{eng}\left(1 + \varepsilon_{eng}\right) \tag{3.15}$$

For compression tests true stress is estimated as:

$$\sigma_{true} = \sigma_{eng}\left(1 - \varepsilon_{eng}\right) \tag{3.16}$$

Except conventional tensile or compression test at different strain rate, strain rate jump test (Fig 3.6 b) were performed at room temperature to determine stress-strain parameters of deformation (strain rate sensitivity m and activation volume ΔV) according a kinetic analysis. The strain rate varied between $5x10^{-4}$ s^{-1} down to $1x10^{-4}$ s^{-1}. Fig 3.8b schematically represents strain rate jump tests: a tensile test is carried out at a strain rate $\acute{\varepsilon}_1$ and a certain flow stress σ_1; then at some point the strain rate is quickly increased to $\acute{\varepsilon}_2$, the material reacts by increasing of the flow stress to σ_2. The strain rate sensitivity (m) and activation volume (ΔV) are estimated as:

$$m = \frac{\log(\sigma_2 / \sigma_1)}{\log(\dot{\varepsilon}_2 / \dot{\varepsilon}_1)} \tag{3.17},$$

$$\Delta V = \frac{\sqrt{3} kT \ln(\dot{\varepsilon}_2 / \dot{\varepsilon}_1)}{\sigma_2 - \sigma_1} \tag{3.18}$$

where *T* is the temperature, *k* the Boltzmann constant.

For more detail for a formula derivation see Appendix A

3.4.2.2 Experimental procedures

As it was shown in Fig. 3.3 sizes of the tested samples are limited by a diameter of 10 mm. Therefore all mechanical tests were carried on an especially dedicated tensile stage (Fig. 3.76) for miniature specimens.

All uniaxial tensile tests were performed using miniature specimens with a gauge length as small as 1.4 mm at room temperature at a range of strain rates from 10^{-2} s^{-1} down to 10^{-5}

s^{-1}. It is well known, that dimensions of the tensile specimens can influence the resulting mechanical properties, primarily the measured elongation. That is why dimensions of tensile specimens are fixed in corresponding standards [99]. The specimen sizes used in the present investigation do not meet these standards; therefore uniform and total elongations obtained cannot be compared with results of tensile tests performed using specimens having other dimensions. However, elongations of different samples within the present investigations can be readily compared to each other.

Compression tests were conducted using the same testing stage (Fig 3.7) equipped with special clamps. The displacement was precisely measured using a laser extensometer P-50 by Fiedler Optoelectronics to read TiO_2 marks that had been applied on the specimens' surfaces as shown in Fig. 3.7b. At least three samples were used for each condition to obtain statistically valid results.

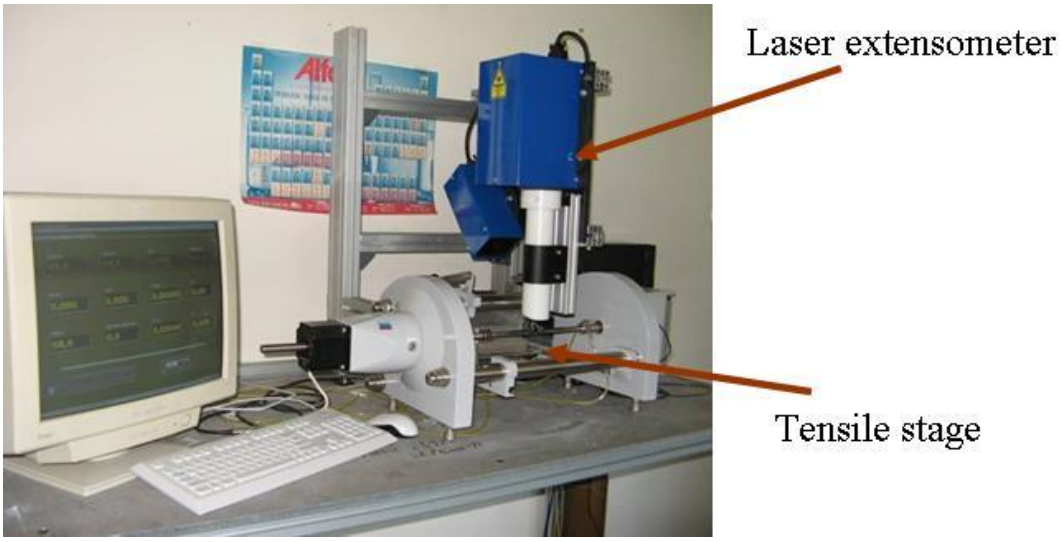


Figure 3.7 The tensile machine with laser extensometer.

Tensile specimens were cut out in the workshop of KIT CN. Fig. 3.8a shows a schematic representation of dog-bone shape specimens showing cutting position from disks processed by HPT. Thereafter specimens were mechanically fine polished using diamond suspensions with particle size down to 3 microns. The dimension of specimens for compression test was 1x1x1.5 mm^3 (Fig. 3.8b).

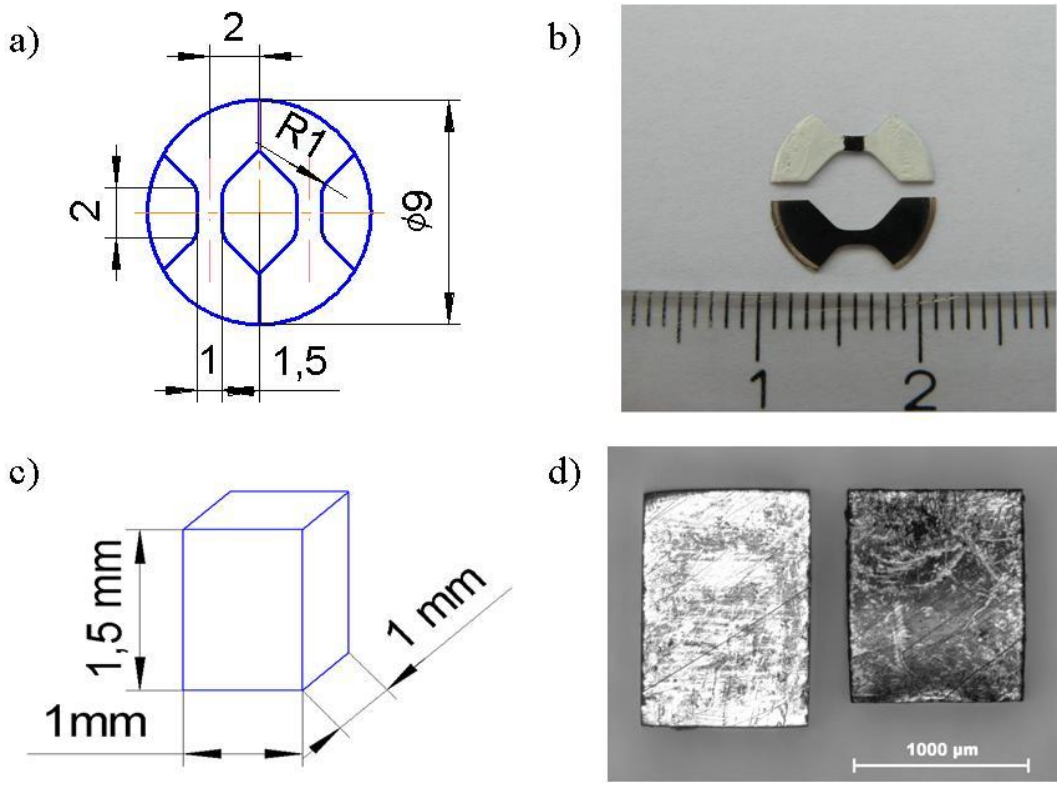


Figure 3.8 (a) A schematic representation of dog-bone shape specimens showing cutting position from disks processed by HPT. **(b)** View of the tensile specimens before test. **(c)** A schematic representation of compression specimen. **(d)** View of compression specimens before and after compression test.

3.4.4 Compression-torsion tests

For the compression-torsion test under a pressure of 4.5 GPa we used a Schenck™ testing machine (Fig. 3.9) with an axial load capacity of 400 kN (IMF-II, KIT CN, Karlsruhe). Due to instrumental limitations the angular range of rotation was restricted to $\pi/2$. Thus the deformation was proceeded in a cyclic form with a repeated back-and-forth rotation, inverting the rotation direction with identical magnitudes of the rotation rate. The axial load was maintained during the entire experiment. Complete tests were achieved with the following numbers, N, of cycles: N = 0.25, 0.5, 1, 2, 4 and 10, upon that one cycle is denoted as rotation for $\pi/2$ and back with total rotation angle of π. Rotation rate was a constant $\pi/2$ per 18 s, except for two runs at $\pi/2$ per 180 s and per 1800 s. All experiments were performed at room temperature.

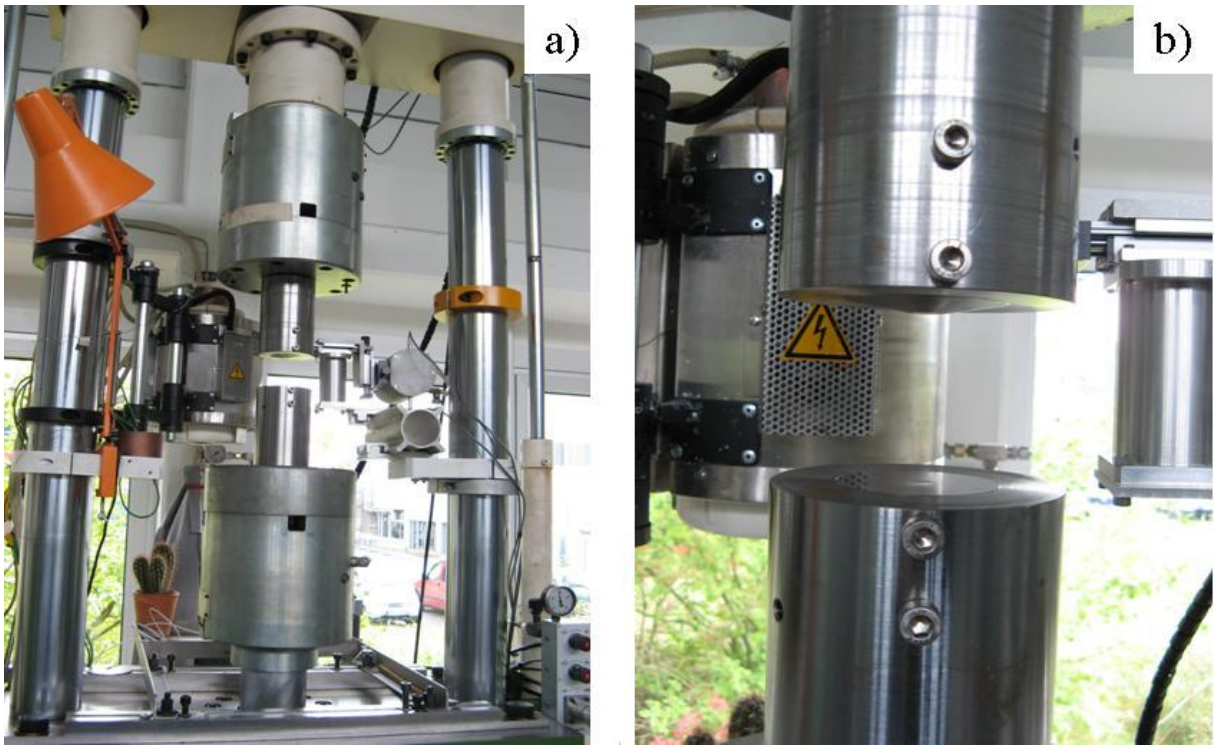


Figure 3.9 (a) Standard compression-torsion testing machine Schenck with capacity of 400 kN equipped with specially designed Bridgmen type anvils shown in **(b)**.

Chapter 4

Experimental results

4.1 Micro- and nanostructure formation resulting from severe shear deformation and related deformation mechanisms in nc and ufg Pd and Pd-Ag alloys

4.1.1 Microstructure of Pd-Ag alloys resulting from High Pressure Torsion

The investigation of the microstructure was done by means of TEM. Fig. 4.1 shows typical bright-field and dark-field images of as-HPT processed Pd and Pd-Ag alloys. The microstructure of all samples is characterized by slightly elongated grains with an aspect ratio of about 1.5. It is also shown that alloying leads to a decrease of the resulting grain size (Fig. 4.1e, 4.1f, 4.1g, 4.1h).

The mean grain size in as-HPT Pd is 240(15) nm as determined by TEM. Grains are delineated by narrow and distinct grain boundaries as shown in Fig. 4.2a. Separate dislocations and dislocation subboundaries are observed inside the grains (Fig. 4.2a). The microstructure of as-HPT alloys looks different as compared to that of pure Pd. The grain size becomes notably smaller, e.g. the mean grain size in the Pd-10%Ag and Pd-20% Ag is 206(11) nm and 150(15) nm, respectively (Fig. 4.1f, 4.1g), and dense dislocation tangles and pile ups are present in all grains (Fig. 4.2b, 4.2c). Additionally, in the Pd-20 %Ag very narrow nano-twins with a thickness of several nm can be found (Fig. 4.2d); the value of grains with such nano-twins is less than 5 %. The further increase of the Ag content leads to a further decrease of the resulting grain size to 144(15) nm in the Pd-40% Ag alloy (Fig. 4.1h). Upon that, the number of grains with nano-twins visually increases, and the dislocation density inside the grains is still high (Fig. 4.2e).

The statistical analysis of the grain size distributions determined from dark field TEM images is shown in Fig. 4.3. It is evident that the width of the grain size distribution is reduced with increasing Ag content, thereby demonstrating that the microstructure becomes more uniform.

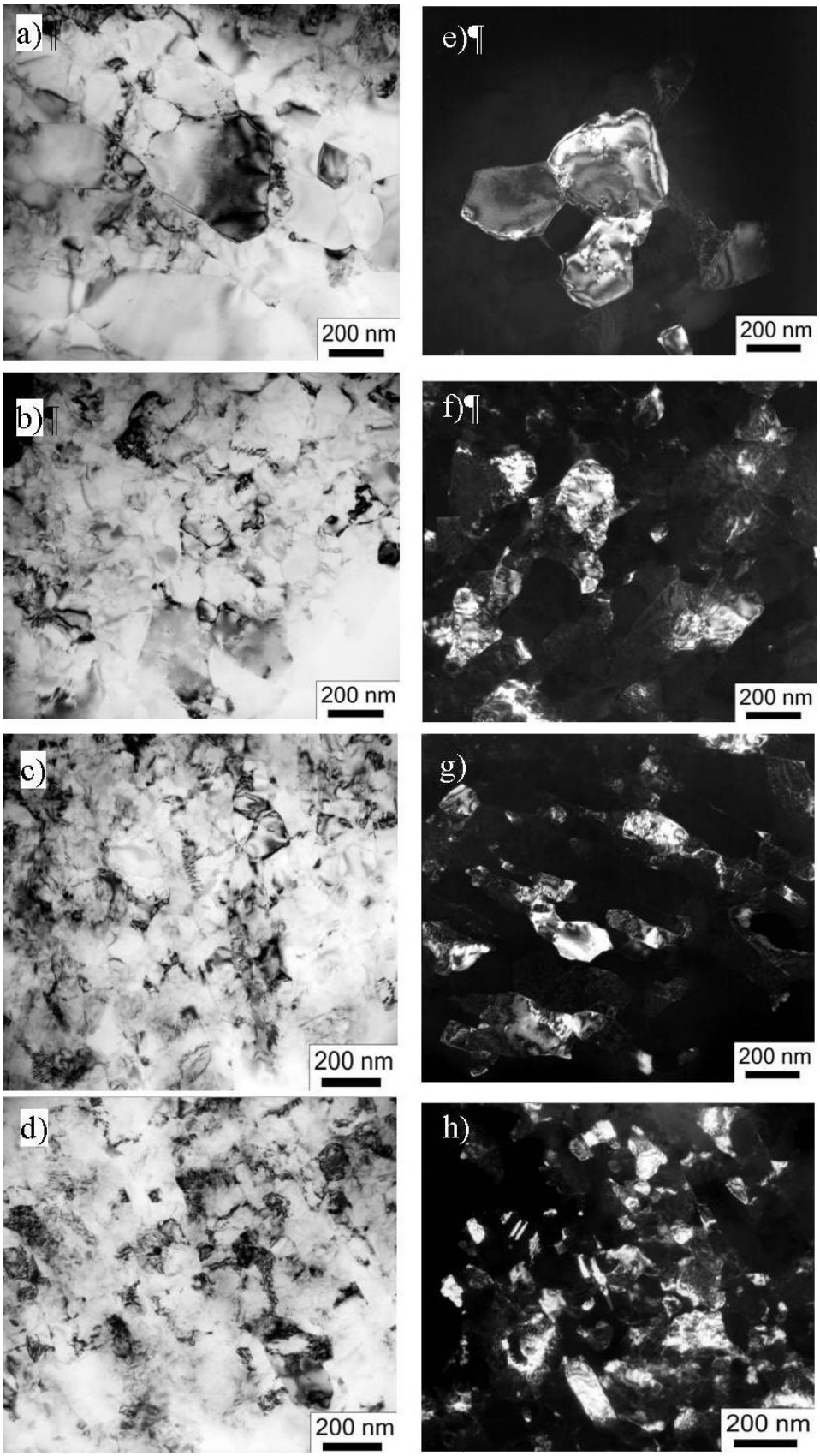


Figure 4.1 Typical microstructures of HPT-processed Pd (**a,e**), Pd-10%Ag (**b,f**), Pd-20%Ag (**c,f**), Pd-40%Ag (**d,h**). Bright-field (a,b,c,d) and dark-field (e,f,g,h) TEM images were done using a Phillips CM 30 operated at 300 kV.

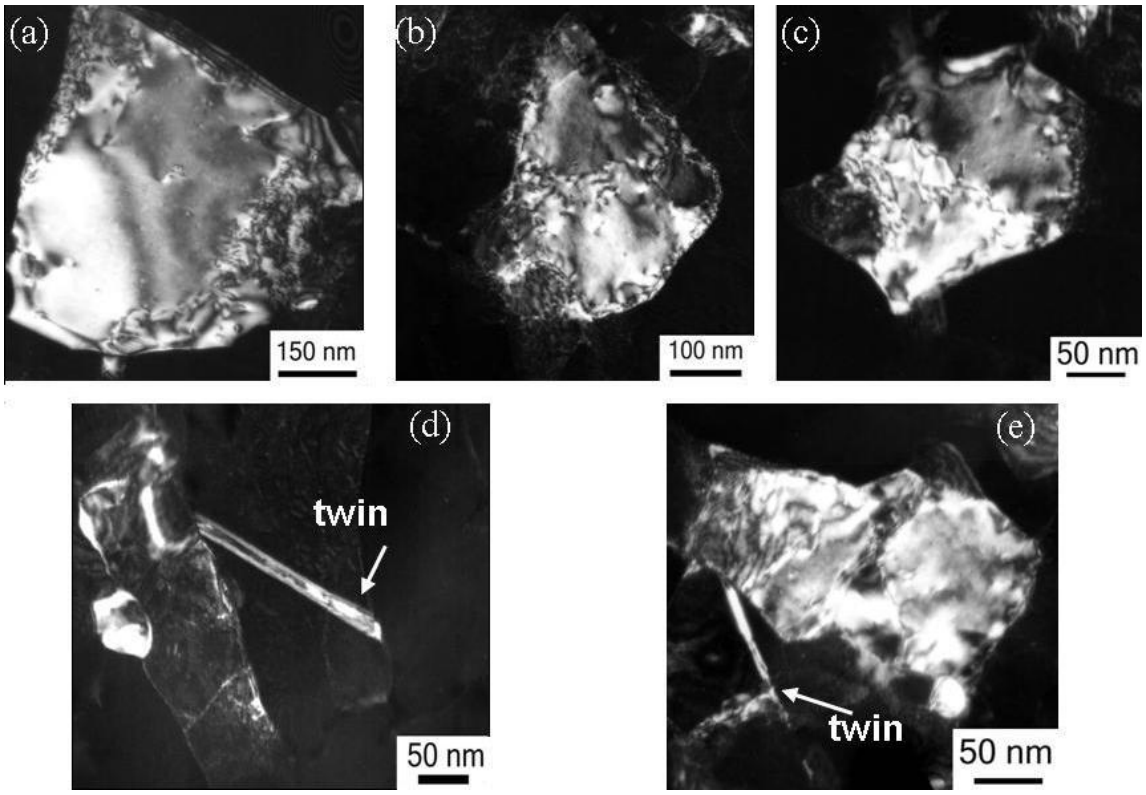


Figure 4.2 Dark-field TEM images showing defect structures in HPT-processed Pd **(a)**; Pd-10%Ag **(b)**; Pd-20%Ag **(c,d)** and Pd-40%Ag **(e)**. Images were done using a Phillips CM 30 operated at 300 kV.

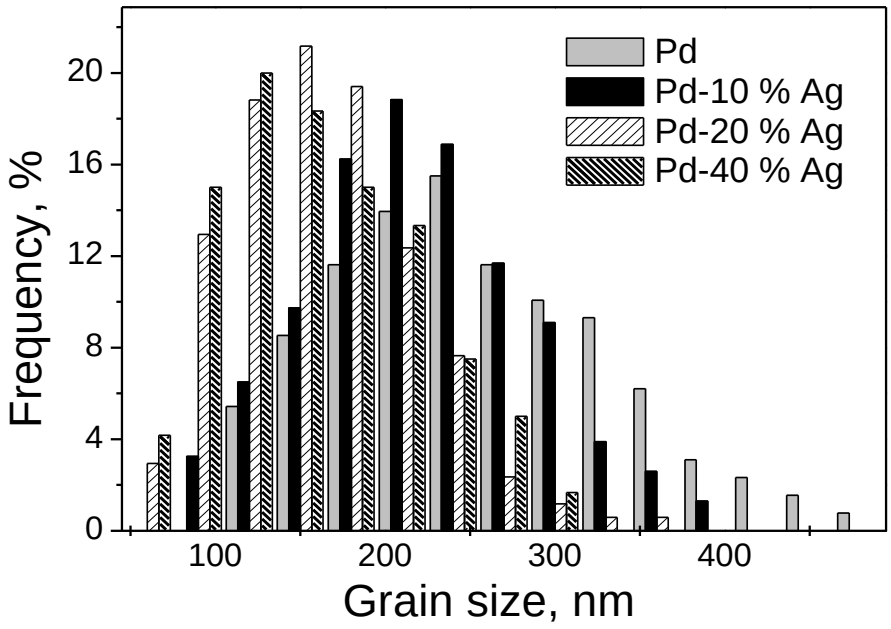


Figure 4.3 The grain size distribution in HPT-processed Pd, Pd-10%Ag, Pd-20%Ag and Pd-40%Ag.

Additionally, the following microstructure parameters like the volume averaged crystallite size, the average amount of microstrain, the lattice parameter, and the stacking fault probability were evaluated from the analysis of the XRD peak profiles obtained using synchrotron radiation, and the results are summarized in Table 4.1. Similar to the TEM observations, the XRD crystallite size is also decreasing with increasing Ag content. Besides, the XRD crystalline size is smaller than the grain size measured from TEM. The reason is that XRD measures the coherent diffraction domains which include dislocation cells and subgrains. Furthermore, with increasing Ag content both the microstrain and the stacking fault probability α_{SF} are increasing (Table 4.2).

As it was mentioned in the section 3.3, the estimation of lattice parameter and stacking fault probability was done using XRD measurements at the special angle Ψ=48° to overcome the influence of residual stresses. For example, the value of lattice parameter of pure Pd estimated using the measurements conducted at Ψ=0° and Ψ=48° were 389.124±0.045 pm and 389.041±0.008 pm, respectively. The residual stress leads to a notable overestimate of the lattice parameter, whereas lattice parameter measured using Ψ=48° is very close to that of as-cast material (389.056±0.012 pm). All the data in Table 4.1 were estimated from XRD measured at the special angle Ψ=48°.

Table 4.1 Microstructure parameters of HPT-processed Pd and Pd-Ag alloys: TEM grain size (d), XRD crystallite size (<D>), microstrain ($<\varepsilon^2>^{1/2}$), stacking fault probability (α_{SF}), dislocation density(ρ) and lattice parameter (a).

% Ag	d [nm]	<D>, [nm]	$<\varepsilon^2>^{1/2}$ [%]	α_{SF}, [%]	ρ, $\times 10^{15}$ [m^{-2}]	a, [pm]
0	240(15)	86.45(6.35)	0.06(0.01)	0.055	0.07	389.04(0.01)
10	206(11)	50.7(5.0)	0.26(0.01)	0.34	1.4	389.98(0.09)
20	150(15)	29.8(2.2)	0.37(0.01)	0.82	2.8	392.69(0.19)
40	144(14)	23.55(1.65)	0.30(0.02)	0.27	1.8	395.85(0.05)

HRTEM observations of stacking faults in Pd-20% Ag alloy

The high value of stacking fault probability (α_{SF}) for Pd-20% Ag (Table 4.1) indicates that the dislocations are very likely splitted. However, the splitting distance is not large enough to be distinguished from unsplit dislocations in conventional TEM images. Indeed, HRTEM observations in <110> orientation revealed numerous staking faults (SFs) (Fig. 4.4, inserts A,B) and staking faults tetrahedrons (Fig. 4.4, insert C). The stacking faults lay in the (111) crystallographic planes. We measured the widths of 50 SF ribbons from HRTEM images. They span a range from 3 to 5.5 nm with an average width of 4.4 nm. The SFs in Fig. 6A is shown edge on. A Burgers circuit [100] has been drawn showing a closing failure due to the presence of a Shockley partial dislocation as indicated. Very often, however, the lattice shift across the apparent SF line appears unclear (Fig. 4.4, insert B), but the stress field related with the SF straightforwardly reveals its presence. We should emphasize that a high local density of stacking faults was revealed in our HRTEM observations. Typically, 10-15 SFs can be seen simultaneously in a field of view (area 35×35 nm). On the other hand, areas free of any defects can also be observed in HRTEM.

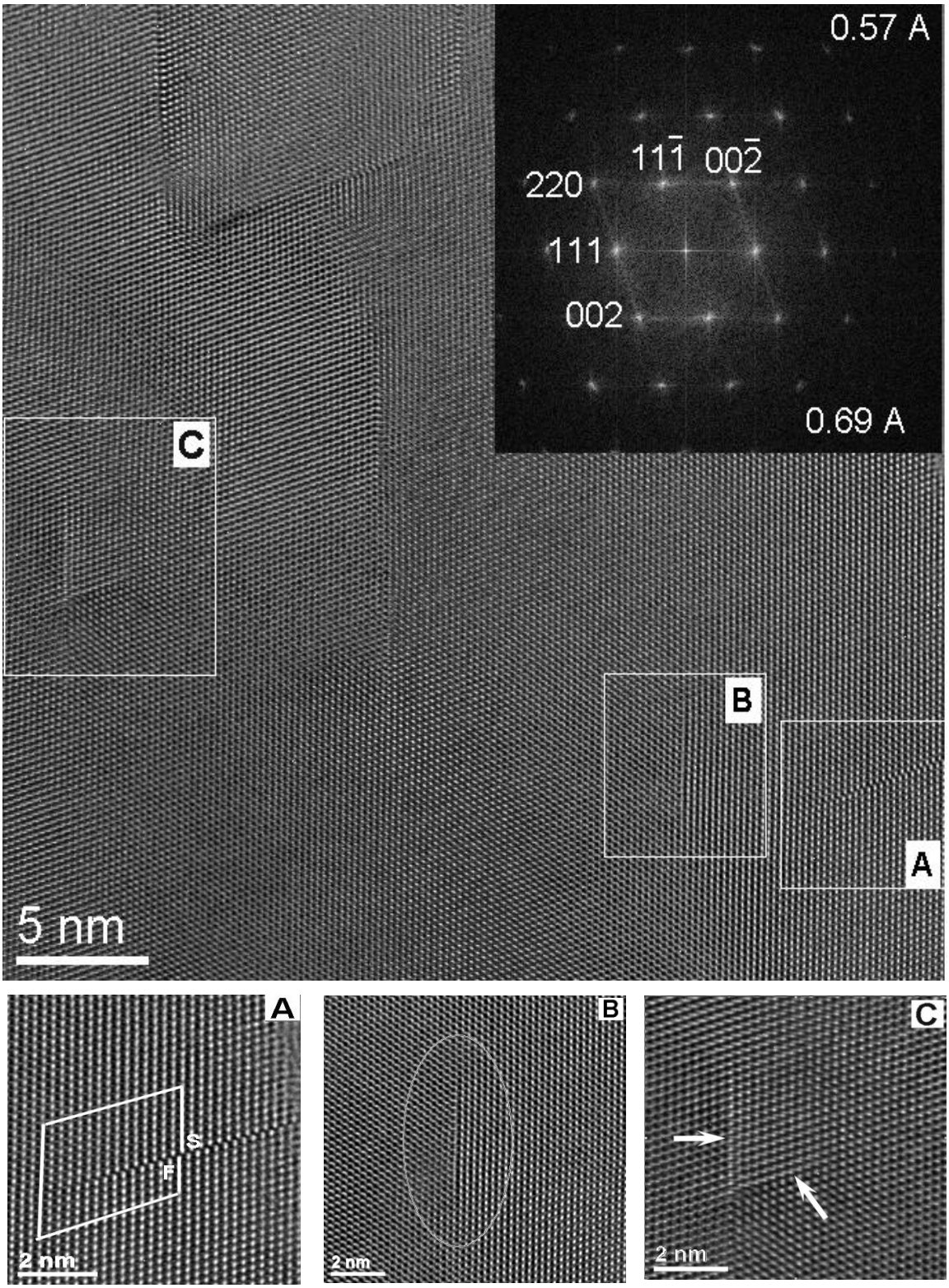


Figure 4.4 HRTEM image of stacking faults in HPT-processed Pd-20% Ag viewed along <110>, insert shows corresponding FFT. Several SFs are indicated with arrows, and two defects are shown enlarged in A and B: in **A** lattice shift in (11-1) is clearly seen as shown by a Burgers circuit; S refers to the starting point and F the finishing point of the Burgers circuit respectively; in **B** stacking fault is indicated by oval, lattice shift is not so clearly seen as in A. **C** shows stacking fault tetrahedron. (HRTEM by Dr. A. Chuvilin and Dr. C. Kübel on FEI Tecnai F20 G^{2e} operated at 200 kV).

4.1.2 Microstructural evolution by TEM analysis

A major impediment to studies of the deformation of nanocrystalline metals is their typically very limited ductility in tension, which restricts the experimentally accessible parameter space. Torsion testing under high pressure [101,102] offers an important opportunity, since it allows practically unlimited shear strain without fracture. In this section, we apply this technique to the nanocrystalline metal, prepared by inert gas condensation. This allows us to explore the microstructure development in a very wide range of strain and strain rate. Besides, presented results is the first investigation of the mechanical behaviour of nanocrystalline material with a grain size as small as ~14 nm, and strain as large as several hundred.

The microstructure investigations and microhardness measurements of investigated samples were conducted in sample areas situated at a distance of 3 mm from the sample centre, and this distance was used for estimation of the shear strain, γ. The local value of shear strain at a distance r from the sample centre is

$$\gamma = \pi N r / t \qquad (4.2),$$

where γ is the shear strain, t – thickness of the sample, N – number of revolutions.

We shall use the r = 3 mm shear strains as representative average values. The average shear strain, assuming uniform deformation, is given by

$$(\pi R^2)^{-1} \int_0^R 2\pi r \gamma(r)\, dr = 2\pi N R / (3 t). \qquad (4.3)$$

In other words, the mean strain in the sample strain would more precisely be obtained by evaluating γ at r = 2/3 R, or r = 2.7 mm. For this distance from the centre the shear strain rates, $\dot{\gamma}$, were 0.8 s^{-1} for rotation rates $\pi/2$ per 18, s.

Comprehensive microstructure investigation of as-IGC and consolidated specimens of pure Pd after cyclic HPT deformation has been performed using XRD analysis and conventional and high resolution TEM.

4.1.2.1 XRD analysis of nc Pd resulting from compression-torsion tests

The X-ray data for samples deformed at the strain rate of 0.8 s^{-1} in the shear strain range (γ) up to 30 indicate an increase of the crystallite size and concomitant decrease of the microstrain (Fig. 4.5 and Table 4.2). Further cyclic deformation is seen to reverse both

trends. Note specifically the remarkable finding of decreasing microstrain with increasing plastic deformation.

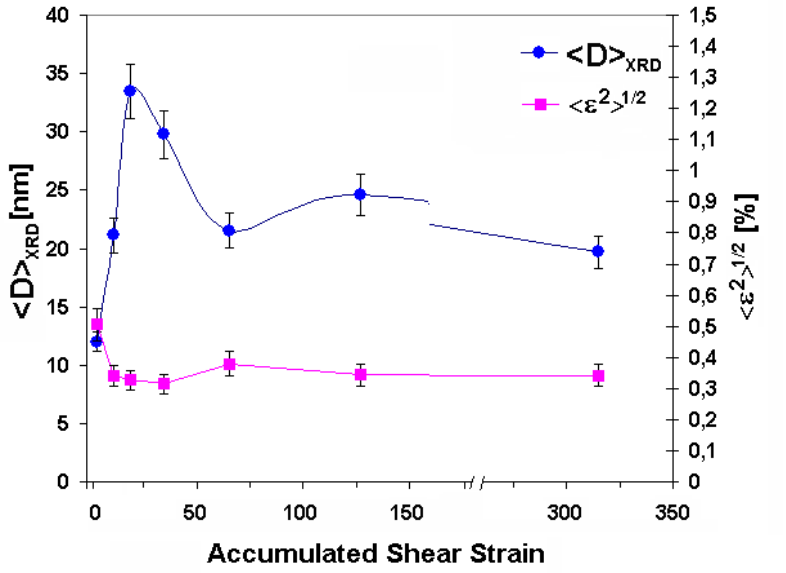


Figure 4.5 Variation of XRD grain size $\langle D \rangle_{XRD}$ and microstrain with increasing of accumulated shear strain in nc Pd HPT-deformed at shear strain rate $\dot{\gamma} = 0.8\ s^{-1}$.

Table 4.2 Relative density, TEM and XRD grain size (*d* and $\langle D \rangle_{XRD}$, mean square root microstrain ($\langle \varepsilon^2 \rangle^{1/2}$) with error bar ($\delta\langle \varepsilon^2 \rangle^{1/2}$) and microhardness (HV) of nc Pd in as-IGC state and after cyclic HPT at 4.5 GPa and shear strain rate $\dot{\gamma}$ of 0.8 s^{-1}.

Nr. of cycles	Shear strain	Relative density [%]	d [nm]	$\langle D \rangle_{XRD}$ [nm]	$\delta\langle D \rangle_{XRD}$ [nm]	$\langle \varepsilon^2 \rangle^{1/2}$ [%]	$\delta\langle \varepsilon^2 \rangle^{1/2}$ [%]	HV
as-IGC	0	91	14.3(0.8)	14.0	0.75	0.50	0.03	280
0.25	7.8	97.6	40(4)	21.1	0.8	0.34	0.01	382
0.5	15.7	97.9	-	33.5	3.3	0.33	0.01	394
1	31.4	97.4	-	29.8	1.2	0.315	0.013	392
2	62	97	-	21.55	0.6	0.38	0.01	380
4	124	96.1	66(6)*	24.6	2.4	0.34	0.02	388
10	310	-	150*	19.7	1.5	0.34	0.02	385

* grain size is measured normal to shear direction

The diffraction data also reveals a clear trend for the stacking fault parameter, α_{SF}, to increase with strain, starting out from a small value in the as-prepared samples. Its value at

γ = 15 increases systematically when the strain rate is decreased, with values of 1 in sample deformed at strain rates of 0.8 s^{-1}.

4.1.2.2 Microstructure evolution (TEM)

As it was shown in section 3.1 the initial as-IGC microstructure is very homogeneous (Fig. 3.2a) with a comparatively narrow grain size distribution (Fig. 4.6a). The mean grain size – as estimated from separate histograms of several TEM micrographs – is 14 (1) nm. This agrees well with the crystallite size estimated in the XRD analysis above, 14 (1) nm (Fig. 4.5, Table 4.2).

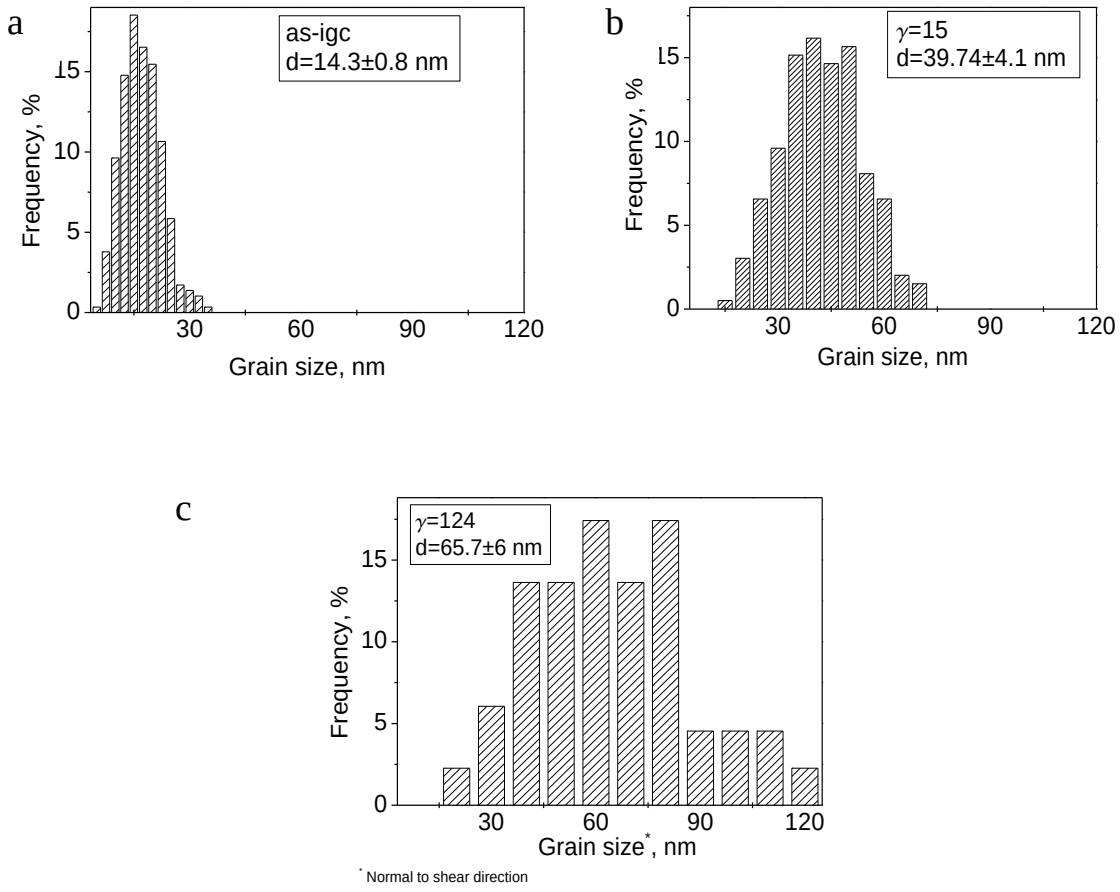


Figure 4.6 An evolution of grain size distribution of nc Pd in as-IGC state **(a)** and after cyclic HPT at 4.5 GPa and shear strain $\dot{\gamma}$ = 0.8 s^{-1}: **(b)** after γ=15 and **(c)** after γ=124. Note that the grain size after γ=124 was measured normal to shear direction.

Shear strain $\gamma \leq 15$

The TEM micrographs of Fig. 4.7a,b reveal a larger grain size at the strain value $\gamma = 15$. In fact, the histograms of Fig. 4.6b indicate that d = 40 (4) nm, more than twice the initial value. It is also seen that the size distribution has broadened. At an aspect ratio of 1.1, the grains appear still equiaxed at this strain.

Dislocations and their pile-ups - spreading throughout entire grains – can be found in larger grains with diameter >50 nm (Fig. 4.8a). Importantly, however the fraction of grains with dislocations is rather low, in other words, the overall dislocation density is small in the sense that most grains are visibly free of dislocations. At γ = 15, some amount of twins in the form of thin lamellae are also observed inside of many grains, their amount is visibly larger than that in the as-IGC state. Fig. 4.8b shows a HRTEM image of a typical twin boundary in a sample deformed to γ = 15 at a strain rate of 0.8 10^{-1} s^{-1}.

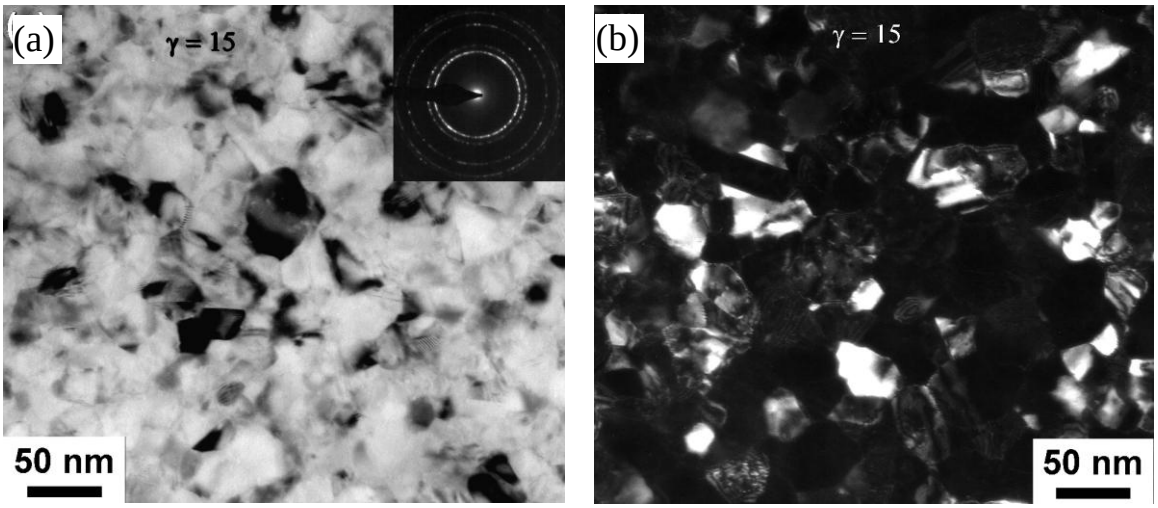


Figure 4.7 Microstructure of nc Pd after cyclic HPT at 4.5 GPa and shear strain rate of 0.8 s^{-1} after γ =15. **(a)**: bright field images and selected area diffraction patterns as inserts; **(b)** dark field images. Dark-field and bright-field images were done on a Phillips CM 30 operated at 300 kV.

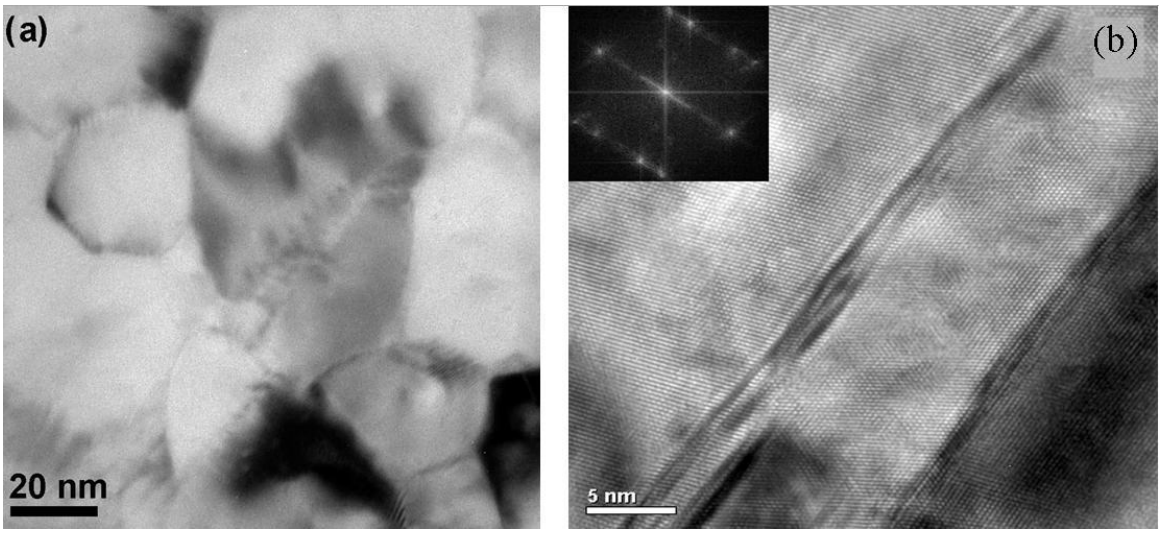


Figure 4.8 Typical images of defect structures in nc Pd after HPT: **(a)** dislocation pile-ups spreading from one GB to the opposite one (grains in centre and in the left bottom corner). Note that other grains do not contain any dislocations. Bright-field image was done on Phillips CM 30 operated at 300 kV. **(b)** HRTEM image of a twin boundary, insert shows corresponding fast Fourier transform. (HRTEM image was done by Dr. H. Rösner on FEI Tecnai F20 G^{2e} operated at 200 kV).

As the most remarkable microstructural feature we advertise structures such as those shown in Fig. 4.9 In part (a) and (b) of the figure, several neighbouring segments of grain boundaries are seen to align in parallel. Part (c) shows another peculiar feature, where individual grains have apparently suffered a large shear along a single slip plane. These features were typically observed quite frequently in samples deformed to $\gamma = 15$ at all studied strain rates, and were clearly absent in as-IGC state.

Shear strains $\gamma > 15$

Micrographs taken at $\gamma \approx 124$ (Fig. 4.10a,b) show a more pronounced grain growth, with grain shapes now distinctly anisotropic. The mean grain dimension measured normal to the shear direction has increased fourfold, to 66(6) nm, as can be seen from the transverse grain dimension distribution, Fig. 4.6c. On the other hand, the grain dimension measured along the shear direction had increased much more, exhibiting a very broad distribution without distinct maximum (not shown here). We were not able to observe any twins in specimens deformed to that strain, but the dislocation density was very high.

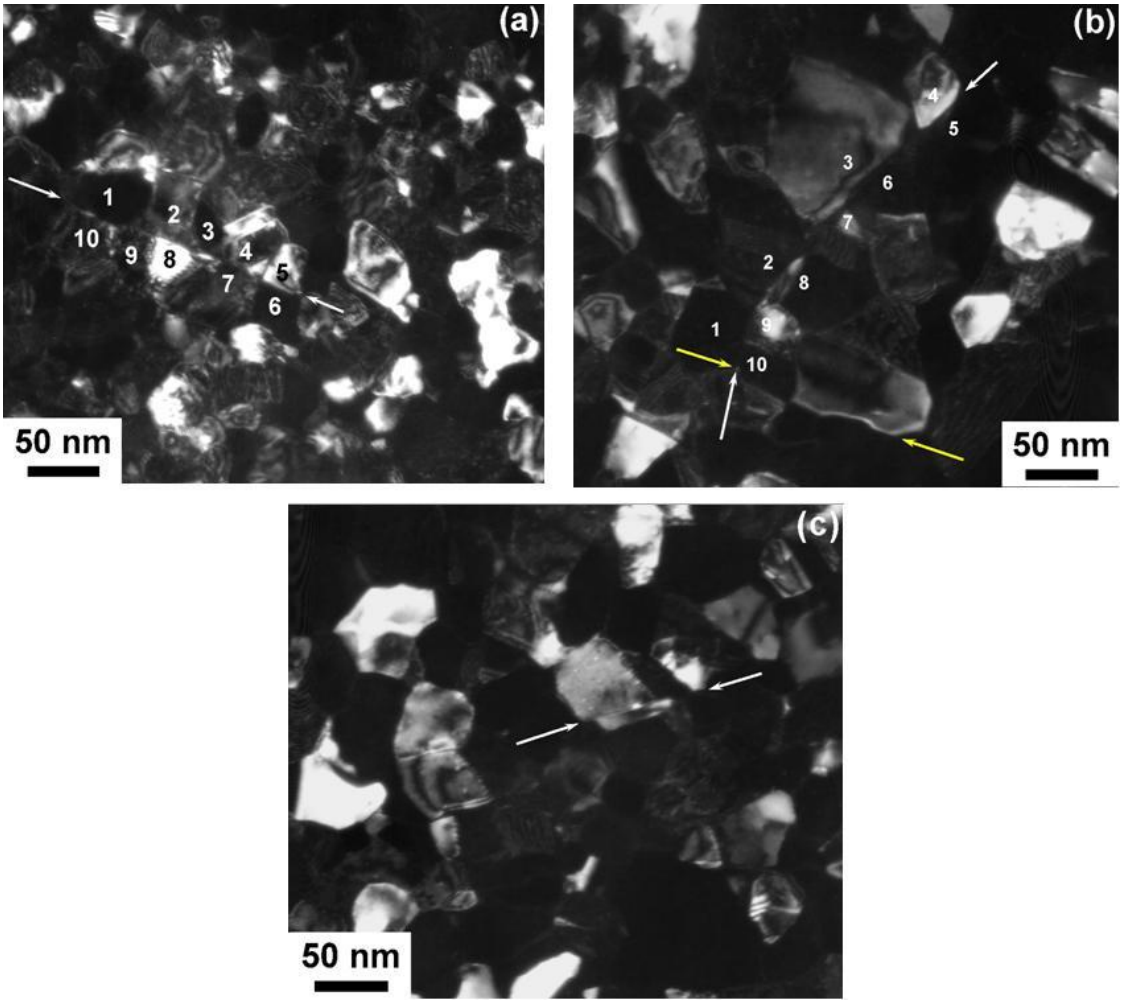


Figure 4.9. Dark field images using the 111 reflections of nc Pd microstructure after HPT for γ=15 at $\dot{\gamma} = 0.8\ 10^{-2}\ s^{-1}$: **(a)** alignment of boundaries of 10 grains with formation of a mesoscopic shear plane, note that grain 4 contains two twins; **(b)** another example of a mesoscopic shear plane, banding of a primary plane (white arrows) is most probably related with formation of a secondary msp (yellow arrows). **(c)** Shear band passed across the grain cutting it into two segments. Dark-field images were done on a Phillips CM 30 operated at 300 kV.

Finally after γ = 300, the microstructure is coarsened further (Fig. 4.11a), it consists of elongated grains with 150 nm in transverse cross section, and very high dislocation density. However, several areas (Fig. 4.11b) with slightly elongated grains were also observed.

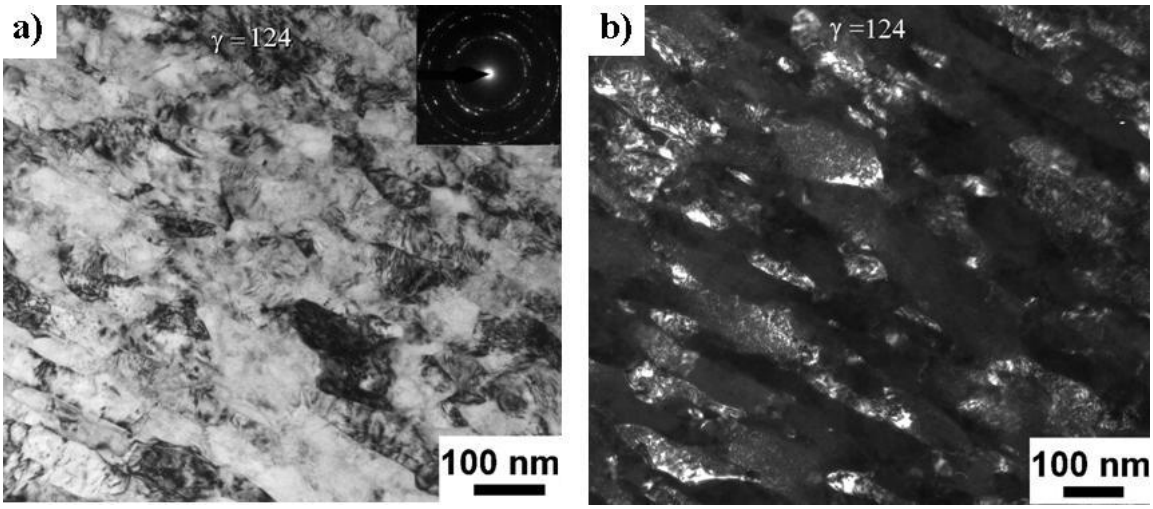


Figure 4.10. Microstructure of nc Pd after cyclic HPT at 4.5 GPa and shear strain rate of 0.8 s^{-1} after $\gamma = 124$. **(a)** Bright field images and selected area diffraction patterns as inserts; **(b)** dark field images. Dark-field and bright-field images were done on a Phillips CM 30 operated at 300 kV.

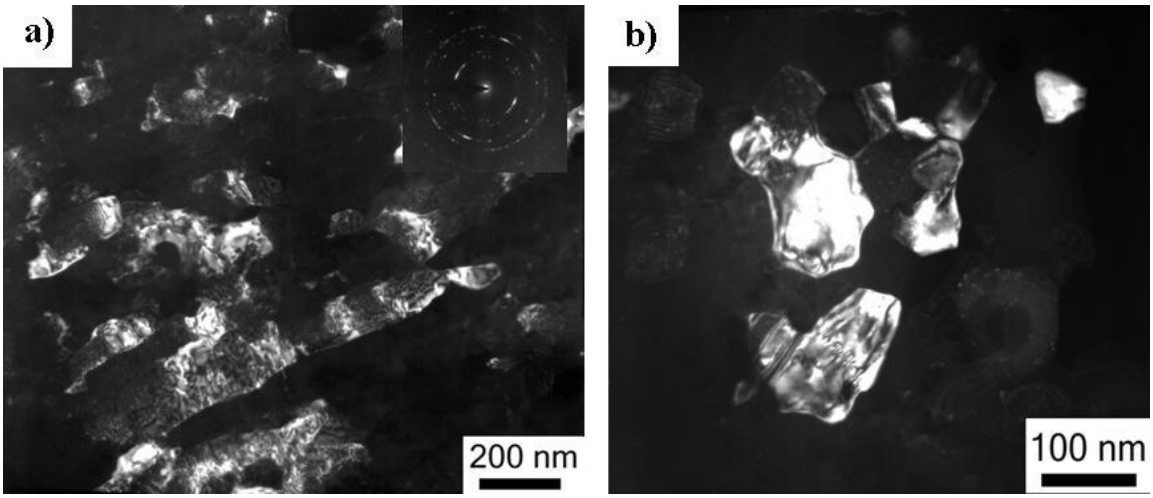


Figure 4.11. Microstructure of nc Pd after cyclic HPT at 4.5 GPa and shear strain rate of 0.8 s^{-1} after $\gamma = 300$. **(a)** Dark field image and selected diffraction patterns as insert. **(b)** Dark-field image showed formation of new equiaxed grains. All images were done on a Phillips CM 30 operated at 300 kV.

4.2 Mechanical performance of nc and ufg Pd and Pd alloys

4.2.1 Results of tensile tests of Pd-Ag alloys

In the section 4.1.1, it was shown, that the alloying influences on the microstructure of Pd-*x* at.% Ag alloys (*x* = 10,20,40). Therefore, it is expected, that changed microstructure should influence the mechanical behaviour of tested material. In the present section the deformation behaviour of ufg Pd-Ag deformed in tension is described.

Fig. 4.12a shows the typical tensile curves of the ufg Pd, Pd-10%Ag, Pd-20%Ag, and Pd-40%Ag alloys. It is apparent that the strength of materials is increasing with increasing Ag content. Remarkably, the Pd-20%Ag and the Pd-40%Ag alloys did not only show the highest values of yield and ultimate strength, but also the largest uniform strain (Table 4.3).

Table 4.3. List of mechanical properties: yield stress (YS), ultimate stress(UTS), uniform elongation(ε_u) and elongation to failure(ε_f) of HPT samples.

% Ag	YS [MPa]	UTS[MPa]	ε_u[%]	ε_f[%]
0	628	760	3.5	16
10	870	1153	5	16
20	975	1215	5.5	13.5
40	1000	1130	5.5	15

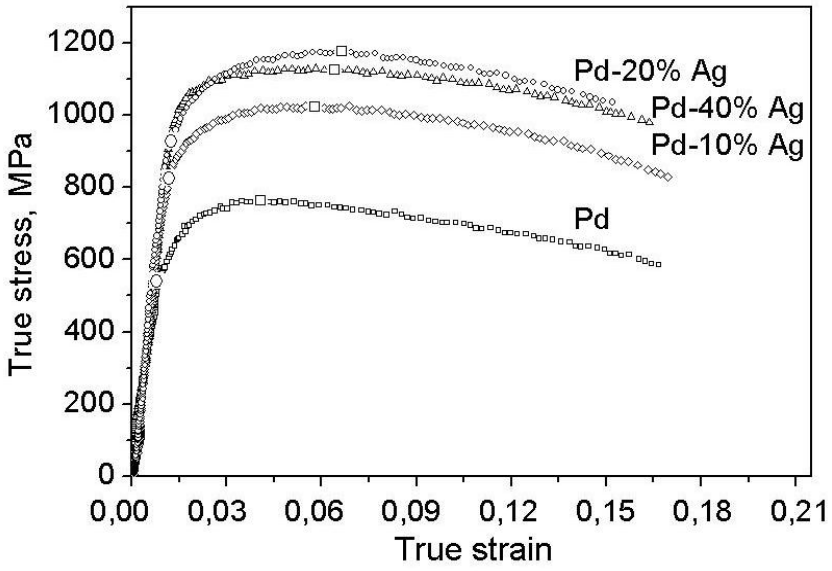


Figure 4.12 Tensile stress-strain curves of UFG Pd, Pd-10%Ag, Pd-20%Ag Pd-40%Ag. The circles indicate the onset of yielding and the squares point to the ultimate stress. Strain was measured by means of the laser extensometer.

4.2.2 Mechanical properties of nanocrystalline Pd and Pd-10 at.% Au

In the present section, we present results on the mechanical behaviour of nc Pd and Pd-10 at.% Au prepared by method of IGC. Initial microstructure (Fig. 3.2b) was described in section 3.1.

All samples deformed in tensile mode showed brittle behaviour and fractured prematurely in the elastic regime (Fig. 4.13). Such a brittle behaviour of the material could be linked to the method of preparation of studied samples. It was already discussed (section 2.1.1) that one of the disadvantages of the IGC technique is residual porosity. As a check on it the tensile tests of the material with same density but large grain size were performed. In Fig. 4.13, true stress- true strain curve of cg Pd is presented. Samples fractured at the strain 0.05. On the bright-field images of cg Pd TEM investigations pores are observed inside of the grains (Fig. 4.14).

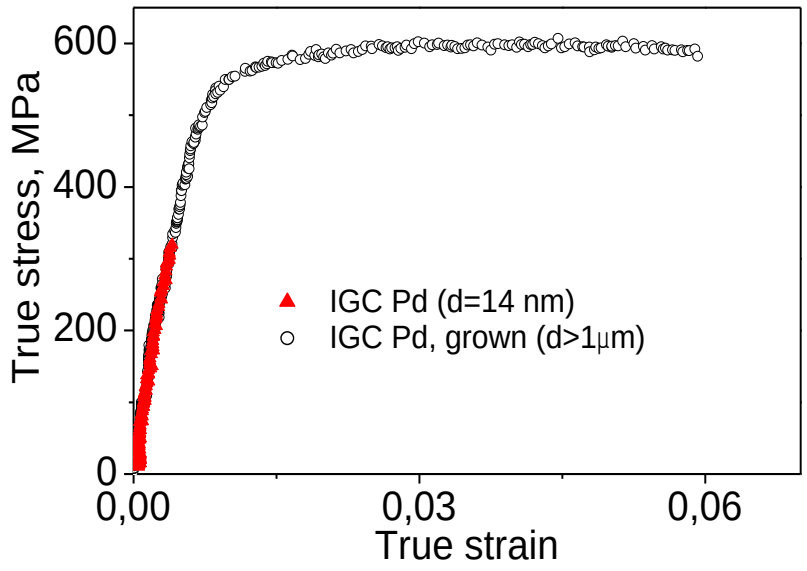


Figure 4.13 Tensile true stress- true strain curves of nc and cg Pd.

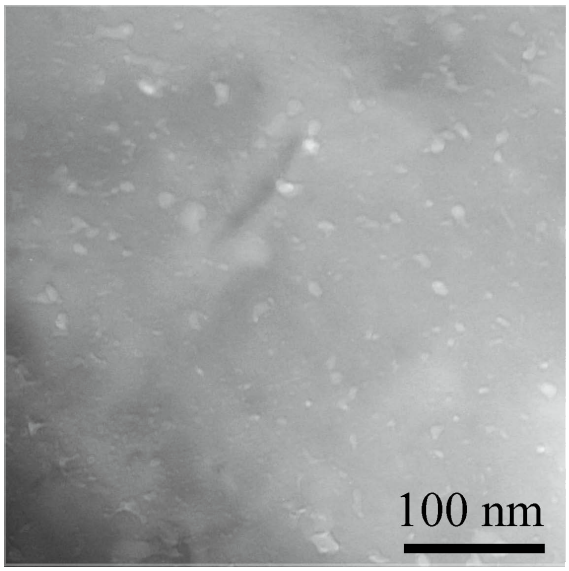


Figure 4.14 Bright-field image of cg Pd was done on a Phillips CM 30 operated at 300 kV.

Typical engineering compression stress – strain curves of nc Pd and Pd-Au are shown in Fig. 4.15. Remarkably, the samples exhibit high strength and significant ductility in the compression tests. Our measure for the yield strength is the stress, σ_{02}, at plastic strain of 0.2%. The values of yield stress (YS) (standard deviation in brackets) for nc Pd and Pd-10at.% Au were 810(80) and 900(50), while the ultimate strengths (UTS) were 60 to 80% higher, 1470(100) and 1470(150), respectively. The compression strains to failure were 0.15(0.01) for Pd and 0.15(0.012) for Pd-Au. As expected, decreasing of grain size led to significant increase of σ_{02} as compared with the yield strength of coarse grained Pd (100 MPa) [103]. However, strain localization in the form of buckling was observed (Fig. 4.16a). The difference between YS values of pure metal and of the alloy is small, and the relative difference between the respective flow stresses, σ_F, never exceeds 10%. The difference tends to vanish at larger strain (Fig. 4.15).

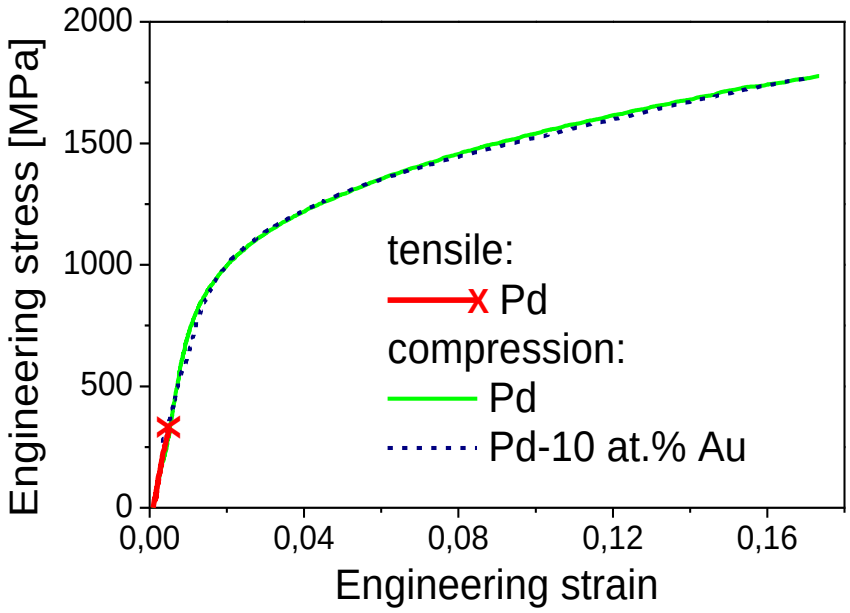


Figure 4.15 Engineering stress - engineering strain curves of Pd and Pd-10at.% Au.

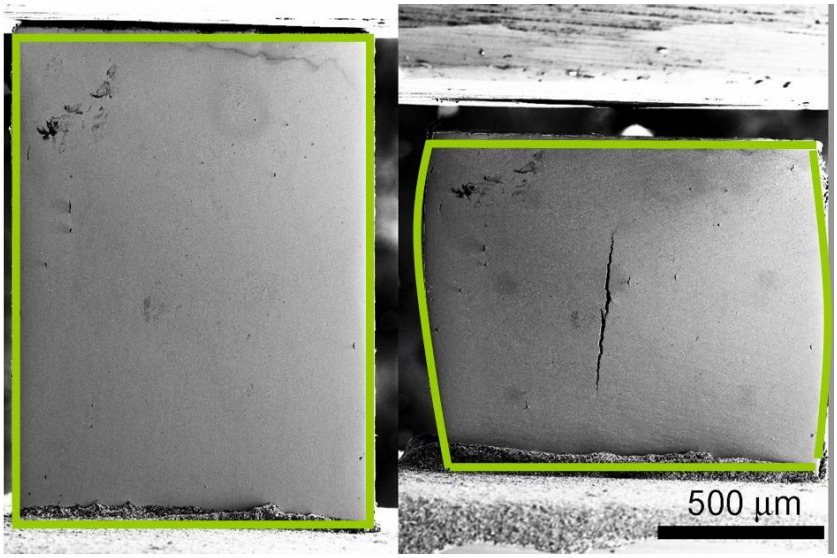


Figure 4.16 View of the sample before and after compression test. Samples after compression test show side-slip buckling, as emphasized by schematic outlines. [SEM images of samples view from K. Yang, Uni Ulm].

Additionally, we performed a room-temperature strain rate change test (jump test) to estimate strain rate sensitivity m, varying the strain rate between 5×10^{-4} s^{-1} and 1×10^{-4} s^{-1}. Typical results are presented in Fig. 4.17. The strain rate sensitivity, *m*, was estimated using Eq. 3.6, which yields *m*=0.050(5) and 0.040(5) for nc Pd and Pd-Au, respectively. These values are consistent with previous reports for the strain rate sensitivity of

electrodeposited Ni with grain size 30 nm [64,65,104,105], and they are much lower than at superplastic flow ($m \geq 0.3$).

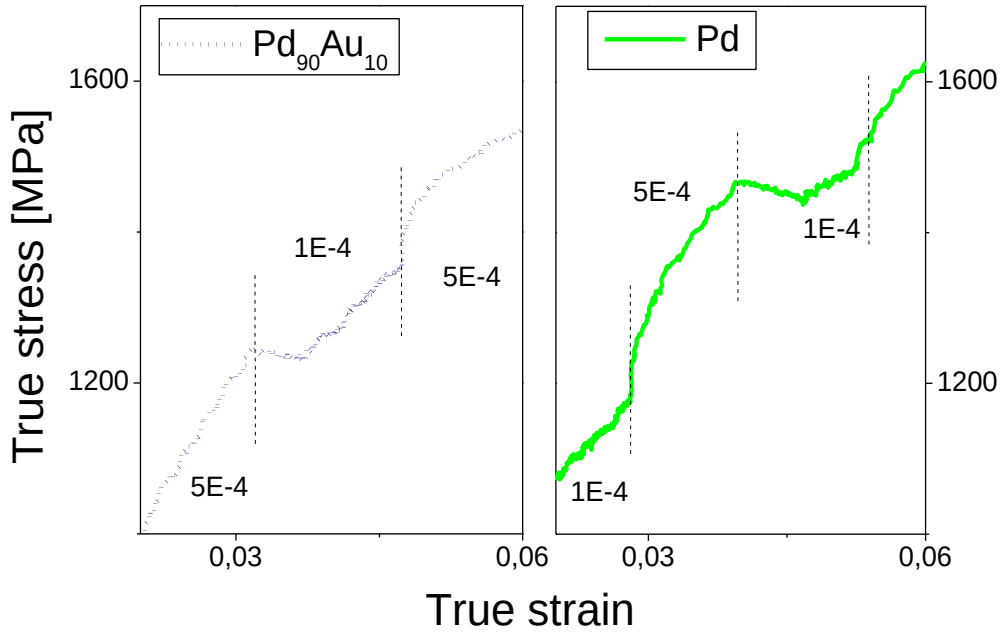


Figure 4.17 Stress-strain curves during strain rate jump tests of as-IGC Pd and Pd-10at.% Au. Labels denote strain rate in units of s^{-1}.

4.2.3 Mechanical properties of Pd with bimodal microstructure

Bimodal distribution of grain size is one effective method of improving ductility (section 2.2.3). In the present chapter we proofed if this idea would work with ns Pd.

To obtain larger grain size due to room temperature grain growth (see section 3.2) samples of as-IGC Pd were kept for 24 hours at the room temperature. Continuous HPT deformation for 5 revolutions was performed at Ufa State Aviation Technical University (Russia). Deformed microstructure is represented by areas with nanocrystalline grains with a mean diameter of 55(5) nm (Fig. 4.18a) and areas with ultrafine grains with a mean diameter of 110(10) nm (Fig. 4.18b). In the areas with the smaller grains deformation twins were observed, in contrast to the larger grains, where dislocation tangles were found. Furthermore the grain size distribution confirms bi-modal type of microstructure.

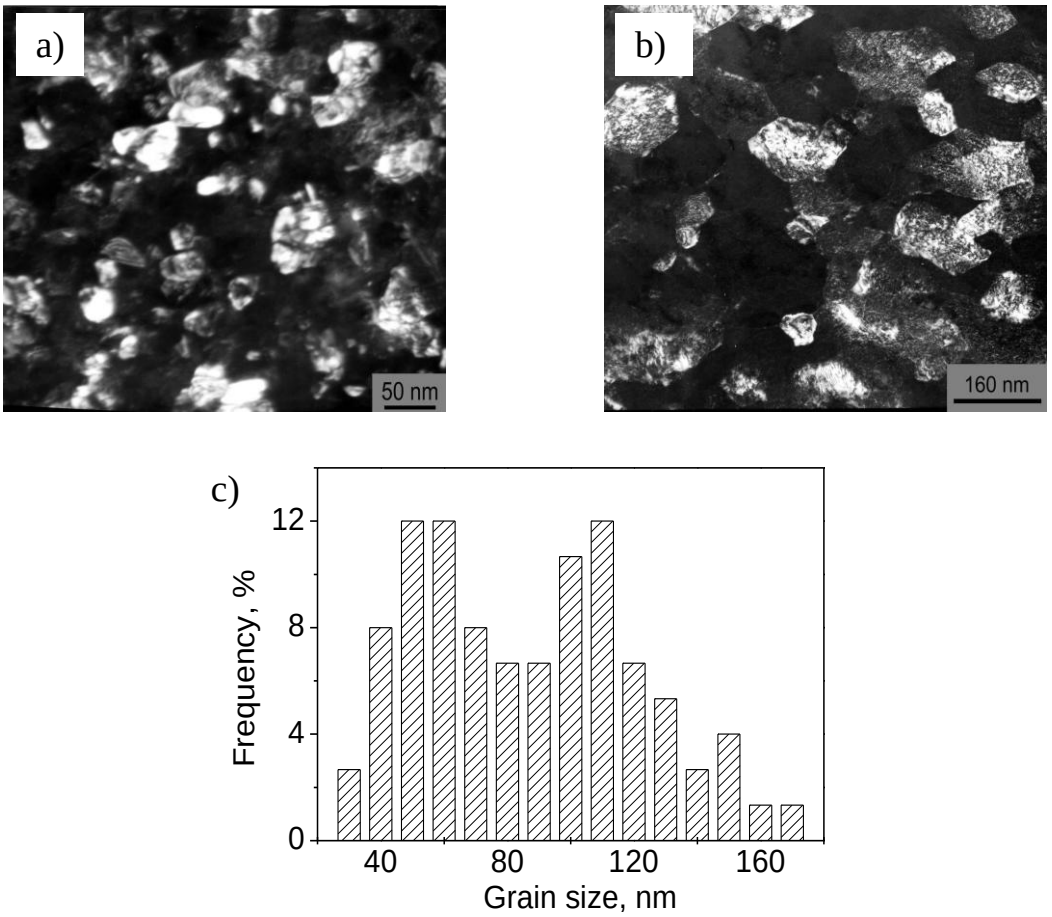


Figure 4.18 Bimodal microstructure of Pd after IGC and deformed by HPT with the strain 300. **(a)** Area with the grain size of 55 nm **(b)** Area with the grain size of 110 nm **(c)** Grain size distribution.

As mentioned in the previous section, tensile tests of IGC samples showed premature fracture in elastic range (Fig. 4.13). Tensile tests of ns Pd with bimodal microstructure revealed high value stress in combination with reasonable ductility (Fig. 4.19). Tensile tests were performed at two different strain rates, 10^{-3} and 10^{-2} s^{-1}. The ductility of samples was not good enough in order to perform strain rate jump tests for determination of the strain rate sensitivity. Therefore, an estimation of the strain-rate sensitivity was done by using the stress-strain curve obtained at different strain rates. By applying Eq. 3.6 we approximately calculated the following value: m = 0.1.

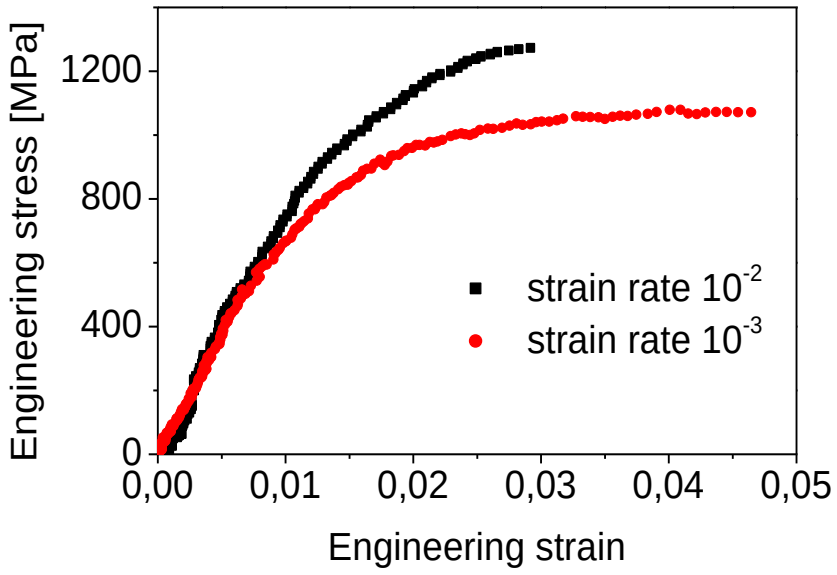


Figure 4.19 Tensile stress-strain curves of IGC+HPT Pd with bimodal structure conducted at different strain rates.

Chapter 5

Discussion

5.1 Fundamental plastic deformation mechanisms in nc and ufg Pd and Pd alloys

Different factors can influence the microstructure resulting after SPD, first of all initial microstructure, as well as chemical composition and conditions of the deformation. Furthermore, these factors affect the minimum grain size that can be reached in materials by SPD. As it was shown in section 4.1.1, the alloying with Ag significantly influences the grain size resulting from HPT: the larger the Ag content, the smaller the grain size.

It is well accepted that the microstructural evolution during HPT occurs as a sequence of several steps (or stages) and begins with the formation of a cell structure with high dislocation density present in the cell boundaries. When the HPT straining is continued over a wide range of strains a non-homogeneous microstructure is formed with a broad grain size and grain orientation distribution. However, the mean grain/cell size gradually decreases with increasing strain and the permanent storage of dislocations in cell boundaries leads to an increase of their misorientations. Finally, a steady stage is reached where the mean grain size achieves the lowest value, and neither the mean grain size nor the grain boundary misorientation distribution can be influenced by further deformation [9,106]. The occurrence of a steady state grain size is also typical for ball milling [107], but the grain size achieved at ball milling is usually lower than that after high pressure torsion. The physical reason for establishing the steady stage is not quite clear yet; it was proposed that the lowest grain size results from the balance between the produced dislocations and their recovery by thermal processes [101]. Obviously, the number of produced dislocations depends on the accumulated strain and should be similar in different materials which experienced the same strain. Then the rate of dynamic recovery is the crucial parameter for the steady stage grain size. This model helps to understand the role of alloying in the process of grain refinement at HPT of Pd-Ag alloys. First of all, pinning of dislocations by solute atoms restricts their free path leading to the smaller cell size. Furthermore, the stacking fault energy decreases rapidly with increasing Ag content (Table 4.1). As our HRTEM investigation has shown (Fig. 4.2.5), smaller values of SFE in the Pd-20% Ag alloy lead to the dissociation of dislocations, which hinders cross slip and climbing, and consequently, the ability of the material for a deformation recovery, which in

its turn leads to an enhanced dislocation storage. Dislocation tangles may rearrange to new cell boundaries and movable dislocations readily sink to cell boundaries promoting their transformation to high angle boundaries [9]. The importance of SFE for the final grain size achieved after severe plastic deformation was shown for ball milling [108] and high pressure torsion [109,110,111]. In all cases, the smaller the γ_{SF}, the smaller the resulting grain size.

According to Mohammed [108], other factors may influence the final grain size during SPD. In particular, the higher the initial hardness, the shear modulus, and the melting temperature, the smaller will be the resulting grain size. In spite of all these parameters (except hardness) decreasing in Pd-Ag alloys with increasing Ag concentration (Table 4.1), the resulting grain size has been decreasing, indicating that the stacking fault energy is a much more important parameter for grain refinement during SPD.

5.1.1 Deformation mechanisms in ultra-fine grained Pd-Ag alloys

Our TEM investigations (Fig. 4.2) demonstrated a notable increase of the dislocation density in the Pd-Ag alloys with the increasing Ag content, despite the decreasing grain size. Analysis of the XRD peak profiles also revealed a concomitant increase of the microstrain (Table 4.1). Microstrain is related to the dislocation density by [112,113]:

$$\rho_{strain} = \frac{k\left\langle \varepsilon^2 \right\rangle}{Fb^2} \qquad (5.1),$$

where ρ_{strain} is the dislocation density due to the microstrain and b the absolute of the Burgers vector, k depends on the kind of dislocations and the strain distribution due to their stress field and F describes their interaction. Quite elaborated methods exist in literature to determine the influence of the kind of dislocations on the strain broadening, especially the use of so-called contrast factors which describe the crystallographic anisotropy of the strain broadening and which do even allow for a distinction of the character of the dislocations (i.e., edge or screw) [114]. However, in the case of present study, Eq. 4.1 should be sufficient because we just want to investigate the change of dislocation density as a function of the silver content. We took $F = 1$, i.e. we assume non-interacting dislocations in the grain interior while all interacting dislocations build up the cell boundaries and their influence on the X-ray peak broadening is considered as size broadening and therefore distinguishable by the size-strain separation of the Williamson-Hall analysis. A value of

$k = 16$ as calculated by Williamson and Smallman describing the strain field of a screw dislocation in an fcc material [112] was used for the calculation of the dislocation densities.

In Table 4.1, the value of the dislocation density calculated using Eq. 4.1 for all studied alloys is presented. The dislocation density ρ increases almost linearly for 40 times from 0.07×10^{15} m^{-2} in pure as-HPT Pd to 2.8×10^{15} m^{-2} in the Pd-20% Ag alloy. Similar values were reported for HPT-processed Cu-Zn alloys, with the same trend for increasing ρ with decreasing stacking fault energy of the alloy [111].

As discussed above, the enhanced dislocation storage in alloys with higher Ag content is related to their lower SFE. The lower stacking fault energy promotes the splitting of dislocations, and indeed in HRTEM images of the Pd-20% Ag alloy, we observed numerous SFs (Fig. 4.4). These observations are consistent with the high stacking fault probability of 0.82% in this alloy (Table 4.1) as estimated by XRD.

Another indication of the high activity of dissociated dislocations during severe plastic deformation is the observation of the SF tetrahedrons formation in the Pd-20% Ag alloy (Fig. 4.4, inset C). Such defects can be frequently found in metals and alloys with a low and medium SFE after cold deformation [111]. According to the mechanism suggested in [111], SF tetrahedrons can be formed by the glide of jogged screw split dislocations. Further mechanisms of SF tetrahedrons formation are discussed in [115].

Decreasing of the stacking fault energy by alloying leads to the appearance of deformation twins at Ag concentrations of 20% and more. However, the number of grains with twins is rather small, therefore contribution of twins to the plastic deformation at HPT is most probably not significant.

5.1.2 Deformation mechanisms in nc Pd

In the section 4.1.2 results on the microstructure evolution of nc Pd were described. Two stages of deformation were distinguished, as indicated by different signatures in the microstructure evolution: first stage for shear strain, $\gamma \leq 15$, and a subsequent regime $\gamma<15$. Our results demonstrate that different deformation mechanisms can operate in the same sample as it is deformed over a wide range of strain. Microscopically, the active set of mechanisms depends on the microstructure, which itself evolves.

Let us analyse all possible deformation mechanisms which can operate in nc Pd.

Twinning. Several investigations point to twinning as possible deformation mechanism in nc materials [17,42,116]. Our microstructure analysis indeed revealed numerous twins in specimens deformed with different strain rates, and diffraction points to a substantial increase of stacking fault probability with increasing strain during early stage of deformation (Table 4.2). Twins can produce a total shear deformation $\gamma_{tw} = s_{tw} f_{tw}$, where s_{tw} is the twinning shear, $s_{tw} = 0.7$ for fcc lattice, and f_{tw} is a volume fraction of twins. Consequently twinning alone could not produce hundreds percents strain achieved during HPT.

Even though Pd has a high stacking fault energy (~180 mJ/m^2 [117]), deformation twins have been revealed in IGC nc Pd after cold rolling [17], and molecular dynamic simulations predict the development of twinning in nanocrystalline materials [48,118]. It was shown recently, that deformation twinning could be relatively easy in Pd because formation of a second partial dislocation in a neighbouring crystallographic plane is energetically preferable as compared with dragging of a trailing partial [119]. However the necessary critical stress is high in Pd [120], and deformation twinning has not been observed in this metal at HPT deformation when the grain size was 250 nm (see chapter 4.1).

Dislocation glide. Surprisingly – in view of the large strain ($\gamma \approx 10$) – the shape of the grains has not significantly changed. This is apparent in TEM observations of specimens (Fig. 4.7a,b). If dislocation glide was the dominant mechanism, we would expect an elongated ('lath-like') grain shape here. The absence of a texture in the grain shapes which is evidenced by the TEM data thus suggests that dislocation glide is either not the dominant mechanism or that another mechanism acts along with it. In fact, similar considerations in relation to data for the crystallographic texture of deformed nc metals have highlighted the role of grain boundary sliding (GBS) and grain rotation in randomizing the texture [17]. Our recent study of crystallographic texture development revealed that a typical shear texture was formed in the nc Pd-10Au samples deformed by HPT [121]. This points towards a limited contribution of dislocation slips to plastic deformation of nc alloy and indicates the activation of grain boundary sliding. Furthermore, a typical recrystallization cube texture was also found in nc specimen, in agreement with the observation of stress induced grain growth. Significantly, random texture was registered in nc Pd samples deformed by cold rolling by Dr. J. Markmann et al. [17]. The authors suggested that it an evidence of grain rotation (via grain boundary

sliding) randomizing the texture. In support of the argument, the recent investigation of nc electrodeposited Ni at large strains has shown that as deposited <111> texture disappeared after high pressure torsion for five rotations, and typical for shear deformation texture was not formed as it would be expected in case of dislocation slip [53]. In fact, similar considerations in relation to data for the crystallographic texture of deformed nc metals have highlighted the role of grain boundary sliding (GBS) and grain rotation in randomizing the texture [17].

Grain boundary sliding and grain rotation. Compression-torsion tests of nc Pd revealed a significant strain rate sensitivity, at least at the lower strains [122]. This suggests that a thermally activated process could control the deformation, possibly grain boundary sliding is such a mechanism.

Our results point towards two related phenomena at larger strain, namely the formation and activity of mesoscopic glide planes at the microscopic scale, and of shear bands at the mesoscopic scale. As the most remarkable microstructural feature we advertise structures such as those shown in Fig. 4.9 In part (a) and (b) of the figure, several neighbouring segments of grain boundaries are seen to align in parallel. Part (c) shows another peculiar feature, where individual grains have apparently suffered a large shear along a single slip plane. These features were typically observed quite frequently in samples deformed to $\gamma = 15$ at all studied strain rates, and were clearly absent in as-IGC state.

The formation of arrays of coplanar grain boundaries – as exemplified by the TEM micrographs of Fig. 4.9a,b – confirms earlier reports of similar structures in Ref. [17] and the predictions, in Ref. [47], of a kind of cooperative grain boundary sliding. The observation in Fig. 4.9b may point towards a possible mechanism of accommodation or, conceivably, of the formation of mesoscopic glide planes: When the shear plane encounters a triple junction and is stopped by a grain that is not in its alignment, the shear band follows its path by intragranular slip in the prolongation of the shear plane.

At the mesoscopic scale, our fracture surface investigations give evidence of abundant shear bands, which start out as finite-size regions of localized deformation and which grow laterally as the strain proceeds (Fig. 4.10). The microscopic structure of the shear bands, and their relation to mesoscopic glide planes, are the subject of other studies.

Such features as randomisation of texture and formation of mesoscopic shear planes extending over several grain boundaries (Fig. 4.9a,b) may be regarded as a clear evidence of GBS at room temperature deformation.

5.1.3 Deformation map for Pd

In section 5.1.1, it was suggested that the main deformation mechanism for cg and ufg Pd was full-dislocation activity. Besides in nc Pd several deformation mechanism take place. Therefore, as an attempt to summarize results from section 4.2, a deformation map for nc Pd deformed at the room temperature and pressure of 4.5 GPa (Fig. 5.1) is suggested, similarly as it was proposed for this material strained at normal pressure [17]. The map schematically show the regions where the most important deformation mechanisms are operating: for the grain size less than 40 nm these are shear banding and grain boundary sliding and grain rotation accommodated by emission of full dislocations or twinning; for larger grain sizes this is a full dislocation activity and shear banding. As the grain size is changing continuously during the deformation, primary deformation mechanisms also change with increasing shear strain. The map illustrates that grain boundary mediated processes dominate in a limited range of strains. Coarsening of the microstructure due to the stress induced grain growth leads to activation of dislocation slip.

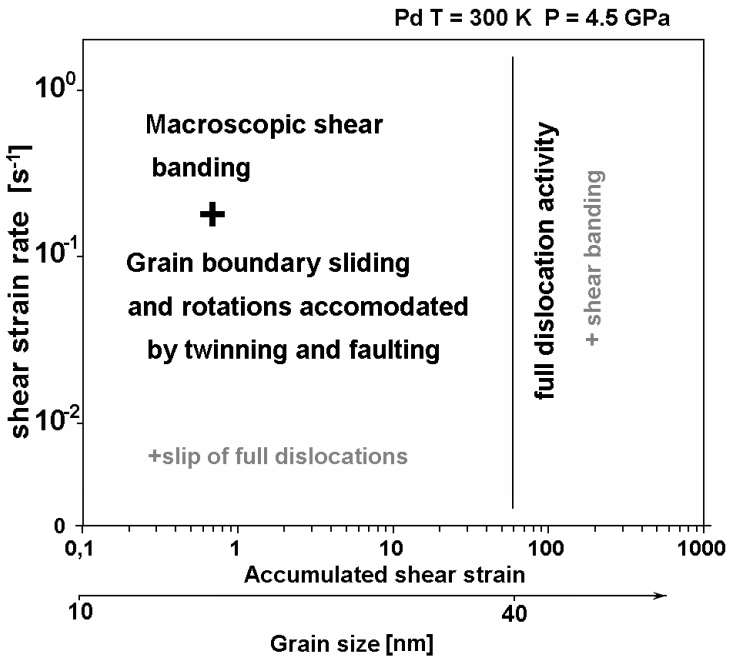


Figure 5.1 Deformation mechanisms map for nanocrystalline Pd deformed at the room temperature and pressure of 4.5 GPa. Less important mechanisms are shown in grey.

5.2 Mechanical behaviour of nc and ufg Pd and Pd alloys

Several strengthening mechanisms may operate in materials. As it was described in section 2.2, the main strengthening mechanism in nc and ufg materials is a grain size strengthening. However, there is some limit in a decreasing of the grain size, below which no further strengthening is observed. The breakdown of Hall-Petch relation was observed in several materials with a grain size about 15 nm. These materials show either softening, or no further changes of the strength.

In this chapter, we analyse which strengthening mechanisms operate in nanostructured Pd and Pd alloys and discuss principles how to obtain good combination of the strength and the ductility.

5.2.1 Strengthening mechanisms

5.2.1.1 Ultra-fine grained Pd-Ag alloys

Our results demonstrated a significant increase of strength as a result of SPD for all studied alloys, with maximal values achieved in the Pd-20% Ag and Pd-40% Ag alloys (Table 4.3). Several factors contribute to this increase of the strength: small grain size, high dislocation density, and solute hardening. Obviously, the most important factor here is the grain size hardening according to the Hall-Petch relation (Eq. 2.1) as $\sigma_{HP} \sim d^{-1/2}$. The smaller the grain size, the higher the strength, and consequently the highest values of the yield strength were obtained in alloys with the smallest grain size (Table 4.3).

The next factor contributing to the enhanced strength is the strain hardening due to dislocation storage during plastic deformation. Already Taylor has shown that, if the influence of the dislocation density on the flow stress is dominant, then its contribution to flow stress is proportional to $\sqrt{\rho}$ (Eq. 2.2). Here we would like to stress that this is valid only for randomly distributed dislocations: dislocation forest. TEM and HRTEM (Fig. 4.2, 4.4 from chapter 4.1) observations show that number of randomly distributed dislocations in grain interior increases with alloying. Furthermore, Eq. 4.1 used for estimation of dislocation density from XRD data accounts only on distortions from non-interacting dislocations, and this density increases dramatically with increasing Ag content and achieves its maximum value in the Pd-20% Ag alloy (Table 4.1).

Solution hardening is much less important for strength of the HPT-processed Pd-Ag alloys. As it was mentioned before, the system Pd-Ag is completely soluble. (Fig. 3.1a) The atomic radii of Pd and Ag are 137.6 pm and 144.4 pm, respectively. This difference in atomic diameters results only in a low solute hardening. A study performed on single crystals of Pd-Ag alloys demonstrated that in the concentration range up to 25 at.% Ag, the yield strength of alloys increases linearly with the increasing Ag concentration. Further increase of Ag leads to an (again linear) decrease of the yield strength [123]. Therefore, the maximal hardening effect was achieved for a concentration of 25% of Ag and its value was only 20 MPa.

Hence, we conclude that the enhanced yield strength of HPT-processed Pd-20% Ag and Pd-40% Ag alloys results mainly from the smaller grain size and the increased dislocation density. Upon that, slightly lower mean grain size in Pd-40% Ag, and slightly larger dislocation density in Pd-20% Ag lead to very close yield strength values in these alloys. Though, we admit that both factors are present simultaneously, it is very difficult to find out a quantitative correlation between the microstructural parameters and the flow stress, because existing theories do not describe their simultaneous influence.

5.2.1.2 Nanocrystalline Pd and Pd-10at.% Au

In Fig. 4.15, it was shown that nanocrystalline Pd and Pd-10 at.% Au demonstrate very high strength. Besides both materials showed quite similar results in the limit of error: the values of yield stress for nc Pd and Pd-10 at.% Au were 810(80) and 900(50), respectively. It means that here alloying does not play an important role as strengthening mechanisms as in the case of Pd-Ag alloys. Furthermore, as it was discussed in the section 2.2.1, the strengthening by dislocation storage also does not work in nanocrystalline materials. The grains are too small for the dislocation nucleation.

The most remarkable feature revealed in compression tests is the significant strain hardening in the early stages of plastic straining. TEM observations of nc Pd deformed by high pressure torsion straining revealed an increased density of twins (Table 4.2). Furthermore, we performed HRTEM on Pd-10 at.% Au before and after compression test (Fig. 5.2). The careful examination of TEM and HRTEM pictures revealed that in the sample after compression the twin density is 1.5 times higher than in non-deformed state.

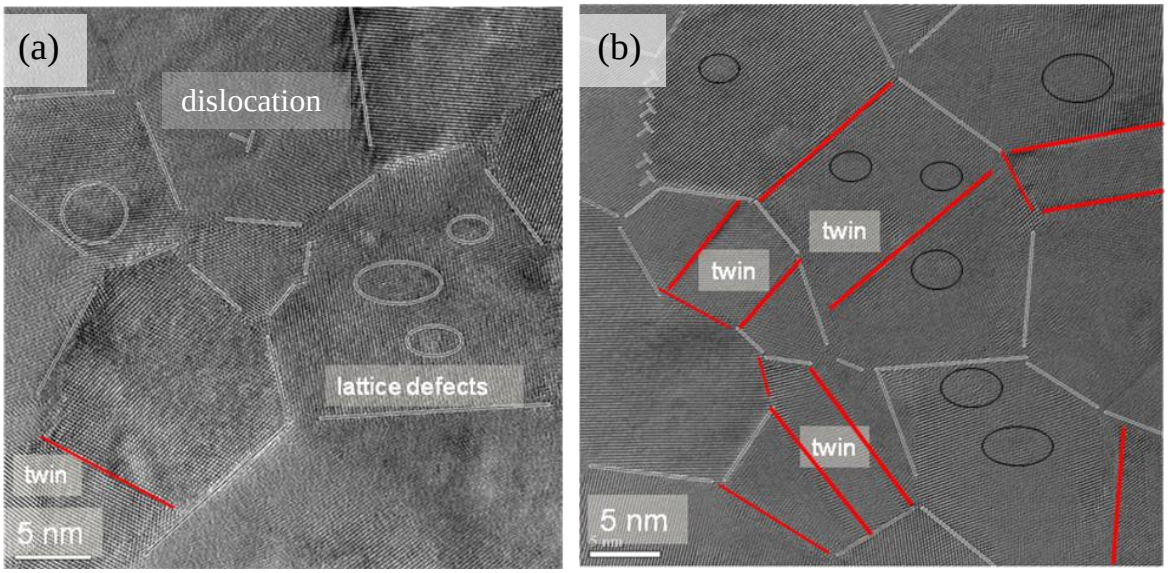


Figure 5.2 HRTEM of nc Pd-10at.% Au **(a)** before and **(b)** after compression test to strain 0.06. Gray lines show high-angle grain boundaries, red lines – coherent grain boundaries, circles denote lattice defects. For determination the software Digital Micrograph and function FFT were used. [HRTEM by Dr. Ch. Kübel from INT, KIT CN]

Most probably the twinning is the deformation mechanism responsible for rapid straining hardening on the early stage on deformation during compression tests. As for compression-torsion straining [122] the rapid stress increase in the beginning of plastic straining is necessary for forming the mesoscopic shear planes. As more and more such plains form, the hardening rate decreases, until the level of stress is sufficient to maintain the necessary number of cooperative grain boundary sliding.

Assuming the twinning is also a kind of grain boundary mediated mechanisms, while twins are coherent grain boundaries. It can be concluded that grain boundary mediated mechanisms are the main strengthening mechanisms for nanocrystalline materials. Therefore alloying does not influence much on the level of strength in Pd and Pd alloys, as these materials have similar value of elastic modulus (Table 3.1).

5.2.2 Analysis and tailoring of ductility in nanocrystalline metals

According to Hart's criteria (Eq. 2.3) for good ductility the material should show either the strain-rate sensitivity or the strain hardening.

5.2.2.1 Improving ductility by alloying in Pd-Ag alloys

Usually ufg materials fail to exhibit a reasonable uniform elongation due to their limited strain hardening capacity (see chapter 2.3). The strain hardening capacity (SHC) reflects the ability of the material to store dislocations produced during plastic deformation, which is difficult in small grains because grain boundaries which can act as dislocation sinks are in direct vicinity.

We performed an analysis of the strain hardening capacity. Fig 5.2 shows the normalized strain hardening rate (Θ) versus true stress calculated as:

$$\Theta = \frac{1}{\sigma}\frac{\mathrm{d}\sigma}{\mathrm{d}\varepsilon}, \qquad (5.2)$$

where σ denotes the true stress and ε the true strain. Only segments of the tensile curves in Fig. 4.12 corresponding to the uniform elongation of the sample (i.e., between open squares and open circles) were used for the calculation of Θ. It proves that Θ increases with the increase of the Ag content higher than 20 %.

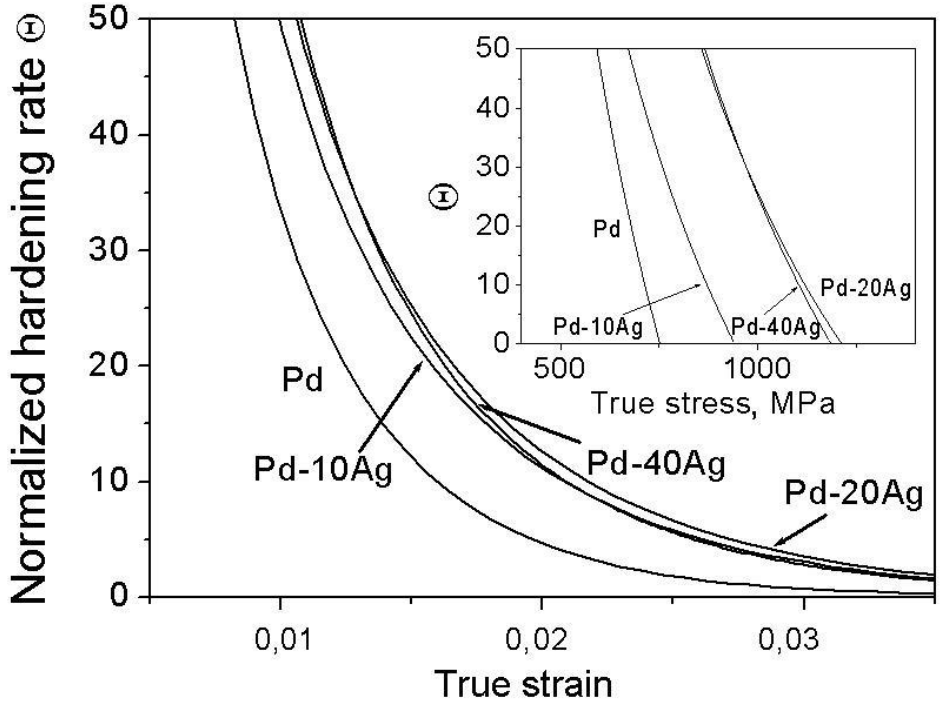


Figure 5.3 Normalized work hardening rate θ against true strain and stress.

At a first glance we observe an unusual behaviour in the Pd-Ag alloys: the highest uniform elongation was found in the Pd-20% Ag alloy, whereas the mean grain size in this alloy is almost two times smaller than that in pure Pd (Table 4.1, Table 4.3).

It is common knowledge, that the dislocation density in SPD materials is low, because dislocations usually sink into grain boundaries or self-organize into ordered substructures like cell and subgrain boundaries [9]. A typical example for this is represented by the microstructure of HPT-processed Pd (Fig. 4.1a, 4.2a). However, in the Pd-20% Ag and the Pd-40% Ag alloys dislocation tangles can be seen in all grains and the dislocation density is almost one order of magnitude higher compared to that of pure Pd. As was discussed above, the enhanced dislocation storage is enabled by the lower SFE in the Pd-20% Ag and the Pd-40% Ag alloys compared to pure Pd which leads to a dislocation dissociation and impedes deformation recovery. Obviously, these pre-existing dislocations are not involved in the plastic flow during tensile testing, because otherwise stress-strain curves would demonstrate no or very low strain hardening which is not the case. On the other hand, pre-existing dislocations may provide sources for new dislocations, and act as barriers for dislocation glide (e.g. Peierls-Nabarro and Cottrell locks). The first provides the necessary source for dislocations, and the second hinders dislocations from sinking into the grain boundaries. The annihilation of dislocations is also retarded because cross slip of split dislocations is difficult. Therefore, such a unique UFG microstructure with high density of pre-existing dislocations as formed in the Pd-Ag alloys as a result of HPT does not only provide a significant increase of the yield strength as compared to pure Pd, but it also helps to sustain further straining due to the enhanced hardening rate.

In the range of Ag content from 20 at.% to 40 at.%, further decreasing of γ_{SF} and increasing of splitting distance of dislocations lead to transition of deformation mechanism from faulting to twinning. The transition is accompanied by a slight decrease of the dislocation density (Table 4.1) and increasing of the volume fraction of grains with nano-twins inside. It was shown by Zhao et al. [110] that formation of deformation of nano-twins results in both a more effective blockage of dislocation slip and a larger amount of dislocation accumulation sites. Therefore, in the concentration range of Ag between 20 and 40 % we observe the interplay of two mechanisms of SHC improvement: one is based on the formation of stacking faults, and the second one on the formation of nano-twins. This interplay promotes the persistence of high mechanical properties in a wide concentration range.

5.2.2.2 Improved ductility in Pd with bimodal microstructure

In the section 2.2, it was already mentioned that bimodal grain size distribution is one effective method to tailor ductility. Recent work has confirmed this approach. Nanostructured Pd with bimodal grain size distribution demonstrates higher values of strain rate sensitivity. As it was calculated, the strain rate sensitivity of Pd with bimodal structure was 0.1. This value is higher than in nc Pd which has $m = 0.05$. The enhanced strain rate sensitivity slows down early necking and prevents catastrophic failure. However, the only relatively high value of the strain-rate sensitivity could not lead to a good ductility. Most probably, the obtained ductility is a result of both, strain rate sensitivity and strain hardening. Samples showed 30% strain hardening of the yield stress.

Our result confirms that usage of bimodal structure is one effective approache to obtain good combination and ductility: nanograins impart the high strength, whereas the micrometer-sized grains provide strain hardening mechanisms and potentially high tensile ductility. Furthermore, it could be suggested that by adjusting the volume fraction and the grain size one has an opportunity to further improve ductility. Possibly, decreasing of the volume fraction of small grains in the tested samples would prevent strain localization – the reason of samples' fracture – and improve the ductility with some loss in the strength.

5.2.2.3 Inherent plastic instability of nanocrystalline Pd and Pd-10at.% Au

In the section 4.2.2, results of the investigation of nanocrystalline Pd and Pd-10at.% Au with a grain size of 15 nm were presented. It was shown that samples demonstrate high strength and ductility in compression and no plastic strain in tension.

Strain rate jump tests (Fig. 4.17) demonstrate that the value of strain rate sensitivity is very low, $m = 0.05$.

The most remarkable feature revealed in the compression tests is the significant strain hardening in the early stages of plastic straining. The mechanical tests of Pd and Pd-10at.% Au with a mean grain size of 15 nm revealed strain hardening by 60-80% of the yield strength. Yet, even though the strain hardening is quite significant, it does not prevent strain localization. For the estimation of strain hardening exponent, some corrections of the experimental data were need.

True stress and true strain were estimated using Eq. 3.8 and Eq. 3.10. Furthermore, we performed additional corrections for true strain (Fig. 5.4a):

$$\varepsilon_{true}{}^{*} = \varepsilon_{true} - (\sigma^{*}) \times s \qquad (5.3),$$

where ε_{true} and $\varepsilon_{true}{}^{*}$ are the true strain and corrected true strain, consequently; s is the slope of the elastic part of stress-strain curve.

The work hardening was analyzed in terms of Ludwik's constitutive law [124] for the variation of flow stress, σ_F, with strain, ε, namely

$$\sigma_F(\varepsilon) = \sigma_{02} + k\,\varepsilon^{n}. \qquad (5.4);$$

here n denotes a work hardening coefficient and k a constant. We ignore here the strain rate sensitivity. Note also that, for $n \approx 0$, Ludwik's law predicts an initially fast increase of the flow stress, which levels off after very little plastic flow. In this respect, Eq. 5.4 catches – qualitatively – an apparent feature of the experimental data (Fig. 4.15).

The ε-derivative of Ludwik's law is a power law, $d\sigma/d\varepsilon \propto \varepsilon^{n-1}$. A plot of $d\sigma/d\varepsilon$ versus ε on log-log scales will thus exhibit straight-line behaviour with the slope $(n - 1)$. Examples of this type of plot are shown in the insert in Fig. 5.4b for an nc Pd and for a nc Pd-Au sample. Remarkably, both data do show straight-line behaviour over the entire plastic deformation range. Similar graphs were obtained with all samples. This suggests that Ludwik's law provides a good representation of the constitutive behaviour of nanocrystalline Pd and Pd-10at.% Au. The straight lines of the best fit in Fig. 4.15c have the slope of -0.95(2) which implies $n = 0.05(2)$.

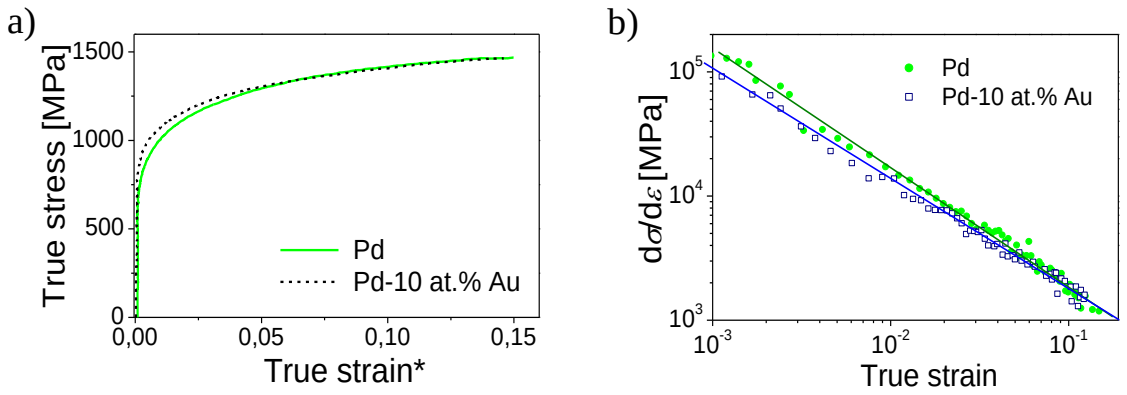


Figure 5.4 (a) True stress vs. corrected true strain for compression tests on Pd and Pd-10at.% Au at strain rate 5×10^{-4}. **(b)** A plot of derivative of true stress, σ, with respect to strain, ε, versus ε for nc Pd and Pd-10 at.% Au. Symbols: experimental data; line: straight line of best fit.

The flow stress obeys Ludwik's law with a single strain hardening exponent n over the full range of plastic flow. The estimated n value is very small, $n = 0.05$. Since the strain rate sensitivity is also low, $m \sim 0.05$, the material does not satisfy the requirements for stable plastic flow. The low values of both n and m suggest small tolerance of nc specimens to stress heterogeneity, which will here inevitably lead to strain localization (note compression specimen buckling in Fig. 4.14).

This is well compatible with the brittle behavior in the tensile tests. One consequence of strain localization is apparent in the fracture behavior. Both in tensile and compression tests the crack proceeds in a plane normal to the largest tensile stress (Fig. 4.14). This observation is typical for brittle fracture. Indeed, even in compression tests where these materials demonstrate ductile deformation, fracture surfaces are flat and smooth as in brittle failure. Even though high magnification reveals traces of microplasticity (Fig. 5.5), the observations are all consistent with low fracture toughness.

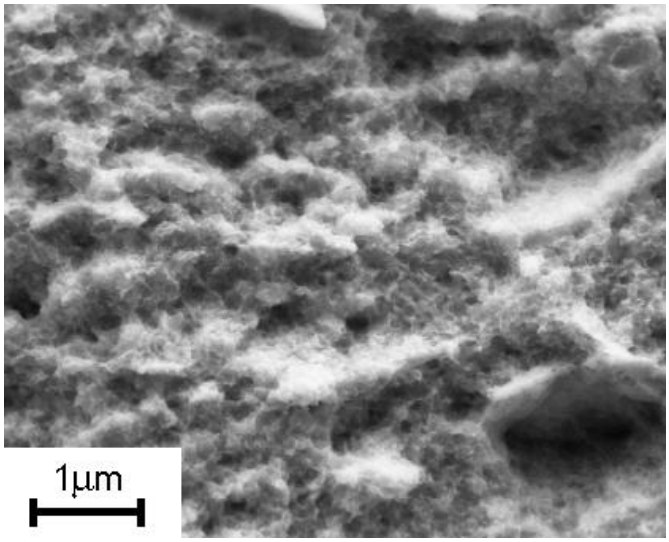


Figure 5.5 High magnification fracture surface of IGC Pd showing traces of microplasticity (dimple-like appearance). [SEM images of fracture surface from K. Yang, Uni Ulm]

Note, that the brittleness of investigated materials is not linked to possible flaws in the microstructure (see section 4.2.2 and Fig. 4.13), but that they appear to be inherent properties of the nanocrystalline state of the samples.

Chapter 6

Summary and Outlook

In the present work a complete experimental data base was obtained for the mechanical behavior (strength, ductility etc.) of nanocrystalline Pd, Pd-Ag and Pd-Au alloys using new testing equipment for miniaturized specimens under tensile, compression and compression-torsion conditions in a wide range of strain rate (10^{-5} - 10^{1} c^{-1}).

The main goal of investigating nanocrystalline materials as a structural material is to achieve a good combination of strength and ductility (Fig. 6.1).

As it was described in 2.3.1, a significant strengthening of nanostructured materials can be achieved by grain refinement, alloying and/or dislocation storage. Usually nc materials fail to show good ductility. However, several routes to improve the ductility together with high strength were suggested, such as generating bimodal grain size distributions, nano-twins, dispersion of nano-particles, etc.

By variation of the concentration of the alloying material the combination of high strength and good ductility was obtained in the alloys with a concentration of Ag from 20 % up to 40 % **which represent the strongest noble metal alloys ever made with a fracture strength of up to 2 GPa, i.e. 2-3 times that of conventional steels**.

It is further proposed that improved ductility is related to the enhanced dislocation storage and strain hardening capacity in these alloys due to the decreased stacking fault energy. Obtained results proofed that the method of increasing SFE can be used to control the mechanical properties in ufg alloys.

As for pure nanocrystalline materials with narrow grain size distribution in general, all studied specimens were relatively brittle in tensile mode, and very ductile in compression. We emphasize that these properties are not linked to possible flaws in the microstructure, but that they appear to be inherent properties of the nanocrystalline state of the samples. We analysed the parameters that control a material's potential for ductility in tension, namely, the strain hardening exponent (n) and the strain rate sensitivity exponent (m), and revealed that both values are low in nc state at approximately $n \approx m \approx 0.05$. This leads to a rapid development of plastic instability and in the case of tensile load to relatively rapid fracture (still not like glass). However, ductility of nanocrystalline Pd can be improved by introducing bimodal grain size distribution, however with a loss of strength.

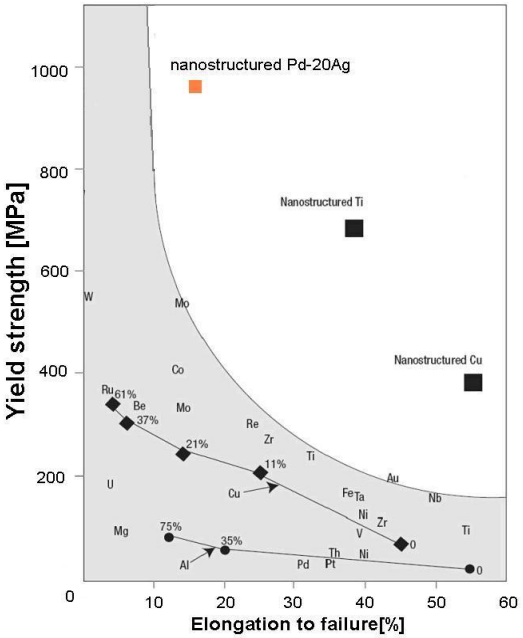


Figure 6.1 Strength and elongation to failure of nanostructured metals compared to conventional grain-sized metals. The lines indicate the influence of cold working on strength and ductility of Cu and Al. % markings represent the degree of cold working. The higher the working degree the higher the strength and lower the ductility. After Ref. [82]

The results on mechanical properties are summarized in Table 6.1.

Table 6.1 Summary of average grain size (d) and mechanical properties (strain rate [ἑ], yield stress [YS], ultimate stress [UTS] and uniform elongation [ε_u]) for Pd and Pd alloys.

Material	d, nm	ἑ, s^{-1}	YS, MPa	UTS, MPa	ε_u, %
Tension					
cg Pd, annealed	>1000	10^{-3}	80	195	33
nc Pd, as-IGC,	14	10^{-3}	>320	-	-
bi-modal ns Pd IGC+HPT	110	10^{-3}	800	1050	3
ufg Pd, as-cast+HPT	240	10^{-3}	628	760	3,5
ufg Pd-20 at.% Ag, as-cast+HPT	150	10^{-3}	975	1215	5,5
Compression					
nc Pd, as-IGC	14	$5x10^{-4}$	810	1470	15
nc Pd-10at. % Au, as-IGC	13	$5x10^{-4}$	900	1470	15

It is known that different factors can influence the result of microstructure after SPD, first of all initial microstructure, as well as chemical composition and conditions of the deformation. Furthermore, these factors have an effect on the minimum grain size that can be reached in materials by SPD. In the present thesis, it was confirmed that HPT deformation has a different influence microstructure evolution of materials with different initial structures. In the case of the initial cg material, HPT with a strain of $\gamma = 300$ leads to a grain size refinement down to 240 nm in Pd samples (Fig. 4.1a). The microstructure developed has slightly elongated grains. As for the initially nc state, significant grain coarsening was observed in deformed samples. After $\gamma = 300$ the microstructure consists of elongated grains with 150 nm in normal to strain direction (Fig. 4.12). Besides, several regions with less elongated grains were observed.

It is already known that there steady state in structural refinement during SPD can be achieved. We suppose that in the Pd grain size the steady state is about 200-240 nm. Stages that are involved in the formation of that grain size are listed in Table 6.2.

Table 6.2 Stages in deformation of Pd with initially coarse grained and nanocrystalline nanostructure.

Initially nc material	Initially cg material
Slightly grain growth. Increase of twin density.	Increase of dislocation density. Formation of dislocation walls
Grain growth in shear direction.	Formation of substructure with low-angle boundaries
Increase of dislocation density inside of elongated grains	Decrease of sub-structure size. Increase of grain boundaries misorientation.
Formation of slightly elongated grains with grain size about 200 - 240 nm	

The fundamental understanding of the deformation mechanisms operating in nanocrystalline materials is very important in order to predict their mechanical properties, and is necessary for a scientifically justified design of new materials.

As an outlook, it would be interesting to study samples with different kind of bimodal grain size distribution. Here it was demonstrated that bimodal samples demonstrated the best compromise in terms of mechanical properties. Besides, one can further enhance the ductility by decreasing the volume fraction of small grains that would prevent strain

localization – the reason of sample's fracture – and would increase the ductility with some loss in the strength. Moreover, it would be interesting to study as-IGC samples with different Au content. In the recent study the alloying with 10 at. % Au was used generally to prevent room-temperature grain growth. However, the systematic study of influence of the Au content could reveal samples with improved mechanical properties. As an example, in the Pd-Ag system best mechanical properties were obtained for a samples with 20 at.% Ag.

In this thesis it was shown that fully dense nanocrystalline pure noble metal exhibit the highest strength ever achieved for noble metals. Moreover, the alloying with second noble metal improves even further strength and ductility of the materials. We suppose that these results could find engineering application in a wide range from MEMS devices, microassembly techniques to jewelry, where noble metals are widely used and show largely improved strength, as well as wear and corrosion resistance.

Appendix

A. Kinetic analysis of nanocrystalline materials

As a general trend during the last three years several attempts have been made to perform the analysis of plastic deformation kinetics in nc materials by means of strain rate change (jump) tests and relaxation tests at different temperatures. This analysis was developed and successfully used for coarse grained materials in the past to determine the stress-strain rate parameters of deformation processes which often allows to reveal (or exclude) the operating deformation mechanism. In the case that the deformation mechanism uniquely determines the strain rate $\dot{\gamma}$, corresponds to [125,126]:

$$\dot{\gamma} = \dot{\gamma}_0 \exp\left(-\frac{\Delta G(\tau_e^*)}{kT}\right) = \dot{\gamma}_0 \exp\left(-\frac{\Delta F - \tau_e^* \Delta V^*}{kT}\right) \qquad \text{(A.1)}$$

where k is the Boltzmann constant and T is the temperature; $\dot{\gamma}_0$ is a pre-exponential constant or a characteristic strain rate at a given grain size d; ΔG is the Gibbs free energy of activation for the stress-assisted, thermally activated process; ΔF and ΔV* are the Helmholtz free energy (activation energy) for overcoming the obstacles to dislocation motion and the effective stress activation volume, respectively.

ΔG is a decreasing function of the effective shear stress τ_e^* , as the activation barrier is lowered by the work done by the effective stress, $\tau_e\Delta$. $\Delta V^* = \partial G/\partial \tau^*$ and τ_e^* is the thermal component of the total stress, τ, i.e., τ_e^* accounts for the stress needed to overcome the short-range barrier responsible for the temperature and strain-rate dependence. The applied shear stress τ_e^* has two components,

$$\tau = \tau^* + \tau_\mu \qquad \text{(A.1)}$$

where τ_μ is the athermal contribution to the flow stress, resulting from long-range internal stresses impeding the plastic flow, the temperature dependence of which is weak and mainly due to that of l (shear modulus). The applied τ* is in normal cases the effective τ_e^*. The shear stress τ and its components are related to the normal stress σ and its corresponding components by the Taylor orientation factor.

The activation volume ΔV can be found from following equations based on Eq. A.1.1 when T = const:

$$\ln[\dot{\gamma}(\tau_1)/\dot{\gamma}(\tau_2)] = \frac{\Delta V}{kT}(\tau_1 - \tau_2) \qquad \text{(A.2)}$$

The shear stress τ and its components are related to the normal stress σ and its corresponding components by the Taylor orientation factor. With the Von Mises yield criterion, $\tau = \sigma / \sqrt{3}$. Similarly, for the shear and normal strain rates, $\dot{\gamma} = \sqrt{3}\dot{\varepsilon}$.

Using strain rate jump tests (Fig. 3.6), an apparent activation volume, ΔV, can be obtained from the Eq. A.1.2:

$$V = \frac{\sqrt{3}kT \ln(\dot{\varepsilon}_2 / \dot{\varepsilon}_1)}{\sigma_2 - \sigma_1} \qquad \text{(A1.3)}$$

where σ is the flow stress and $\dot{\varepsilon}$ is the strain rate. Flow stresses σ_2 and σ_1 correspond to strain rate $\dot{\varepsilon}_2$ and $\dot{\varepsilon}_1$, and $\sigma_2 > \sigma_1$. The activation volume was estimated approximately for a number of deformation mechanisms. For example,

$\Delta V = 10 \ldots 10^2 b^3$ for dislocation slip and cross slip,

$\Delta V = 1b^3$ for dislocation climb, Coble creep and grain boundary sliding,

$\Delta V > 10^2 b^3$ for intersecting forest dislocations.

Another important parameter which can be obtained from strain rate jump tests is the strain rate sensitivity m. It is given as:

$$m = \left(\frac{\partial \ln \sigma}{\partial \ln \dot{\varepsilon}} \right)_{\gamma,T} = \frac{\log(\sigma_2 / \sigma_1)}{\log(\dot{\varepsilon}_2 / \dot{\varepsilon}_1)} \qquad \text{(A.4)}$$

In coarse grained materials, the strain rate sensitivity is always low, $m << 0.01$ at room temperature, but it increases with increase of temperature. For superplastic deformation, when primary deformation mechanism is grain boundary sliding, the value of $m \geq 0.3$.

B. List of abbreviations and symbols

Latin symbols and abbreviation

b.c.c.	body-centered cubic (lattice structure)	
CG	coarse grained	
D	grain size	nm
<D>	crystallite size (from XRD)	nm
ECAP	equal channel angular pressing	
ED	electrodeposition	
f.c.c.	face-centered cube (lattice structure)	
FWHM	full width at half maximum	
G	elastic shear modulus	GPa
GB	grain boundary	
GBS	grain boundary sliding	
GS	grain size	nm
H-P	Hall-Petch (relation)	
h.p.c	hexagonal close-packed (lattice structure)	
HV	microhardness	
HPT	high pressure torsion	
IGC	inert gas condensation	
m	strain rate sensitivity	
MD	molecular dynamic	
nc	nanocrystalline	
ns	nanostructure/nanostructure	
SEM	scanning electron microscopy	
SFE	stacking fault energy	
SHC	strain hardening capacity	
SPD	severe plastic deformation	
T_m	melting temperature	^oC
TEM	transmission electron microscopy	
TJ	triple junction	
ufg	ultra-fine grained	
UTS	ultimate stress	MPa

ΔV	activation volume	
XRD	X-ray diffraction	
YS	yield stress	MPa

Greek symbols

α_{SF}	Warren stacking fault	%
$\delta(\theta)$	full width at half maximum	
ε	Strain	
$<\varepsilon^2>^{1/2}$	microstrain (for XRD)	%
$\dot{\varepsilon}$	strain rate	s^{-1}
λ	wave length	pm
ρ	dislocation density	$x10^{15}$, m^{-2}
σ	stress	MPa
τ	shear stress	MPa
2θ	scattering angle	^{o}
θ	normalized work hardening rate	
γ	shear strain	
γ_{sf}	stacking fault energy	mJ/m^2
$\dot{\gamma}$	shear strain rate	s^{-1}

References

1. E.O. Hall. Proc. Phys. Soc. (London), Sect.B, *The deformation and ageing of mild steel: III Disscussion of results*, **64**, 747 (1951).
2. N.J. Petch. J. Iron Steel Inst., *The cleavage strength of polycrystals*, **174**, 25 (1953)
3. C.C. Koch, Scripta Mater., *Optimization of strength and ductility in nanocrystalline and ultrafine grained metals*, **49**, 657 (2003)
4. H. Van Swygenhoven, Science, *Polycrystalline materials - Grain boundaries and dislocations*, **296**, 66 (2002)
5. R.W. Siegel, Nanostructured materials, *Nanostructured materials – mind or matter-*, **4**, 121 (1994)
6. K.S. Kumar, H. Van Swygenhoven, S. Suresh, Acta Mater., *Mechanical behaviour of nanocrystalline metals and alloys*, **51**, 5473 (2003)
7. R.Z. Valiev, H. Hahn, T.G. Langdon. Adv. Eng. Mater. Special Issue "Bulk Nanostructured Metals: New Ideas for Innovation *Editorial*, **12 (8)**, 665 (2010)
8. H. Gleiter, Progr. Mater. Sci., *Nanocrystalline materials*, **33**, 223 (1989)
9. R.Z. Valiev, R.K. Islamgaliev, I.V. Alexandrov. Progr. Mater. Sci., *Bulk nanostructured materials from severe plastic deformation*, **45**, 103 (2000)
10. A. Zhilyaev, T.G. Langdon. Progr. Mater. Sci., *Using high-pressure torsion for metal processing : Fundamentals and application*, **58**, 893 (2008)
11. R.Z. Valiev, Y. Estrin, Z. Horita, T.G. Langdon, M.J. Zehetbauer, Y.T. Zhu. JOM, *Producing bulk ultrafine-grained materials by severe plastic deformation*, **58**, 33 (2006)
12. R.Z. Valiev, M.J. Zehetbauer, Y. Estrin, H.-W. Höppel, Yu. Ivanisenko, H. Hahn, G. Wilde, H.J. Roven, X. Sauvage, T.G. Langdon. Adv. Eng. Mater., *The innovation potential of bulk nanostructured materials*, **7**, 527 (2007)
13. R.Z. Valiev, I.P. Semenova, V.V. Latysh, H. Rack, T.C. Lowe, J. Petruzelka, L. Dluhos, D. Hrusak, J. Sochova. Adv. Eng. Mater., *Nanostructured titanium for biomedical application*, **10**, B15 (2008)
14. M. Dao, L. Lu, R.J. Asaro, J.T.M. De Hooson, E. Ma. Acta Mater. *Toward a quantitative understanding of mechanical behavior of nanocrystalline metals*, **55**, 4041 (2007)

15. M.A. Meyers A. Mishra, D.J.Benson, Prog. Mater. Science, *Mechanical properties of nanocrystalline materials*, **51**, 427 (2006)
16. R. Birringer, H. Gleiter, H.-P. Klein, P. Marquardt, Phys. Lett. A, *Nanocrystalline materials an approach to a novel solid structure with gas-like disorder?* **102**, 365 (1984)
17. J. Markmann, P. Bunzel, H. Rosner, K.W. Liu, K.A. Padmanabhan, R. Birringer, H. Gleiter, J. Weissmüller, Scripta Mater., *Microstructure evolution during rolling of inert-gas condensed palladium*, **49**, 637 (2003)
18. Y.M. Wang, E. Ma, Acta Mater., *Three strategy to achieve uniform tensile deformation in nanostructured metal*, **52**, 1699 (2004)
19. E. Ma, JOM, *Eight routes to improve the tensile ductility of bulk nanostructured metals and alloys*, **4**, 49 (2006)
20. Y.H. Zhao, Y.T. Zhu, X.Z. Liao, Z. Horita, T.G. Langdon. Mater. Sci. Eng. A, *Determining the optimal stacking fault energy for achieving high ductility in ultrafine-grained Cu–Zn alloys*, **463**, 22 (2008)
21. Y.H. Zhao, Y.T. Zhu, X.Z. Liao, Z. Horita, T.G. Langdon. Appl. Phys. Lett., *Tailoring stacking fault energy for high ductility and high strength in ultrafine grained Cu and its alloy*, 89, 121906 (2006)
22. H. Gleiter in *Deformation of Polycrystalls: mechanisms and microstructure*. (eds) Hanse, S. Horsewell, T. Leffers, M. Linilt, Roskilde, Denmark, Riso National laboratory, 1981 p. 15
23. C.C. Koch, Nanostr. Mater., *The synthesis and structure of nanocrystalline materials produced by mechanical attrition: A review*, **2**, 109 (1993)
24. H.-J. Fecht, E. Hellstern, Z. Fu, W.L. Johnson, Metall. Trans. A, *Specific-heat anomaly during vitrification of hydrided Fe_2Er single crystals*, **21(9)**, 2333, (1990)
25. U. Erb, Nanostr. Mater., *Electrodeposited nanocrystals: Synthesis, properties and industrial applications*, **6(5-8)**, 243 (1995)
26. R. Beckerdike, D. Clarck, J.N. Easterbrook, G. Hughes, W.N. Mair, P.G. Partridge, H.C. Ranson, Int. J. Rapid. Solidif., *Microstructures and tensile properties of vapour deposited Aluminium alloys. Part2: Co-deposited alloys*, **1**, 305 (1985)
27. W. Chang, G. Skandan, S.C. Danforth, M. Rose. A.G. Balogh, H.Hahn, B. Kear, Nanostr. Mat., *Nanostructured ceramics synthesized by chemical vapor condensation*, **6**, 321 (1995)

28. G.W. Nieman, J.R. Weertman, R.W. Siegel, Scr. Metall., *Microhardness of nanocrystalline palladium and copper produced by inert-gas condensation,* **23**, 2013 (1989)
29. M. Ames, J. Markmann, R. Karos, A. Michels, A. Tschöpe, R. Birringer, Acta Mater., *Unraveling the nature of room temperature grain growth in nanocrystalline materials*, **56**, 4255 (2008)
30. U. Erb. K.T. Aust, G. Palumbo in *Nanostructured Materials.: Process., Properties, Applic*. Ed C.C. Koch, William Andrew Publisher, 2002, Norwich, NY p. 179
31. V.M. Segal, V.I. Reznikov, A.E. Drobyshevkij, V.I. Kopylov, Metally, *Plastic deformation of metals by pure shearing,* **1**, 115 (1981), in Russian
32. R.Z. Valiev, N.A. Krasilnikov, N.K. Tsenev, Mater.Sci Eng. A., *Plastic Deformation of Alloys with Submicro-Grained Structure*, **137**, 35 (1991)
33. R.Z. Valiev, T.G. Langdon, Prog. Mater. Sci., *Principles of equal-channel angular pressing tool for grain refinement,* **51**, 881 (2006)
34. P.W. Bridgman. J. Appl. Phys., *On Torsion Combined with Compression*, **14**, 273 (1943)
35. N.A. Smirnova, V.I. Levit, V.I. Pilyugin, R.I. Kuznetsov, L.S. Davydova, V.A. Sazonova, FMM, *Microstructure evolution in fcc monocrystalls after severe plactic deformation,* **61(6)**, 1170 (1986), in Russian
36. R.Z. Valiev, O.A. Kaibyshev, R.I. Kuznetsov, R.S. Musalimov, N.K. Tsenev, Doklady Akad Nauk SSSR, *Low-temperature superplasticity of metallic materials,* **301(4)**, 864 (1988), in Russian
37. F.C. Frank, W.T. Read, Phys. Rev., *Multiplication processes for slow moving dislocations,* **79(4)**, 722, (1950)
38. J.A. Venables, J. Phys. Chem. Solids, *The nucleation and propagation of deformation twins*, **25**, 693(1964)
39. V. Yamakov, D. Wolf, S.R. Phillpot, A.K Mukherjee, H. Gleiter, Nature, *Dislocation processes in the deformation of nanocrystalline materials*, **1**, 45 (2002)
40. H. Van Swygenhofen, P.M. Detlef, A. Hasnaoui, Phys.Rev.Lettr. B, *Atomic mechanism for dislocation emission from nanosized grain boundary*, **66,** 024101 (2002)
41. J. Schiotz, K.W. Jacobsen, Science, *A maximum in the strength of nanocrystalline copper*, **301**, 1357 (2003)

42. X.Z. Liao, S.G. Srinivasan, Y.H. Zhao, M.I. Baskes, Y.T. Zhu, F. Zhou, E.J Lavernia, H.F. Xu, Appl Phys Lett, *Formation mechanism of wide stacking faults in nanocrystalline Al*, **84**, 3564 (2004)
43. M.W. Cheng, E. Na, K.J. Hemker, H.W. Sheng, Y.M. Wang, X.M Cheng, Science, *Deformation twinning in nanocrystalline aluminum*, 300, 1275 (2003)
44. X. Wu, Y.T. Zhu, M.W. Chen, E. Ma, Scr. Mater., *Twinning and stacking fault formation during tensile deformation of nanocrystalline Ni,* **54**, 1685 (2006)
45. H. Rösner, J. Markmann, J. Weissmüller, Philos. Mag. Lett., *Deformation twinning in nanocrystalline Pd*, **84**, 321 (2004)
46. Y.T. Zhu, X.Z. Liao, S.G. Srinivasan, E.J Lavernia, J. Appl. Phys., *Nucleation of deformation twins in nanocrystalline face-centered-cubic metals processed by severe plastic deformation*, **98**, 034319 (2005)
47. H. Hahn, P. Mondal, K.A. Padmahnabhan, Nanostr. Mater., *Plastic deformation in nanocrystalline materials*, **9**, 603 (1991)
48. H. Van Swygenhoven and P. Derlet, Phys. Rev. B, *Grain-boundary sliding in nanocrystallinefcc metals*, **64**, 224105 (2001)
49. A. Hasnaoui, H. Van Swygenhoven and P.M. Derlet, Phys. Rev. B, *Cooperative processes during plastic deformation in nanocrystalline fcc metals: A molecular dynamic simulation,* **66**, 184112 (2002)
50. Y.M. Wang, E. Ma, M.W. Chen, Appl. Phys. Lett., *Enhanced tensile ductility and toughness in nanostructured Cu*, **80**, 2395 (2002)
51. J. Weissmüller, J. Löffler, M. Kleber, Nanostruct. Mater., *Atomic structure of nanocrystalline metals studied by diffraction techniques and EXAFS*, **6**, 105 (1995)
52. M. Legros, D.S. Gianola, K.J. Hemker, *In situ TEM observations of fast grain boundary motion in stressed nanocrystalline aluminum films,* Acta Mater., **56**, 3380 (2008)
53. X.Z. Liao, A.R. Kilmametov, R.Z. Valiev, H. Gao, X. Li, A.K. Mukherjee, J.F. Bingert, Y.T. Zhu. Appl. Phys. Lett., *High-pressure torsion-induced grain growth in electrodeposited nanocrystalline Ni*, **88**, 021909 (2006)
54. K. Zhang, J.R. Weertman, J.A. Eastman, Appl. Phys. Lett., *The influence of time, temperature, and grain size on indentation creep in high-purity nanocrystalline and ultrafine grain copper*, **85**, 5197 (2004)

55. M. Winning, G. Gottstein, L.S. Schvindlerman, Mater. Sci. Eng. A, *Migration of grain boundary under the influence of an external shear stress*, **317**, 17 (2001)

56. M. Winning, Acta Mater., *Motion of <100>-tilt boundaries*, **51**, 6465 (2003)

57. J.W. Cahn, Y. Mishin, A. Suzuki, Acta Mater., *Coupling grain boundary motion to shear deformation*, **54**, 4953 (2006)

58. D. Pan, S. Kuwano, T. Fujita, M.W. Chen, Nano Letters, *Ultra-large room-temperature compressive plasticity of a nanocrystalline metal*, **7**, 2108 (2007)

59. G.J. Fan, L.F. Fu, D.C. Qiao, H. Choo, P.K Liaw, N.D. Browning, Scripta Mater., *Grain growth in a bulk nanocrystalline Co alloy during tensile plastic deformation*, **54(12)**, 2137 (2006)

60. G.J. Fan, Y.D. Wang, L.F. Fu, H. Choo, P.K. Liaw, Y. Ren, N.D. Browning, Appl. Phys. Lett., *Orientation-dependent grain growth in a bulk nanocrystalline alloy during the uniaxial compressive deformation*, **88**, 171914 (2006)

61. J. Schiotz, F.D.Di Tolla, K.W. Jacobsen, Nature, *Softening of nanocrystalline metals at very small grain sizes*, **391**, 561 (1998)

62. H. Iwasaki, K. Higashi, T.G. Nieh Scr. Mater., *Tensile deformation and microstructure of a nanocrystalline Ni–W alloy produced by electrodeposition*, 50, 395 (2004)

63. J.R. Weertman 2002 in Koch C (ed.) Nanostructured material, Noyes Publications, Norwich, NY 393-417

64. F. Dalla Torre, P Spatig, R. Schaublin, M. Victoria, Acta Mater., *Deformation behavior and microstructure of nanocrystalline electrodeposited and high pressure torsioned nickel*, **53**, 2337 (2005)

65. Y.J. Li, J. Mueller, H.W. Höppel, M. Göken, W. Blum, Acta Mater., *Deformation kinetics of nanocrystalline nickel*, **55**, 5708 (2007)

66. Y.M. Wang, A.V. Hamza, E. Ma, Acta Mater., *Temperature-dependent strain rate sensitivity and activation volume of nanocrystalline Ni*, **54**, 2715 (2006)

67. J. Schiotz, K.W. Jacobsen, Science, *A maximum in the strength of nanocrystalline copper*, **301**, 2715 (2006)

68. Z.W. Shan, E.A. Stach, J.M.K. Wiezorek, J.A. Knapp, D.M. Follstaedt, S.X. Mao, Science, *Grain boundary-mediated plasticity in nanocrystalline nickel*, **305**, 654 (2004)

69. E. Ma, Science, *Watching the nanograins roll*, **305**, 623 (2004)

70. M. Dao, L. Lu, Y.S. Shen, S. Suresh Acta Mater., *Strength, strain rate sensitivity and ductility of copper with nano-scale twins*, **54(20)**, 5421 (2006)
71. L. Lu Y.F Shen, X.H Chen, L.H. Qian, K. Lu, Science, *Ultrahigh strength and high electrical conductivity in copper*, **304**, 422 (2004)
72. G.I Taylor, Proc. Roy. Soc., *The mechanisms of plastic deformation of crystals. Part I. Theoretical*, **145**, 362 (1934)
73. K.M Yossef, R.O Scattergood, K.L. Murty, C.C. Koch, Appl. Phys. Lett., *Ultratough nanocrystalline copper with a narrow grain size distribution*, **85**, 929 (2004)
74. E. Ma, Y.M. Wang, Q.H. Lu, M.L Sui, L. Lu, K. Lu, Appl. Phys. Lett., *Strain hardening and large tensile elongation in ultrahigh-strength nano-twinned copper*, **85**, 4932 (2004)
75. Y.M. Wang and E. Ma *Mechanical properties of bulk nanostructured materials: in Bulk Nanostructured Materals* Y. Zhu and M Zehetbauer (Eds) Wiley VCH, 2009, pp425-453
76. Y.M. Wang, E. Ma, Mater. Sci. Eng. A, *Strain hardening, strain rate sensitivity and ductility of nanostructured metals*, **375-377**, 46 (2004)
77. D. Jia, Y. M Wang, K.T. Ramesh, E. Ma, Y.T. Zhu, R.Z. Valiev, Appl. Phys. Lettr., *Deformation behaviour and plastic instabilities in ultra-fine grained titanium*, **76**, 611 (2001)
78. A. Hasnaoui, H. Van Swygenhoven, P.M. Derlet. Science, *Dimples on fracture surfaces as evidence for shear plane formation in nanocrystalline metals*, **300**, 1550 (2003)
79. C.C. Koch, D.G. Morris, K. Lu, A. Innoe, MRS Bull, *Ductility of nanostructured materials*, **24**, 54 (1999)
80. Y.M. Wang, M.W. Chen. F.H. Zhou, E. Ma, Nature, *High tensile ductility in a nanostructured metal*, **419**, 912, (2002)
81. K.M. Yossef, R.O Scatterot, K.L Murphy, J.A. Horton, C.C. Koch, Appl. Phys. Lett., *Ultrahigh Strength and High Ductility of Bulk Nanocrystalline Copper*, **87**, 091904 (2005)
82. R.Z. Valiev, I.V. Alexandrov, Y.T. Zhu, T.C. Lowe, J. Mater. Res., *Paradox of strength and ductility in metals processed by severe plastic deformation*, **17(1)**, 5 (2002)
83. E.W. Hart, Acta Metall., *Theory of tensile test*, **15**, 351 (1967)

84. G. He, J. Eckert, W. Loser, L. Shultz, Nature Mater., *Novel Ti-base nanostructure–dendrite composite with enhanced plasticity*, **2**, 33 (2003)

85. Z. Horita, K. Okashi, T. Fujita, K. Kaneko, T.G. Langdon, Adv. Mater., *Achieving high strength and high ductility in precipitation hardening alloys*, **17**, 1599 (2005)

86. R.Z. Valiev, A. Sergeeva, A.K. Mukherjee. Scr. Mater., *The effect of annealing on tensile deformation behavior of nanostructured SPD titanium*, **49**, 669 (2003)

87. I. Karakaya, W.T. Thompson . In: T.B. Massalski (Editor-in-chef), H. Okamoto, P.R. Subramanian, L. Kacprzak (Eds.), *Binary alloy phase diagrams*, vol. 1, William W. Scott, second edition, 1990, p 72

88. M. Levy (Editor-in-chef), H. Bass, R. Stern (Eds) *Handbook of Elastic Properties of Solids, Liquids, and Gases, Vol 2:Elastic properties of solids : theory, elements and compounds, novel materials, technological materials, alloys, and building materials*, Academic press, 2000

89. S. Crampin, D.D. Vedensky, R. Monnier, Phil. Mag. A., *Stacking fault energies of random metallic alloys*, **67**, 1447 (1993)

90. H.P. Klug, L.E. Alexander, *X-ray Diffraction Procedures for Polycrystalline and Amorphous Materials*, second ed., Wiley-Interscience, New York, 1974.

91. J. Markmann, V. Yamakov, J. Weissmuller, Scr. Mater., *Validating grain size analysis from X-ray line broadening: A virtual experiment*, **59**, 15 (2008)

92. P. Scherrer, Gött. Nachr., *Bestimmung der Grösse und der inneren Struktur von Kolloidteilchen mittels Röntgenstrahlen*, **26** (1918) 98–100.

93. C.E. Krill, R. Birringer, Phil. Mag. A, *Estimating grain-size distributions in nanocrystalline materials from x-ray diffraction profile analysis*, **77**, 321 (1998)

94. B.E. Warren, *X-ray diffraction*, Dover, New York,1990.

95. R. Birringer, M. Hoffmann, P. Zimmer. Phys. Rev. Lett., *Interface stress in polycrystalline materials: the case of nanocrystalline Pd*, **88**, 206104 (2002)

96. J. Markmann, *Mikrostrukturuntersuchungen an kaltwalzenem nanokristallinem Palladium*, FZKA7126, 2005

97. B.J. Kestel. Ultramicroscopy, *Improved retention of precipitates in stainless steels during jet thinning for TEM*, **19**, 213 (1986)

98. H. Elias, D.M. Hyde, R.L Scheaffer, *A guide to practical stereology* Basel u.a.: Karger, 1983, 305 S.

99. DIN EN 10002, ASTM E8/E8M-08.

100. J.M. Howe, U. Dahmen, R. Gronsky. Phil. Mag. A, *Atomic mechanisms of precipitate plate growth*, **56**, 31 (1987)

101. R. Pippan, F. Wetcher, M. Hafok, A. Vorhauer, I. Sabirov, Adv. Eng. Mater., *The limits of refinement by severe plastic deformation*, **8**, 1046 (2006)

102. A. Vorhauer, R. Pippan, Metall. Mater. Trans. A, *On the onset of a steady state in body-centered cubic iron during severe plastic deformation at low homologous temperatures*. 39, 417 (2008)

103. J.R. Weertman, D. Farkas, K. Hemker, H. Kung, M. Mayo, R. Mitra, and H. Van Swygenhoven. MRS Bulletin, *Structure and mechanical behavior of bulk nanocrystalline materials* **24**, 44 (1999).

104. F. Dalla Torre, H. Van Swygenhoven, and M. Victoria, Acta Mater., *Nanocrystalline electrodeposited Ni: microstructure and tensile properties*, **50**, 3957 (2002)

105. K.S. Kumar, H. Van Swygenhoven, S. Suresh, Acta Mater., *Mechanical behavior of nanocrystalline metals and alloys*, **51,** 5743 (2003).

106. R.Z. Valiev, Yu. Ivanisenko, E.E. Rauch, B. Baudelet. Acta Mater., *Structure and deformation behavior of Armco iron subjected to severe plastic deformation*, **12**, 4705 (1996)

107. H.-J. Fecht. In *Nanomaterials: Synthesis, Properties, and Application*, Edestein AS and CammarataRC (Eds.), J.W. Arrowsmith LTD, Bristol, 1996

108. F.A. Mohammed, Acta Mater., *A dislocation model for minimum grain size obtainable by milling*, **51**, 4107 (2003)

109. Y.H. Zhao, Y.T. Zhu, X.Z. Liao, Z. Horita, T.G. Langdon, Mater. Sci. Eng. A, *Influence of stacking fault energy on nanostructure formation under high pressure torsion*, **188**, 410 (2005)

110. Y.H. Zhao, Y.T. Zhu, X.Z. Liao, Z. Horita, T.G. Langdon, Mater. Sci. Eng. A, *Influence of stacking fault energy on the minimum grain size achieved in severe plastic deformation*, **463**, 22 (2007)

111. L. Balogh, T. Ungar, Y. Zhao, Y.T. Zhu, Z. Horita, C. Xu, T.G. Langdon, Acta Mater., *Influence of stacking-fault energy on microstructural characteristics of ultrafine-grain copper and copper–zinc alloys*, **56**, 809 (2008)

112. G.K. Willamson, R.E. Smallmann. Phil. Mag., *III. Dislocation densities in some annealed and cold-worked metals from measurements on the X-ray debye-scherrer spectrum*, **1**, 34 (1956)

113. R.E Smallman, K.H. Westmacott,. Phil. Mag., **S***tacking faults in face-centred cubic metals and alloys*, **2**, 669 (1957)

114. T. Ungár, A. Borbély, Appl. Phys. Let., *The effect of dislocation contrast on x-ray line broadening: A new approach to line profile analysi*s, **69**, 3173 (1996)

115. J.P. Hirth, J. Lothe, *Theory of dislocations*. New York: Wiley, 1982, p. 332-335

116. X.Z. Liao, F. Zhou, E.J. Lavernia, S.G. Srinivasan, M.I. Baskes, D.W. He, Y.T. Zhu, Appl. Phys. Lett., *Deformation mechanism in nanocrystalline Al: partial dislocation slip*, **83**, 632 (2003)

117. I.L. Dillamore, S.M. Smallman, Phil. Mag., *The stacking-fault energy of F.C.C. metals*, **12**, 191 (1965)

118. V Yamakov, D Wolf, SR Phillpot, Gleiter H. Acta Mater., *Deformation Twinning in Nanocrystalline Al by Molecular-Dynamics Simulation*, **50**, 61 (2002)

119. N. Bernstein, E.B. Tadmor, Phys. Rev. B, *Tight-binding calculation of stacking fault energy and twinnability in fcc metals*, **69**, 094116 (2004)

120. S. Kibey, J.B. Liu, D.D. Johnson, H. Sehitoglu. Acta Mater., *Predict twinning stress in fcc metals: Linking twin-energy pathways to twin nucleation*, **55**, 6843 (2007)

121. Yu. Ivanisenko, W. Skrotzki, R. Chulist, T. Lippmann, K. Yang, L. Kurmanaeva, H.-J. Fecht, J. Mater. Sci., *Recent results on deformation mechanisms in nanocrystalline Pd-10% Au inferred from texture analysis*, **45(17)**, 4571 (2010).

122. Yu. Ivanisenko, L. Kurmanaeva, J. Weissmueller, K. Yang, J. Markmann, H. Rösner, T. Scherrer, H.-J. Fecht *Deformation mechanisms of nanocrystalline palladium at large strain.* Acta Mater. **57**, 3391 (2009) 3391.

123. P. Rodriguez, Rao. K. Krishna. J. Inst. Met., *Yield-strength in polycrystalline silver-palladium alloys*, **93** (1964-65).

124. ASM Handbook: *Mechanical Testing and Evaluation*: Vol 8 Kuhn H, Medlin D (Eds.): ASM International, 2000.

125. D. Calliard, J.L. Martin *Thermally activated mechanisms in crystal plasticity*. Amsterdam: Pergamon (2003) p.13.

126. G.E. Dieter *Mechanical Metallurgy*, 3rd ed. Boston (MA) McGraw-Hill (1986) p. 173.

Curriculum Vitae

Personal details

Name	: Lilia Kurmanaeva
Date of birth	: 25 July 1983
Nationality	: Russian
Marital status	: Single

Education

Sept 1991 - Jun 2000	School Nr. 19, Salavat, Russia: with Honours
Sept 2000 - Jun 2005	Engineer in Material Science Ufa State Aviation Technical University

Experience

Sept 2005 - Sept 2006	Research Assistant in Institute of Physics of Advanced Materials, Ufa State Aviation Technical University, Ufa, Russia
Since 2006	Scientific co-worker in Institute for Nanotechnology, Karlsruhe Institute of Technology, Karlsruhe

Awards

2008	Early Carrier Researcher Award at NanoSPD4, Goslar, Germany
2009	Best oral report in the special session for young scientists at BNM-2009, Ufa, Russia

Scientific Output

9 scientific publications

9 conference contributions

Publications

1. L. Kurmanaeva, Yu. Ivanisenko, J. Markmann, R.Z. Valiev, H.-J. Fecht: *Grain refinement and deformation behavior of ultrafine grained Pd and Pd-Ag alloys produced by HPT.* Materials Science Forum **584-586** (2008) 182-187.
2. Yu. Ivanisenko, L. Kurmanaeva, J. Weissmueller, K. Yang, J. Markmann, H. Rösner, T. Scherrer, H.-J. Fecht *Deformation mechanisms of nanocrystalline palladium at large strain.* Acta Mater. **57**, 3391 (2010) 3391.
3. I. Choi, R. Schwaiger, L. Kurmanaeva, O. Kraft. *On the effect of Ag content on the deformation behavior of ultra-fine grained Pd-Ag alloys* Scr. Mater. **61**, 64 (2009)
4. H. Jin, L. Kurmanaeva, J. Schmauch, H. Rösner; Yu. Ivanisenko, J. Weissmüller: *Deforming Nanoporous Metal: Role of Lattice Coherency.* Acta Mater. **57,** 2665 (2009)
5. K. Yang, Yu. Ivanisenko, A. Caron, A, Chubillin, L. Kurmanaeva, T. Scherer, R.Z. Valiev, H.-J. Fecht *Mechanical behaviour and in situ observation of shear bands in ultra-fine grained Pd and Pd-Ag alloys* Acta Mater, **58**, 967 (2010)
6. Yu. Ivanisenko, W. Skrotzki, R. Chulist, T. Lippmann, L. Kurmanaeva, H.-J. Fecht: *Information on deformation mechanisms in nanocrystalline Pd-10% Au inferred from texture analysis*. J. Mat. Sci. **45,** 4571 (2010)
7. Yu. Ivanisenko, L. Kurmanaeva, K Yang, H.-J. Fecht: *Can we use kinetic analysis for investigation of deformation processes in nanocrystalline materials?* Proceedings of ICSMA-15 in Dresden, Germany, August 2009, Journal of Physics: Conference Series (2010)
8. L. Kurmanaeva., Yu Ivanisenko, J. Markmann, C. Kübel, A. Chuvillin, R.Z. Valiev, H-J Fecht *Grain refinement and mechanical properties in ultrafine grained Pd and Pd - Ag alloys produced by HPT* Mater Sci Eng A, **527**, 1776 (2010)
9. L. Kurmanaeva., Yu Ivanisenko, J. Markmann, K. Yang, H-J Fecht and J. Weissmüller. *Work hardening and inherent plastic instability of nanocrystalline metals.* Phys Stats Solidi RRL, **4 (5-6)**, 130 (2010)

Conference contributions

1. *Microstructure and deformation behaviour of nc Pd*. "10th European Congress and Exhibition on Advanced Materials and Processes (Euromat 2007)", 10-13 September 2007, Nürnberg, Germany,

2. *New approach of designing increased strain hardening in nanostructured materials* "German Physical Society Meeting (DPG)", 25-29 February 2008, Berlin, Germany,

3. *Deformation behavior of nanocrystalline metals and alloys investigated by mini-tensile test.* "137th Annual Meeting and Exhibition of the Minerals, Metals and Materials Society (TMS 2008)", 9-13 March 2008, New Orleans, LA, USA

4. *Grain refinement and deformation behavior of ultrafine grained Pd and Pd-Ag alloys produced by HPT* "The 4th International Conference on Nanomaterials by Severe Plastic Deformation (NanoSPD4)", 17-22 August 2008, Goslar, Germany *[2nd second price in Young scientist session]*

5. *Deformation behavior of nanocrystalline metals and alloys investigated by mini-compression test* "International Workshop on the Plasticity of Nanocrystalline Metals", 28 September-01 October 2008, Bostalsee, Germany

6. *Deformation behavior and microstructure of nanocrystalline Pd and Pd-10 at. % Au alloy investigated by mini-compression test* "International Symposium Bulk Nanostructured materials (BNM 2009)", 21-26 September 2009, Ufa, Russia, [2nd price]

7. *Deformation behavior of nanocrystalline Pd and Pd-10 at. % Au alloy investigated by mini-compression test* "German Physical Society Meeting (DPG)", 22-27 March 2009, Dresden, Germany

8. *Deformation behavior of nanocrystalline Pd-10 at. % Au alloy investigated in compression mode at different temperatures* "Annual Meeting and Exhibition of the Minerals, Metals and Materials Society (TMS 2010)", 14-18 February 2010, Seattle, WA, USA

9. *The optimal grain size for strength and ductility in nanocrystalline Pd* "The 5th International Conference on Nanomaterials by Severe Plastic Deformation (NanoSPD5)", 21-25 Marcht 2011, Nanjing, China

Acknowledgements

It is a pleasure to thank the many people who made this thesis possible.

I would like to thank Prof. Hans-Jörg Fecht who considered me to be capable of doing this PhD work. I am grateful for his interest in the project and the constructive discussions.

It is difficult to overstate my gratitude to Dr. Yulia Ivanisenko. I appreciate her vast knowledge and skill in many areas, and her assistance in writing reports. Throughout my research, she provided encouragement, good teaching, sound advices, good company, and many interesting ideas. I would have been lost without her.

I would like to express my sincere thanks to Prof. Ruslan Valiev from Ufa State Aviation Technical University, Russia for the fruitful collaboration. At his institute I obtained elementary knowledge about bulk nanostructured materials, and during my work at INT I still could feel his support. Furthermore, I am very thankful to him for the HPT processing of my samples.

I wish to thank Prof. Jörg Weissmüller for his scientific suggestions, friendly support, and the valuable discussions.

I gratefully acknowledge Dr. Jürgen Markmann's patience in explaining to me the basics of XRD analysis, and I appreciate his constructive comments and suggestions, and of course, the fruitful discussions.

I would like to express my sincere gratitude to Torsten Scherer who introduced me in a lot of aspects of sample preparation. My appreciation also goes to Dr. Christian Kübel, Dr. Harald Rösner for helping with the HRTEM of my samples.

I would also like to thank Kejing Yang from Ulm University, Institute of Micro and Nanomaterials, for shearing with me results of her experiments which helped to thoroughly understand my experiments.

I am grateful to IMF II for the access to the Schenk compression–torsion machine and transmission electrone microscope CM 30. I sincerely appreciated Mr Stephen Knaak's (IMF II) help in conducting the HPT experiments, and both Mr. Michael Schlenker's and Tanja Fabry's (workshop department) well-timed cutting of my samples.

I would like to acknowledge the affection and the support from my friends and colleagues Sveta, Maxim, Agnieszka, and Sylwia. Their company has made my time at INT a memorable experience.

Special thanks to Christine Batch, Patricia Jaeger and Erika Schütze for taking care of official matters during my stay at the Institute of Nanotechnology. And many thanks to everyone who has contributed in any way to this Ph.D. thesis.

Financial support from the Deutsche Forschungsgemeinschaft under contract FOR714 is gratefully acknowledged.

Finally, I want to thank my parents for the patience, support, and understanding.